

Mar Cóndor Salgado

Cell traction forces in 3-D microenvironments

Departamento
Instituto de Investigación en Ingeniería [I3A]

Director/es
García Aznar, José Manuel
Fabry, Ben

<http://zaguan.unizar.es/collection/Tesis>



Reconocimiento – NoComercial – SinObraDerivada (by-nc-nd): No se permite un uso comercial de la obra original ni la generación de obras derivadas.

© Universidad de Zaragoza
Servicio de Publicaciones

ISSN 2254-7606



Universidad
Zaragoza

Tesis Doctoral

CELL TRACTION FORCES IN 3-D MICROENVIRONMENTS

Autor

Mar Cóndor Salgado

Director/es

García Aznar, José Manuel
Fabry, Ben

UNIVERSIDAD DE ZARAGOZA

Instituto de Investigación en Ingeniería [I3A]

2018



**Universidad
Zaragoza**



Escuela de
Ingeniería y Arquitectura
Universidad Zaragoza



FRIEDRICH-ALEXANDER
UNIVERSITÄT
ERLANGEN-NÜRNBERG

Cell traction forces in 3-D microenvironments

DISSERTATION

submitted in partial fulfillment of the requirements for the degree of

DOCTOR OF PHILOSOPHY

in Biomedical Engineering

by

Mar Cóndor Salgado

Faculty advisors

José Manuel García Aznar

Ben Fabry

Aragon Institute of Engineering Research (I3A)

Department of Mechanical Engineering, University of Zaragoza, Spain

&

Department of Physics, University of Erlangen-Nuremberg, Germany

Zaragoza, May 2018

A mis padres

What leads and drags the world are not machines, but ideas.

~Victor Hugo

ABSTRACT

Cells are able to actively sense and respond to mechanical stimuli in their surroundings. The mechanical stimuli emerging from the extracellular matrix, such as stiffness, surface topology and deformation, are transduced into biochemical signals through interactions between the cell and the matrix. In order to survive and grow cells must attach to and spread on a substrate. Once attached, cells generate internal contractile forces through actomyosin interactions and exert tractions on the underlying substrate. Thus, cell traction forces are critical regulators of cell adhesion, signaling and function and therefore are crucial in many biological processes such as inflammation, wound healing, angiogenesis and metastasis. Despite their importance, measuring cellular forces in a physiological context and understanding their contribution to biological processes remain challenging. Moreover, since cell-matrix interactions vary considerably between two-dimensional and three-dimensional environments, understanding their influence over normal and pathological cell responses in three-dimensional systems that better mimic the *in vivo* microenvironment is essential to translate such insights efficiently into medical therapies.

Thus, the main scope of this Thesis is the development of computational models focused on studying different aspects of cell-matrix interactions so that specific phenomena can be better understood, serving as a guide for the development of new experiments and *in vitro* modeling techniques. All the models and experiments contained in this thesis are focused on studying single cells. Firstly, due to the complexity and marked differences with respect to collective cell migration, and secondly owing to the importance of individual cell migration in such important processes as tumor cell invasion. In addition, since three-dimensional environments are physiologically more relevant, in most of the *in silico* models developed in this Thesis, three-dimensional approaches have been considered to better mimic cell and tissue *in vivo* conditions.

Firstly, the binding dynamics of cell-matrix adhesion sites and how cells transmit forces to the extracellular matrix is investigated. For this purpose, a numerical model is developed within the framework of the finite element method. Secondly, an *in vitro* model is introduced to study three-dimensional cell-matrix interactions at both cell and

tissue level. In particular, different microfluidic-based devices are presented, which are currently being used for studying different biological processes. Those have been used to study the chemical gradient formation process inside a three-dimensional matrix.

Recent research demonstrated that cell traction forces are critical regulators of tumor cell invasion, which is highly dependent on the mechanical properties of both the cell and the surrounding matrix. Because a deeper understanding of this mechanism is needed, the second part of this Thesis focused on different experiments to quantify cellular forces as well as an *in silico* finite element model to reconstruct the forces exerted by cells during its migration, thereby allowing to study the dependency of the mechanical properties of cells onto the force solution obtained.

In sum, new insights into the mechanisms underlying cell-matrix interactions, brought in part by the emergence of new technologies to study cellular mechanics at high spatial and temporal resolution, will not only result in a better understanding of cellular behavior in normal cells but may also lead to the development of novel therapies in diseases linked to defects in cellular mechanical interactions.

Keywords: Computational modeling, finite element simulation, cell traction forces, cell migration, focal adhesions, microfluidic-based devices, chemical gradients, traction force microscopy, *in vitro* cell culture, collagen hydrogels, fibrin hydrogels, steric hindrance.

SINOPSIS

Las células son capaces de sentir y responder activamente frente a los estímulos mecánicos de su entorno. Los estímulos mecánicos que provienen de la matriz extracelular, tales como la rigidez, la topología de la superficie o la deformación, son traducidos en señales bioquímicas a través de las interacciones entre la célula y la matriz. Para poder sobrevivir y crecer las células necesitan adherirse y propagarse sobre el sustrato que las rodea. Una vez adheridas, las células generan fuerzas contráctiles a través de la interacción actina-miosina, ejerciendo de este modo tracción sobre el sustrato subyacente. Es por ello, que las fuerzas de tracción ejercidas por las células son reguladores críticos de la adhesión, la señalización y la función celular, y por tanto son muy importantes en numerosos procesos biológicos tales como la inflamación, la cicatrización de heridas, la angiogénesis e incluso la metástasis. Pese a su importancia, la medición de las fuerzas celulares en un contexto fisiológico así como entender su contribución en los procesos biológicos sigue siendo todavía un reto. Además, debido a que las interacciones célula-matriz varían considerablemente entre ambientes bidimensionales y tridimensionales, entender su influencia sobre las respuestas celulares normales y patológicas en sistemas tridimensionales es esencial para poder traducir de manera eficiente dichos conocimientos en terapias médicas.

El principal objetivo de esta Tesis es, por tanto, el desarrollo de modelos computacionales enfocados al estudio de diferentes aspectos de las interacciones célula-matriz, que permitan entender mejor los fenómenos específicos y que sirvan como referencia para el desarrollo de nuevos experimentos y de técnicas de modelado *in vitro*. Además, todos los modelos y experimentos contenidos en esta tesis se centran en el estudio de células individuales. En primer lugar, debido a la complejidad y a las grandes diferencias que presentan con respecto a la migración celular colectiva, y en segundo lugar debido a la importancia que supone el estudio de la migración celular individual en procesos tan importantes como es la invasión de células tumorales. Además, debido a la relevancia que suponen fisiológicamente los entornos tridimensionales, en la mayoría de los modelos *in silico* desarrollados en esta Tesis, se han considerado aproximaciones tridimensionales para poder así imitar mejor las condiciones *in vivo* de células y tejidos.

En primer lugar, se ha investigado la dinámica de unión de los sitios de adhesión célula-matriz, más en particular cómo las células transmiten las fuerzas a través de estas uniones a la matriz extracelular. Para ello, se ha desarrollado un modelo numérico mediante el uso del método de los elementos finitos. En segundo lugar, se ha desarrollado un modelo *in vitro* para el estudio de las interacciones célula-matriz tanto a nivel celular como a nivel de tejido. En particular, se presentan diferentes dispositivos de microfluídica, los cuales están siendo utilizados en la actualidad para el estudio de diferentes procesos biológicos. Estos han sido utilizados para estudiar los procesos de formación de gradientes químicos a través de una matriz tridimensional.

Investigaciones recientes han indicado que las fuerzas de tracción celular son reguladores críticos de la invasión de las células tumorales, las cuales dependen en gran medida de las propiedades mecánicas tanto de las células como de la matriz que las rodea. Debido a que surge la necesidad de tener un conocimiento mucho más profundo sobre este mecanismo, la segunda parte de esta Tesis se ha centrado en el desarrollo de diferentes experimentos para cuantificar las fuerzas celulares, así como en el desarrollo de un modelo *in silico* basado en elementos finitos para reconstruir las fuerzas ejercidas por las células durante su migración, permitiendo de este modo estudiar la dependencia de las propiedades mecánicas de las células sobre la solución de fuerzas obtenida.

En resumen, una mejor comprensión de los mecanismos subyacentes a las interacciones célula-matriz, aportados en parte por la aparición de nuevas tecnologías para estudiar la mecánica celular a alta resolución espacial y temporal, no sólo resulta en una mejor comprensión del comportamiento de células normales, sino que también conduce al desarrollo de terapias novedosas para enfermedades relacionadas con los defectos en las interacciones mecánicas celulares.

Palabras clave: Modelado computacional, simulación de elementos finitos, fuerzas de tracción celular, migración celular, adhesiones focales, dispositivos de microfluídica, gradientes químicos, microscopía de fuerza de tracción, cultivo celular *in vitro*, hidrogeles de colágeno, hidrogeles de fibrina, impedimento estérico.

AGRADECIMIENTOS

Quisiera comenzar expresando mi más profundo agradecimiento a mis directores de Tesis Manu y Ben, no sólo por vuestro apoyo en el ámbito científico sino también por vuestra cercanía y amistad. Sin vuestra supervisión este trabajo no habría sido posible.

También quiero brindar un especial agradecimiento a Mariajo, quien me acogió por primera vez y me guió durante los primeros pasos en el mundo de la investigación y la docencia.

Especial mención a los locatis (L.E.S.) Andrea, Jorge e Ismael... sin vosotros no hubiera sido posible avanzar en los momentos más difíciles de esta larga aventura. Juntos hemos disfrutado de grandes momentos dentro y fuera de la sala. Espero poder seguir compartiendo muchos más a vuestro lado. Agradecer también a todo el departamento, por vuestra ayuda desinteresada y en especial a todos los compañeros de la sala, grupo y del laboratorio, Mariangeles, Cris, Carlos, Tirso, Reich, Sara, Nieves, Sergio, Marina, Pablo y Enrique.

No puedo olvidar tampoco a mis amigas y amigos, en especial a Fani, gracias por transmitirme tu energía y animarme a no dejar nunca de perseguir mis sueños. Tampoco puedo dejarme a Dani, Diego, Pablo y Borja, mis compañeros de bici, de cordada y de aventuras de montaña. Vosotros también formáis parte de este proyecto tan especial. Muchas gracias por todo vuestro apoyo y cariño durante estos años.

Quiero también dedicar un especial agradecimiento a Pablo. Por acompañarme y apoyarme durante los años de la tesis, sin ti tampoco hubiera sido posible este gran reto. También a ti pequeño-gran Javi. Sé que aunque estés lejos, estás cada día más cerca.

Por último quiero agradecer a mis padres, porque todo lo que soy os lo debo a vosotros. Por mostrarme vuestro apoyo incondicional tanto en los buenos como en los malos momentos y por no dejar nunca de creer en mí. En especial en estos últimos tiempos, en los que habéis sabido animarme y hacerme sonreír. Por ello, quiero dedicaros esta tesis a vosotros.

ACKNOWLEDGEMENTS

I would like to deeply thank you Ben, not only for your wisdom and guidance during my PhD, but also for your kindness and friendship. This thesis wouldn't have been possible without you.

Also thanks to entire Fabry's lab: Richi, Foxi, Chris, Astrid, Marina, Janina.... we shared short but very fun moments, always accompanied with cool technical discussions and very good german beer. I hope we keep in touch and wish you all the best.

CONTENTS

ABSTRACT	I
SINOPSIS	III
AGRADECIMIENTOS	V
ACKNOWLEDGEMENTS	VI
CONTENTS	VII
LIST OF FIGURES.....	XIII
LIST OF TABLES	XVI
ABBREVIATIONS	XVII
1. INTRODUCTION	1
1.1. Background.....	2
1.1.1. Cell invasion	3
1.1.2. Cell traction forces	4
1.1.3. Biomimetic 3-D hydrogels.....	6
1.1.4. Microfluidics: A novel technology for studying cell-matrix interactions in 3-D microenvironments.....	8
1.2. State of the art	10
1.2.1. Measuring methods of forces generated by an entire tissue	11
1.2.2. Measuring methods of forces generated by a single cell.....	12
1.2.2.1. Traction forces in two dimensions	13
1.2.2.2. Traction forces in three dimensions.....	14
1.3. Motivation.....	15
1.4. Objectives.....	16
1.5. Outline.....	18

2. MACROSCOPIC SIMULATION OF CELL-MATRIX ADHESION	21
2.1. Introduction.....	22
2.2. Cell-matrix adhesion model	25
2.2.1. Constitutive law for mechanical adhesion.....	26
2.2.2. Mechanical stimuli that regulate adhesion	28
2.2.3. Binding/unbinding criteria	29
2.2.4. Temporal evolution of the DOA.....	31
2.2.5. Mechanical failure of the adhesion	32
2.2.6. Reinforcement criterion.....	33
2.2.7. Numerical implementation	34
2.3. Theoretical model validation: Local modeling of the dynamics of cell-matrix adhesion.....	36
2.3.1. Description of the finite element model and model parameters	36
2.3.2. Numerical results and sensitivity analysis	38
2.3.2.1. Influence of substrate stiffness on cell-matrix adhesion	39
2.3.2.2. Influence of substrate stiffness on adhesion rupture	42
2.3.2.3. Influence of cell force rate on adhesion rupture	43
2.3.2.4. Influence of traction forces on the cell-matrix adhesion	44
2.4. Numerical predictions: Global modeling of cell-matrix adhesions.....	46
2.4.1. Description of the FE model	46
2.4.2. Influence of cell deformation on cell-matrix adhesion	48
2.4.3. Influence of substrate deformation on cell-matrix adhesion.....	51
2.5. Discussion	52
3. IN VITRO MODEL FOR STUDYING CELL-MATRIX INTERACTIONS	55
3.1. Introduction.....	56
3.2. Microfluidic devices design and fabrication	58

3.3.	Study of GF transport within synthetic hydrogels inside microfluidic devices	59
3.3.1.	Numerical model of GF transport within synthetic hydrogels	60
3.3.2.	Microfluidic device geometry parameterization	61
3.3.3.	3-D Finite element model of a microfluidic device	65
3.3.4.	Web application for the numerical model proposed: Insilico-cell	66
3.4.	Results	68
3.4.1.	Numerical predictions of GF transport: 4 different geometries	68
3.4.2.	Multiparametric analysis of gradient formation within a synthetic collagen-based hydrogel	70
3.4.3.	Numerical predictions of GF transport under different hydrogel combinations	72
3.4.4.	Automatic quantification of GF signaling: a web application	75
3.5.	Discussion	76
4.	RECURSIVE METHOD FOR RECONSTRUCTING CELL TRACTION FORCES	81
4.1.	Introduction	82
4.2.	Material and methods	84
4.2.1.	Cell culture and preparation of 3D collagen gels	84
4.2.2.	Live cell imaging inside a microfluidic device	85
4.2.3.	3-D cell-specific segmentation and FE mesh development	87
4.2.4.	3-D finite element model and examples of application	88
4.3.	Numerical reconstruction of cell traction forces	90
4.3.1.	Introduction	90
4.3.2.	Direct problem for determining the reaction forces	92
4.3.3.	Direct problem for applying reaction forces and determining traction forces	93
4.3.4.	Recursive formulation for solving the inverse form problem	94

4.4.	Results	95
4.4.1.	Direct problem: Determination of the input displacement field	95
4.4.2.	Inverse FE problem: Numerical model validation	96
4.4.3.	Effect of cell properties onto the traction force solution.....	98
4.5.	Discussion	100
5.	EFFECT OF CELL MECHANICAL PROPERTIES ON TRACTION FORCES	103
5.1.	Introduction.....	104
5.2.	Material and Methods	105
5.2.1.	Cell culture	105
5.2.2.	MBA-MD 231 Lam-A lentiviral transduction.....	106
5.2.3.	Internalization of latex beads	107
5.2.4.	Bead internalization analysis with tdTomato-farnesyl live cell membrane staining	107
5.2.5.	Preparation of 3-D collagen hydrogels	108
5.2.6.	Collagen gel mechanical characterization	108
5.2.7.	Invasion assay in a 3-D collagen gel.....	110
5.2.8.	3-D Traction force microscopy assay	111
5.2.9.	Unconstrained traction force reconstruction.....	112
5.2.10.	Cell shape analysis	113
5.2.11.	Statistical analysis	113
5.3.	Results	113
5.3.1.	Effect of cell stiffness on cell invasion	113
5.3.2.	Adaptation of contractile forces to altered steric hindrance	116
5.3.3.	Strain energy and matrix stiffening	123
5.3.4.	Effect of steric hindrance on cell morphology.....	126
5.4.	Discussion	128

6. CONCLUSIONS	131
6.1. Conclusions.....	132
6.2. Original contributions	135
6.2.1. Publications in peer-reviewed journals	135
6.2.2. Congress and conference contributions.....	136
6.3. Future lines of work	138
APPENDIX A: RESUMEN Y CONCLUSIONES	139
A.1 Antecedentes	140
A.1.1. Invasión celular	141
A.1.2. Fuerzas de tracción celulares.....	142
A.1.3. Hidrogeles biomiméticos tridimensionales	144
A.1.4. Microfluídica: Tecnología de vanguardia para el estudio de la interacción célula-matriz en ambientes 3-D.....	147
A.1.5. Estado del arte de la microscopía de fuerza de tracción.....	149
A.2 Conclusiones.....	150
A.3 Contribuciones originales.....	154
A.3.1. Publicaciones relacionadas con la Tesis.....	154
A.3.2. Contribuciones a congresos	155
A.3.3. Otras contribuciones.....	156
A.4 Líneas futuras	157
BIBLIOGRAPHY.....	159

LIST OF FIGURES

MAIN CHAPTERS

Figure 1.1: Scheme of cell migration in a 2-D and 3-D matrix.....	3
Figure 1.2: Schematic of focal adhesion assembly on a 2-D migrating cell.	5
Figure 1.3: Different types of <i>in vitro</i> ECMs used for studying cell behavior.....	7
Figure 1.4: Different types of Microfluidic devices developed to investigate the biological responses of cells and tissues to various mechanical stimuli.....	9
Figure 1.5: Methods for measuring cell traction forces.	11
Figure 1.6: Thesis outline.....	20
Figure 2.1: Schematic of discrete FAs connecting a cell to an ECM-coated substrate.	22
Figure 2.2: Schematic of the evolution of cell-matrix adhesions.	24
Figure 2.3: Interface constitutive model.	27
Figure 2.4: Schematic of evolution of the adhesion degree on time.	31
Figure 2.5: Schematic of cell-matrix detachment process.	33
Figure 2.6: Iterative incremental-load algorithm.	35
Figure 2.7: Schematic of the FEM used for simulating the local cell-matrix adhesion.	36
Figure 2.8: Influence of substrate stiffness on cell-matrix adhesion.	40
Figure 2.9: Influence of integrin type on cell-matrix adhesion.	41
Figure 2.10: Influence of substrate stiffness on the lifetime of FAs.....	42
Figure 2.11: Influence of cell force rate on adhesion rupture.	44
Figure 2.12: Influence of traction forces on cell-matrix adhesion.	45
Figure 2.13: Schematic of the FEM used for simulating the global cell-matrix adhesion.	47
Figure 2.14: Influence of cell deformation on cell-matrix adhesion.	49
Figure 2.15: Influence of cell deformation rate on cell-matrix adhesion.....	50
Figure 2.16: Interface stresses as a result of cell deformation.	51
Figure 2.17: Influence of substrate deformation on cell-matrix adhesion.	52
Figure 3.1: Fabrication of microfluidic-based devices.....	59
Figure 3.2: Geometry of the microfluidic-based device.....	61
Figure 3.3: Parameterization of a microfluidic-based device.....	63
Figure 3.4: Finite element model of a microfluidic-based device.	65

Figure 3.5: Screenshot of the web-based application interface.	67
Figure 3.6: Numerical predictions of PDGF-BB diffusion within a collagen type I hydrogel for different microfluidic device geometries.	69
Figure 3.7: Results of the parametric analysis on chip-1 device.	71
Figure 3.8: Effect of hydrogel combination on the diffusion profiles.	73
Figure 3.9: Web application screenshot.	76
Figure 4.1: Preparation of collagen gels for injection into a microfluidic device.	85
Figure 4.2: Confocal microscopy imaging of an individual NHDF-GFP live cell spreading into a 3-D collagen gel.	86
Figure 4.3: Generation of a three-dimensional finite element mesh of a NHDF-GFP cell embedded on a 2 mg/ml collagen type-I hydrogel.	88
Figure 4.4: Deformed configuration of the problem.	90
Figure 4.5: Schema of the recursive algorithm.	92
Figure 4.6: Simulated displacement field around an individual NHDF cell. The magnitude of the displacements vectors are in microns.	96
Figure 4.7: Traction maps predicted around an individual NHDF cell.	97
Figure 4.8: Effect of cell mechanical properties on traction maps reconstruction through the inverse algorithm.	99
Figure 5.1: Representative cells invading a 1.2 mg/ml collagen gel.	106
Figure 5.2: Live cell membrane staining with td-Tomato-farnesyl.	108
Figure 5.3: 1.2 mg/ml collagen gel characterization.	109
Figure 5.4: Cell invasion assays.	111
Figure 5.5: Cell traction force reconstruction.	112
Figure 5.6: Results of invasion assays.	115
Figure 5.7: Cell traction forces around MDA-MB 231 cells.	116
Figure 5.8: 3-D density plots around the MDA-MB 231 breast carcinoma cells included in this study.	117
Figure 5.9: 3-D density plots around the MDA-MB 231 breast carcinoma cells included in this study.	118
Figure 5.10: 3-D density plots around the MDA-MB 231 breast carcinoma cells with lam-A overexpressed included in this study.	119

Figure 5.11: 3-D density plots around the MDA-MB 231 breast carcinoma cells with lam-A overexpressed included in this study.	120
Figure 5.12: 3-D density plots around the MDA-MB 231 breast carcinoma cells with 5- μ m polystyrene beads included in this study.	121
Figure 5.13: 3-D density plots around the MDA-MB 231 breast carcinoma cells with 5- μ m polystyrene beads included in this study.	122
Figure 5.14: Influence of cell rigidity on cell traction forces.	123
Figure 5.15: Influence of cell contractile forces on the collagen matrix properties.	125
Figure 5.16: Collagen matrix structure imaging.	126
Figure 5.17: Influence of steric hindrance on the morphology of cells.	127
Figure 5.18: Correlation analysis between cell contractility and cell aspect ratio.....	128

APPENDIX A

Figure A.1: Esquema de la migración celular en una matriz 2-D y 3-D.	141
Figure A.2: Esquema de la adhesión celular a una matriz bidimensional.....	144
Figure A.3: Tipos de MEC para estudiar el comportamiento celular <i>in vitro</i>	146
Figure A.4: Diferentes tipos de dispositivos de microfluídica desarrollados para investigar la respuestas biológica de células y tejidos ante diversos estímulos mecánicos.....	148
Figure A.5: Métodos para la medición de las fuerzas celulares.....	150

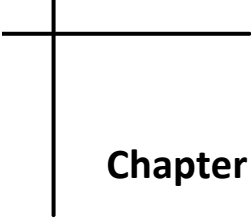
LIST OF TABLES

Table 2.1: Major parameters that define the interface adhesion model.	38
Table 2.2: Major parameters used in the 3-D model simulations.....	47
Table 3.1: Main geometrical parameters of microfluidic-devices.	64
Table 3.2: Major parameters used in the simulations.	74

ABBREVIATIONS

ECM	ExtraCellular Matrix
2-D	Two-Dimensional
3-D	Three-Dimensional
SFs	Stress Fibers
ATP	Adenosine TriPhosphate
CTFs	Cell Traction Forces
FAs	Focal Adhesions
FCs	Focal Complexes
FAK	Focal Adhesion Kinase
COL-I	Type I Collagen
PDMS	PolyDiMethylSiloxane
TFM	Traction Force Microscopy
PAA	PolyAcrylAmide
BAA	BisAcrylAmide
FTTC	Fourier Transform Traction Cytometry
FEM	Finite Element Method
DOA	Degree Of Adhesion
UMAT	User Defined Material
GF	Growth Factor
ELISA	Enzyme-Linked Immuno Sorbent Assays
PDGF-BB	Platelet Derived Growth Factor-BB
TGF- β_1	Transforming Growth Factor- β_1
LSCM	Laser Scanning Confocal Microscopy
NHDF	Normal Human Dermal Fibroblast

Cell traction forces in 3-D microenvironments



Chapter 1

INTRODUCTION

A brief summary of the current knowledge on the role of cell traction forces during cell invasion in two-dimensional and three-dimensional substrates is presented in this Chapter, specifically different experimental techniques and computational methods for traction force microscopy. Next, the motivation and main objectives of this Thesis, as well as a description of its structure are presented.

1.1. Background

In order to survive and grow cells must attach to and spread on a substrate [1-3]. Once attached, cells generate internal tensile forces through actomyosin interactions that are transmitted to the underlying substrate or the extracellular matrix (ECM) and lead to cell tractions. These cell traction forces are essential for cell migration, cell shape maintenance, mechanical signal generation and other cellular functions [4].

In the last few years, studies of cell migration in three-dimensional (3D) cell culture systems and *in vivo* have revealed several differences when compared with cell migration in two dimensions [5]. When cells grown on flat two-dimensional (2-D) substrates, the mechanical properties, in particular the stiffness of the underlying substrate, influence cell migration [6, 7]. Different studies have shown that when cells migrate on a more rigid substrate, the cells form more stable focal adhesions, which lead to a reduced migration speed and contributes to durotaxis, which induces cells to migrate in the direction of increasing substrate stiffness [1, 8]. In contrast to a 2-D substrate, when cells migrate through a three-dimensional (3-D) matrix, they must overcome not only the adhesion forces, but also the resisting forces imposed by the surrounding matrix [9-11]. Resisting forces mainly arise from steric effects as the cell moves through the matrix and deforms it. Then, to overcome the steric hindrance, cells need to generate traction forces that depend on the matrix properties (pore size and fiber stiffness [9, 12-14]) as well as cell properties (cell shape and stiffness [13, 15-19]).

Accordingly, studying these forces as well as the cell ability to deform the ECM is therefore important for a mechanistic understanding of many physiological and pathological cell functions in health and disease that involve cell adhesion, shape changes and migration, such as tissue formation during embryogenesis, tumor cell invasion in tissue, or the homing of immune cells [8, 20-23]. Furthermore, quantifying these forces is important for understanding the function of muscle cells and other highly contractile cells, such as fibroblasts, at both the tissue and organ levels.

1.1.1. Cell invasion

Most cells that are able to adhere, spread, and migrate onto a two-dimensional (2-D) substrate can also adhere, change shape, and migrate when embedded in a biopolymer network of suitable adhesiveness, stiffness, and network porosity (see Figure 1.1).

The ability of cells to invade a connective tissue depends on the following parameters that determine the speed of migration in dense 3-D matrices: cell adhesion and detachment, cytoskeletal remodeling, cell and matrix mechanical properties, the matrix remodeling by proteolytic enzyme secretion and protusive force generation [9, 24]. The balance of all these parameters determines cell invasiveness into 3-D matrices and a change of this balance leads to a switch toward another invasion mode such as mesenchymal or ameboid and with or without traction forces, therefore determining which invasion strategy was used by cells [25].

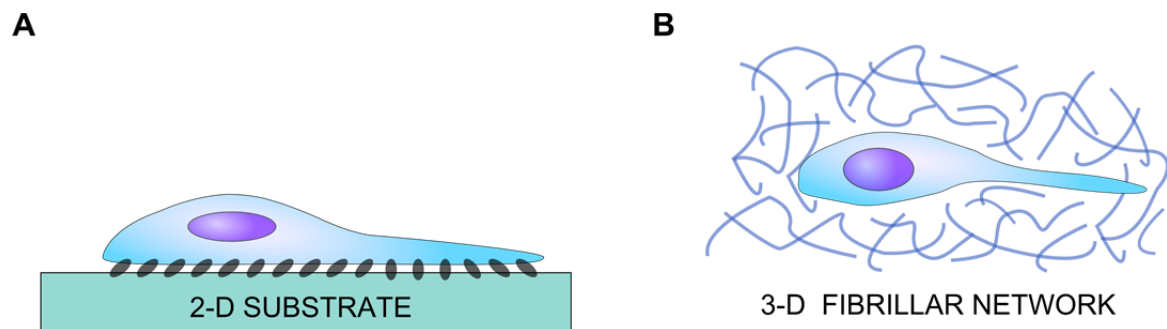


Figure 1.1: Scheme of cell migration in a 2-D and 3-D matrix.

Cell migration on 2-D substrates highly depends on cell adhesion. However, when cells migrate in a 3-D fibrillar network, they become embedded in the scaffold, and passively undergo contacts with surrounding matrix.

How cells regulate this balance is currently still under investigation and debate, but there are at least two main mechanisms postulated: the first is that invading cells degrade the ECM through the production and secretion of proteolytic enzymes that digest the surrounding ECM; and the second mechanism relies on the generation of contractile forces.

In fact, several studies suggest that the invasiveness of cells depends on a combination of both mechanisms, and thus the generation of contractile forces is a parameter that determines the invasion speed and invasion depth of cells. Therefore,

the measurement of contractile forces in 2-D and 3-D environments is important for determining whether a cell invades the surrounding ECM [26, 27].

1.1.2. Cell traction forces

Non-muscle cells contain bundles of actin filaments, or stress fibers (SFs), which form sarcomere-like structures. Powered by adenosine triphosphate (ATP) hydrolysis, the actomyosin crossbridges inside these structures generate tension and contractile shortening that makes cell body contracts [28, 29]. This tension is then transmitted to the ECM, and the force exerted on the ECM is termed cell traction force.

Actin polymerization is a second source for generating cell traction forces (CTFs) that drives forward protrusion of the leading edge of a migrating cell [30, 31]. To transmit the traction forces to the ECM, cells do this through focal adhesions (FAs). FAs are located at both ends of the stress fiber and on the substrate [32] and hence physically connect the actin cytoskeleton to the ECM [33-35].

Focal adhesion sites contain an assembly of ECM proteins, transmembrane receptors, and cytoplasmic structural and signaling proteins (see Figure 1.2), including $\alpha v \beta 3$ and $\alpha 5 \beta 1$ integrins, vinculin, paxillin, talin, zyxin, tensin, protein tyrosine kinases, and phosphatases [36, 37]. Moreover, among these FA proteins, integrins are primary mediators that provide a physical linkage between the actin cytoskeleton and the ECM, and thus play a pivotal role in cellular mechanotransduction [38, 39].

Considerable research has focused over the last years on studying how cells adhere to the extracellular matrix through FAs, and which of the molecular components are responsible for transmitting forces between the cell and the substrate [32, 40-43]. On mature elongated FAs of relatively stationary cells, the magnitude of traction forces linearly correlates with FA size [32, 35]. In particular, as the adhesion sites continue to mature, the traction forces exerted by cells are markedly enhanced. Interestingly, other studies showed that cells also exert appreciable larger forces through small focal complexes (FCs) with an average area of less than $1 \mu\text{m}^2$, where the level of force no longer correlates with adhesion size [35]. In particular, near the leading edge of a migrating cell, such as a fibroblast, small nascent FCs transmit strong propulsive traction forces, whereas large, mature FAs exert weak forces [40]. Therefore, changes in the

structure, molecular composition, and level of phosphorylation that accompany the maturation of FAs result in a shift of its function for transmitting cell forces to the underlying substrate [4, 44].

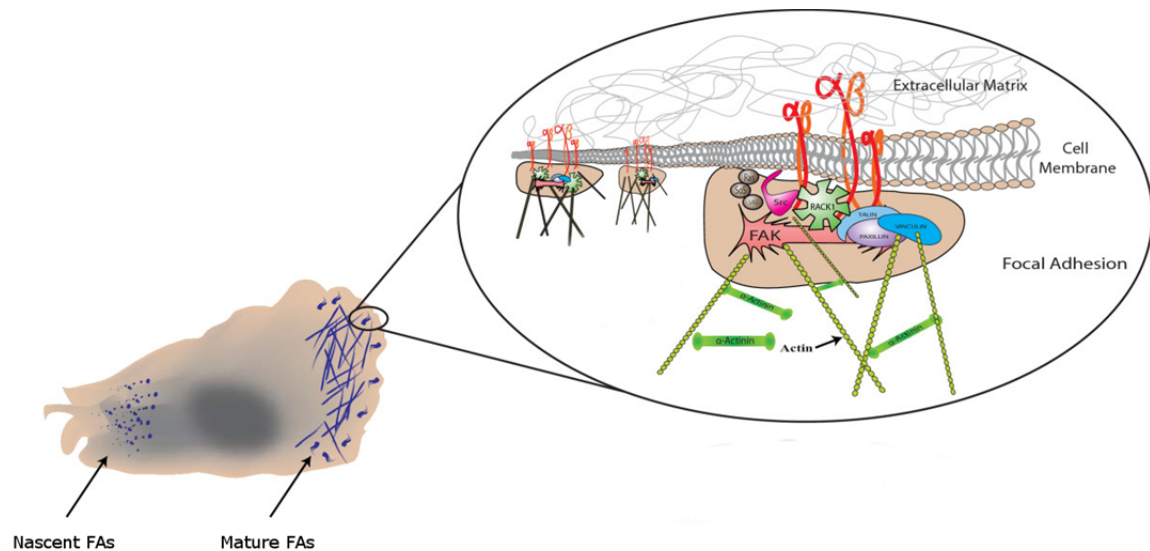


Figure 1.2: Schematic of focal adhesion assembly on a 2-D migrating cell.

When a cell is in contact with the ECM, integrins that are clustered at the cell surface, leading to the recruitment of focal adhesion kinase (FAK) and to the stabilization of FAs. Through focal adhesions sites, cells are able to transmit forces to the substrate. Figure adapted from [45].

Recent work has highlighted the importance of examining adhesions in more physiologic 3-D environments [46-48]. Although the characterization of adhesions in 3-D matrices is in its infancy, available data indicate that adhesions in 2-D and 3-D environments can differ, at least in some aspects. For example, when fibroblasts are plated on 2-D substrates or in 3-D cell- or tissue-derived matrices, FAK was differently phosphorylated in 2-D and 3-D adhesions [46]. Other studies have also shown differences in adhesion signaling, morphology, and composition between 2-D and 3-D [47, 49, 50]. These differences point to the need to better characterize adhesions and other types of cell-matrix interactions in 3-D environments, such as collagen type I matrices.

1.1.3. Biomimetic 3-D hydrogels

The connective tissue forms a mechanically stable support for cells, permits the diffusion of oxygen and nutrients between the microvasculature and adjacent tissues, and enables the trafficking of freely moving cells. The connective tissue is composed of a biopolymer fiber network of proteins, proteoglycans and glycosaminoglycans that differ in composition and structure throughout various parts of the body [51]. Each type of connective tissue in animals has a different composition: collagen fibers and bone mineral comprise the ECM of bone tissue; reticular fibers comprise the ECM of loose connective tissue; and https://en.wikipedia.org/wiki/Blood_plasma fibrin is the ECM of coagulated blood.

The most abundant component of ECM is type I collagen (COL-I), a fibrous protein responsible for giving the stiffness to the ECM [52]. The stiffness and relative alignment of network fibers are particularly important for cell function. In fact, some studies revealed that dense and rigid collagen gels can promote growth and progression of cancer cells and tumors [21, 53]. Other examples are durotaxis in which cells tend to move in the direction of increasing matrix stiffness [54], and contact guidance in which cells tend to align and move in the direction of fiber alignment [55-57].

In the last decades, biopolymer hydrogels have become one of the best studied alternatives to substitute biological tissues in cell culture and tissue engineering [58, 59]. Biopolymer hydrogels consist of a polymer network made of connected individual filaments which are embedded on an aqueous medium. The properties of both individual filaments and the global structure that they form contribute to the global mechanical properties of the hydrogels. Thus, geometrical parameters such as fiber diameter, network pore size, pore-size distribution or fiber length may determine the mechanical, or rheological, properties of the biopolymer network and at the same time cell behavior. Due to their effects on cell behavior and communication, a significant amount of work has been carried out to characterize the structural and physical properties of biopolymer networks [12, 60-64].

To study cell behavior in 3-D microenvironments, the most commonly *in vitro* ECMs used are: collagen type I gels (COL-1), cell-derived matrix (CDM) from fibroblasts,

fibrin gels and basement membrane extract (BME or Matrigel) (see Figure 1.3) [65]. All of them have been used for exploring differences in cell morphology, signaling, adhesions and motility, or even for quantifying cell traction forces, which vary even for the same type of ECM depending on specific properties or whether cells are plated on top or inside the hydrogel.

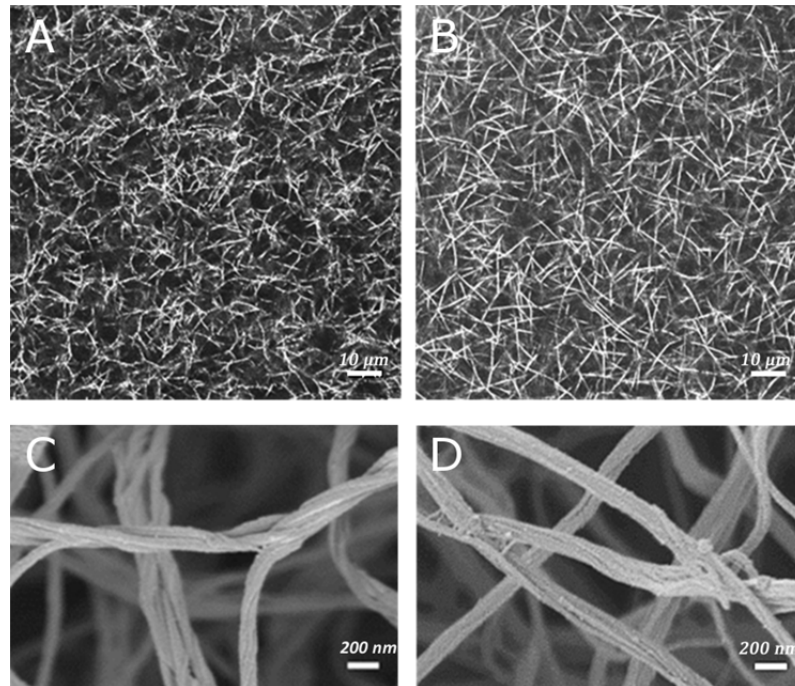


Figure 1.3: Different types of *in vitro* ECMs used for studying cell behavior. Confocal reflection imaging at 120x of: A) a collagen type I hydrogel and B) a fibrin hydrogel. Fiber structure detail imaging, acquired with SEM microscopy of: C) a collagen type I hydrogel and D) a fibrin hydrogel. Figure adapted from [66].

For studying cell traction forces on planar substrates (2-D traction forces), the most commonly used substrates are polyacrylamide-bisacrylamide hydrogels. The main advantage of this synthetic hydrogels is the simplicity for characterizing the mechanical properties, such as the elastic modulus, which is constant over a large range of strain and strain rates.

1.1.4. Microfluidics: A novel technology for studying cell-matrix interactions in 3-D microenvironments

In vitro 3-D research has been rapidly growing in the last years, as it entails a better representation of the microenvironmental conditions of living tissues. The desire to address cell biological questions that cannot be otherwise answered *in vitro*, has led to the development of advanced technologies for real-time *in vivo* imaging [67]. Nevertheless, *in vitro* models are still indispensable to isolate and define specific contributions of single factors to the overall response of a living tissue.

Recent advances in fabrication technology have made it possible to fabricate novel microfluidic devices that allow for precise control of the cellular microenvironment. The incorporation of microfluidic technology to investigate the biological response of cells and tissues to various mechanical stimuli has overcome several difficulties of large-scale *in vitro* experiments, such as the limited control of potentially important physiological factors [68].

Microfluidic systems allow for greater control and versatility for designing and performing experiments and, hence, for creating more realistic *in vitro* models of mechanotransduction in living systems. Additionally, real time monitoring is also facilitated with this technology, so qualitative and quantitative studies in 3-D environments can be performed (see Figure 1.4). Due to all these advantages, microfluidics presents unique opportunities for designing novel physiologically-relevant *in vitro* models, to study mechanotransduction.

In summary, microfluidic culture systems are a useful tool for gaining new insights into the underlying mechanisms by controlling the microenvironmental complexity, which can be applied to a wide variety of *in vitro* studies such as angiogenesis, cultures of organ function or tumor cell migration [69, 70].

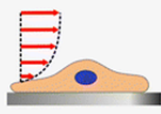
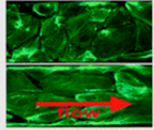
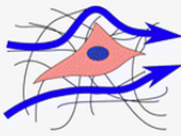
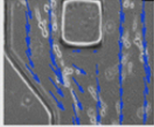
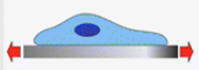
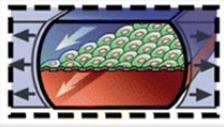
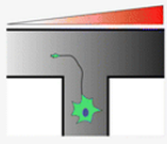
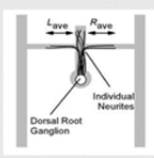

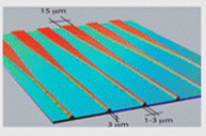
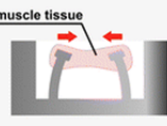
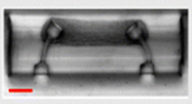
	Types of stimuli	Schematics	Literature examples
A	Shear stress		
B	Interstitial flow		
C	Stretching		
D	Stiffness gradient		
E	Confinement		
F	Force measurement		

Figure 1.4: Different types of Microfluidic devices developed to investigate the biological responses of cells and tissues to various mechanical stimuli.

Type of stimulus induced to the cells (left), schematics of the system (center) and literature examples of microfluidic devices developed (right). A) Fluid flow through confined channels induces a shear stress to the cells, resulting in cell alignment in the flow direction [71, 72]. B) Applying a fluid pressure gradient across a hydrogel allows for the investigation of the effect of interstitial flow on cell migration and alignment [73]. C) By incorporating flexible substrates into microfluidic platforms, devices have been developed to study the effect of mechanical stretch on cells cultured on deformable substrate [74]. D) Gradients in substrates stiffness within a microfluidic device were used to study durotaxis in axon outgrowth [75]. E) Microfluidic systems were used to study the effect of geometric confinement on axon outgrowth [76]. F) Novel devices have been developed to measure the force generated by active cells and tissues, for example in cardiac microtissue grown around two micro-cantilevers [77]. The figure adapted from [68].

1.2. State of the art

Cell traction forces (CTF) are critical regulators of cell adhesion, signaling and function and therefore are crucial in many biological processes such as inflammation, wound healing, angiogenesis and metastasis. Despite their importance, measuring cellular forces in a physiological context and understanding their contribution to biological processes remain challenging.

The concept of traction force microscopy (TFM) was first developed in the 80's by Harris et al. [78], who showed that fibroblast wrinkle an elastic silicone rubber substrate, therefore indicating the mechanical activity of cells. However, this approach showed some difficulties regarding force quantification due to the non-linearities associated with the wrinkling of a thin elastic silicone rubber membrane and the low spatial resolution of the technique [79, 80]. This approach was later refined by combining high-resolution optical imaging techniques and extensive computational procedures, which produced a significative improvement on resolution, accuracy and reproducibility of traction force measurements, thus transforming TFM into a technique with relatively wide use in many biological laboratories, even by using different matrices [34, 81-83].

Several methods have been developed in the last 20 years for measuring forces applied by cells on the surrounding substrate with a significant impact in the biological community (see Figure 1.5). This section discusses the fundamentals and experimental considerations of the different approaches categorizing them according to methods that: methods that measure forces generated by an entire tissue versus those that measure traction forces generated by a single cell [4, 84].

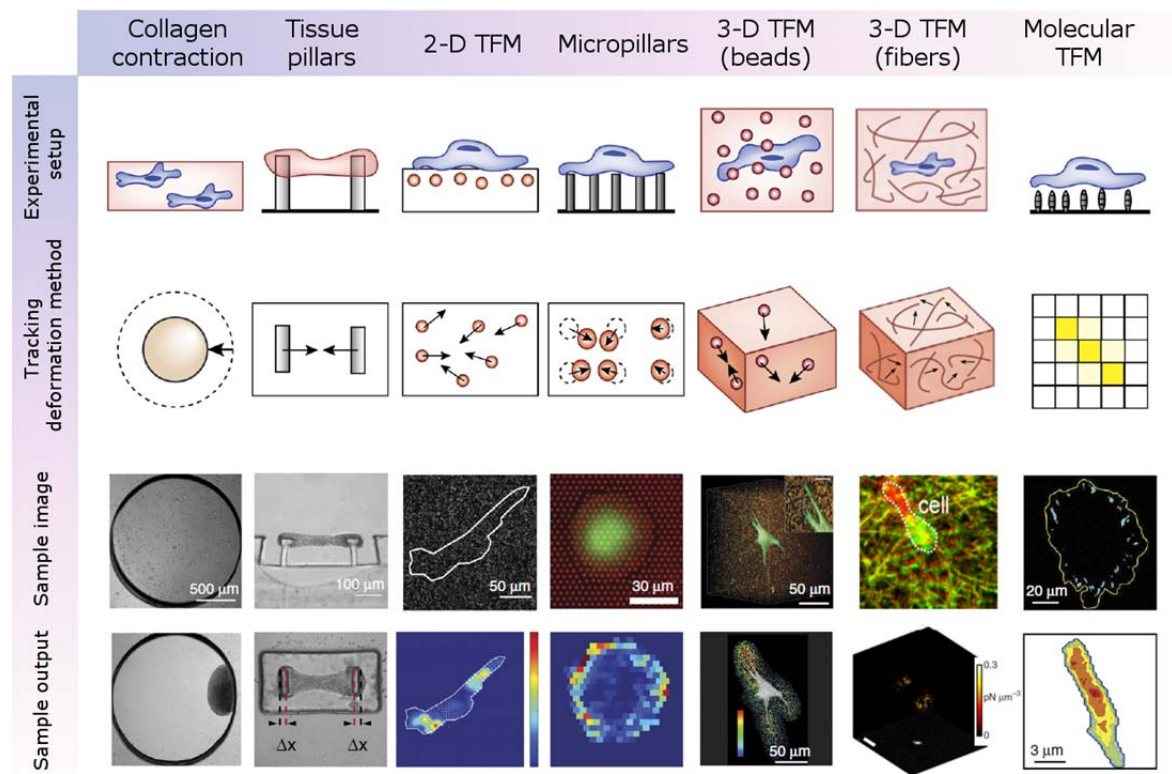


Figure 1.5: Methods for measuring cell traction forces.

Experimental setup, tracking deformation method, sample image and sample output for the most relevant TFM methods for measuring cellular forces on individual cells and tissue. Figure adapted from [84].

1.2.1. Measuring methods of forces generated by an entire tissue

Stromal cells embedded in collagen gels are able to compact the gel over a time course of hours to days, likely mimicking the contractions produced during wound closure process [85-87]. The compaction of a gel with embedded cells in a well can be measured by the change of diameter/shape of the gel. Basically, two general approaches have been used to measure the forces generated when compacting gels.

The first is based on attaching a gel to an isometric force sensor, which changes the resistance or the voltage signal with force (see Figure 1.5, Collagen contraction). The sensors are much stiffer than gels, hence the sensor undergo no displacement as the tissue contracts. These systems have been used for measuring cell forces of different types of contractile tissues, such as skin fibroblasts, cardiac and skeletal myocytes [88-90].

The second approach relies on measuring the displacement induced on deformable cantilevers of known stiffness, during cell contraction [91-93], and to calculate the contractile forces based on beam theory (see Figure 1.5, Tissue pillars). Some of the advantages of this system are that this technique requires less tissue than the previous one, fewer cells, and many cantilevers can be measured simultaneously. The cantilevers are usually microfabricated from a silicone elastomer, such as polydimethylsiloxane (PDMS), which makes it possible to image them with conventional optical microscopy. These systems have become important tools for measuring forces in cardiomyocytes, since this type of cells cannot be isolated and propagated in large numbers [94-96].

1.2.2. Measuring methods of forces generated by a single cell

To quantify cellular tractions of individual cells, these can be determined from a quantitative map of the material deformation and a well defined constitutive relation of the substrate material. During the last years, a variety of techniques have been developed for measuring forces by growing cells on or inside natural and synthetic optically transparent hydrogels, in which fluorescent beads are embedded. Basically, the displacement field of the hydrogel caused by cell tractions is quantified by tracking the positions of the embedded beads before and after the cell tractions are relaxed with a drug cocktail containing trypsin and/or high concentrations of actin-disrupting drugs such as cytochalasin-D. Once the matrix displacements are known, the matrix strain field can be computed. Given the known mechanical properties of the matrix, an inverse algorithm is then used to compute the stress field within the hydrogel.

Implementation of conventional TFM experiments can be achieved at any epifluorescence microscope without additional optical components. However, more advanced microscopy techniques with 3-D resolution, such as confocal microscopy, has allowed for mapping out-of plane tractions with higher resolution. Moreover, a variety of elastic materials and labeling strategies have been explored in order to improve measurement accuracy and to extend the number of biological applications of TFM (see Figure 1.5).

1.2.2.1. Traction forces in two dimensions

This method and its variations remain the most widely used technique for quantifying cell forces. For computing cell forces in two dimensions, cells are usually plated on synthetic deformable hydrogels, such as polyacrylamide-bisacrylamide (PAA, BAA) hydrogels. These substrates are resistant to degradation caused by biochemical factors released by the cells, so that deformation due to cell forces can be decoupled from changes in the local mechanical properties of the gel. Moreover, their mechanical properties are well characterized, as they behave as linear elastic solids under deformations. However, recent studies suggest that degradation and reorganization of the ECM contribute to the traction profile of cells *in vivo* [97, 98].

Once the displacement field is mapped by tracking the fiducial markers embedded in the hydrogel, different computational algorithms are used for recovering cell tractions in the cell-matrix interface (see Fig. 1.5, 2-D TFM). When TFM is applied to a thick, 2-D, linear elastic substrate, the problem of determining cell tractions is achieved by solving an inverse problem. This inverse problem can be solved with Green's functions either in real space or in Fourier space. In real space, this is commonly done using the boundary element method [99-101]. However this solution is further simplified by utilizing the Boussinesq solution in the Fourier space [102]. This technique is often referred to as Fourier Transform Traction Cytometry (FTTC), and yields a rapid solution for the traction field [103]. However, its application is limited to thick 2-D substrates undergoing small strains.

A computationally simpler alternative to TFM on soft elastic substrates is the use of pillar arrays [35, 104, 105]. Pillars can be fabricated from many different materials, such as PDMS, as long as they have a sufficiently high aspect ratio to deform under cellular traction (see Fig. 1.5, Micropillars). Some of these systems integrate electronics that allow forces to be converted to electrical signals directly on chip [106, 107].

Another promising alternative is the use of molecular force sensors [108-112]. These molecular force sensors consist of either a fluorophore and a quencher or a Förster resonance energy transfer (FRET) fluorophore pair separated by an entropic polymeric molecular spring, arranged such that the emission spectra of the fluorophores

shift as a function of strain in the spring (see Fig. 1.5, Molecular TFM). However, these systems present the difficulty to calibrate the conversion of shifts in emission spectra to absolute forces [84].

1.2.2.2. Traction forces in three dimensions

The concept of TFM can also be extended to 3-D measurements. Measuring tractions in three dimensions presents a number of challenges not only because of the requirement of tracking fiducial markers in three dimensions, but also because of the complex mechanical characterization in three dimensions of biological materials used to culture cells, such as reconstituted collagen type I hydrogels.

This problem introduced by Dembo and Wang [100] was first solved by Legant et al. [113], constructing a numerical Green's function by using the finite element method (FEM), that connects the traction applied at a point on the cell-matrix interface to the displacement at a given bead location. Once the beads displacement map is determined, a minimization problem is solved in order to determine the traction field that produces a bead displacement field that best matches the measured displacement field. A similar approach can also be found in [114]. The extension to the ideas described above involves accounting for the non linear behavior of the ECM by implementing a FEM-TFM with a non-linear formulation. Several attempts have been made to solve CTFs on highly non-linear materials [115-117].

Moreover, the role of noise plays an important issue in traction forces reconstruction since most of TFM approaches use an inversion of the elastic problem to obtain the cell forces. In those cases, the solution however is not trivial since a set of equations is usually ill-posed [113], even in the case of 2-D TFM as pointed out by Schwarz et al. [118]. This means that the cellular traction result may not be unique and can be sensitive to measurement errors in the bead displacement data. To ensure robustness of the traction measurement, additional regularization procedures have been developed [118, 119].

For that reason, many methods have adopted the forward computation method, as described in [119]. In this approach, a continuous displacement field is determined

from the bead images (see Fig. 1.5, 3-D TFM from beads) and then directly evaluates the strain and then the stress field by using the constitutive equation [120, 121]. Thus, the quality of the reconstructed forces will depend on the ability to measure the displacement field close to the cell-matrix interface. Alternatively, a recent approach has solved this issue by determining the map of the displacement field in the entire domain as a function of the fibers deformation (see Fig. 1.5, 3-D TFM from fibers), by means of confocal reflection imaging [115].

1.3. Motivation

As described above, studies of cell migration in 3-D cell culture systems and *in vivo* have revealed several differences when compared with cell migration in two dimensions. Recent findings point to substantial dependence of cell behavior not only on the morphological, chemical and mechanical properties of the surrounding environment, but also highlight the importance of the internal mechanical properties of cells when invading 3-D substrates. Particularly in the context of single cell migration, e.g. during wound healing processes or tumor cell invasion, the mechanical interactions of cells with their environment are of great importance. For that reason, these dependencies need to be characterized and understood to successfully relate the results of *in vitro* studies to the potential implications for the physiological processes *in vivo*.

In the last years, collagen gels have become popular as an alternative to conventional cell culture systems, being used for exploring differences in cell morphology, signaling, adhesions and motility, or even for quantifying cell traction forces in 2-D and 3-D microenvironments. However, these biopolymer networks have a complex mechanical behavior that can not be simply explained with conventional mechanical laws. Thus, new *in silico* computational methods developed to explore cell interactions with the surrounding ECM, should use these type matrices and take into account their non-linear behavior.

Additionally, microfluidic platforms have gained popularity due to their unique capability to spatially and temporally control biophysical and biochemical factors in culture, hence, presenting unique opportunities for designing novel physiologically-

relevant *in vitro* models. As far as we know, microfluidic technology has not been used before to explore cell traction forces inside 3-D biopolymer networks.

Thus, the main motivation of this Thesis is to advance towards a better knowledge of how cells use traction forces to invade relevant 3-D biological microenvironments, such as collagen type-I hydrogels. To that end, a novel *in vitro* model has been developed by using microfluidic technology, capable to control the microenvironmental complexity of cells and tissues. Furthermore, different experiments and computational models have been developed with the aim to investigate cell-matrix interactions and in particular focusing on the effect of the mechanical properties of cells and ECM on traction forces exerted by cells. The combination of both experimental and computational studies could provide new insights in the development of therapies and diagnosis techniques, therefore reducing the number of animal studies.

In this context, this Thesis was part of the project INSILICO-CELL *-Predictive modelling and simulation in mechano-chemo-biology: a computer multi-approach* (European Union Starting Grant / ERC-2012-StG - Proposal 306571) whose main purpose is to better understand the cell-cell and cell-environment interactions through the development of *in vitro* models by means of microfluidic technology, with three main applications: wound healing, angiogenesis and bone regeneration.

Additionally, this work is funded with the Government of Aragón (DGA) grant (C126/2015) and European research fund.

1.4. Objectives

Based on the arguments above, the main objective of this Thesis is to advance towards the understanding of how cells exert traction forces in 3-D non-linear matrices, while taken into account the internal mechanical properties of cells. For this purpose, different numerical and computational strategies have been developed for modeling and quantifying cell traction forces in 2-D and 3-D substrates. Moreover, a novel *in vitro* microfluidic-based model and different experimental assays have been performed, for studying cell interactions within 3-D microenvironments.

To reach the main goal above exposed, the following partial objectives have also been achieved:

- Study the effect of physical forces on adherent cells that regulate the formation of cell-matrix adhesions. This includes the development of a computational model to simulate the dynamics of cell-matrix adhesions within the framework of finite element method (FEM) and based on the principles of continuum damage mechanics (CDM).
- Investigate and quantify how different mechanical conditions in the cell (e.g., contractile forces, actin cytoskeletal properties) or in the ECM (e.g., stiffness, external forces) can regulate the dynamics of cell-matrix adhesions.
- Design of an *in vitro* model by using microfluidic technology, to control the microenvironmental complexity of cells cultures and tissues.
- Explore the chemical gradient formation process within these microfluidic devices to assess the diffusion of nutrients to the cells. A FEM was used for simulating the diffusion process within the ECM, and the possible chemotactical and haptotactical cues generated inside them were evaluated. Moreover, a web-based application for automated quantification of chemical gradients induced in microfluidic devices was developed.
- Improve the understanding of cell-matrix interactions in the form of cell traction forces as a function of both cell and matrix mechanical properties, based on real cell geometries and experimental data. For this purpose, a 3-D TFM inverse method has been developed by using a recursive formulation based on finite elements.
- Investigate how cells respond to changes in steric hindrance that arise from altered cell mechanical properties. To that end, different experiments were performed to measure traction forces, morphology and invasiveness of MDA-MB 231 breast cancer cells, by studying two different cases with altered cell mechanical properties.

1.5. Outline

This Thesis is organized into six chapters and an appendix (see scheme of Figure 1.6). Although the contents of each chapter are treated separately, much of the material, by its very nature, is interrelated and requires the consideration of the overall picture. More specifically the Thesis is structured as follows:

- **Chapter 1 (the present one):** serves as an introduction, including the state of the art, motivations, objectives and Thesis organization.
- **Chapter 2** presents a brief overview of the cell-matrix adhesion sites, termed as focal adhesions (FAs). Next, a computational model to simulate the dynamics of cell-matrix adhesions is presented through a cohesive formulation within the framework of the finite element method (FEM) and based on the principles of continuum damage mechanics (CDM). Through this approach it is investigated how different mechanical properties of the cell (e.g., contractile forces, actin cytoskeletal properties) or of the ECM (e.g., stiffness, external forces) can regulate the dynamics of cell-matrix adhesions. Finally, a validation of results and a parameter sensitivity analysis are presented, and the role of cell-matrix adhesions for a whole cell is explored.
- **Chapter 3** introduces a novel *in vitro* model based on microfluidic technology to study cell-matrix interactions inside a 3-D ECM, such as collagen type-I or fibrin hydrogels. First, the chemical gradient formation process within these microfluidic devices is explored using FEM. Secondly, possible chemotactical and haptotactical cues generated inside these microdevices are evaluated. Finally, an intensive multiparametric analysis is carried out for four different microfluidic device geometries, to study the dependence of the gradient formation processes on the geometrical parameters. In addition, a web-based application for automated quantification of chemical gradients induced in microfluidic devices is presented.

- **Chapter 4** is entirely dedicated to the development of an *in silico* model for computing 3-D cell traction forces in non-linear matrices. With this purpose, a novel inverse method is developed by using a recursive formulation and finite element analysis. This new approach is used to simulate different cases where the effect of cell and matrix mechanical properties onto the cell traction force reconstruction is investigated. Finally, the implications and possible developments of the model are discussed.
- **Chapter 5** emphasizes the importance of the cell and matrix mechanical properties on cell migration processes. To that end, it is investigated how cells respond to changes in steric hindrance that arise from altered cell mechanical properties. Different experiments were performed to measure traction forces, morphology and invasiveness of MDA-MB 231 breast cancer cells, by studying two different cases in which cell mechanical properties were altered. The results obtained experimentally are discussed, as well as the possible integration of these effects on the numerical model previously presented.
- **Chapter 6** concludes with a summary of the main achievements of the Thesis and the most relevant conclusions from previous chapters. In addition, the original contributions of the work are reviewed and future research lines are proposed.

Appendix A comprises a summary and the main conclusions of this Thesis in Spanish, which constitutes a necessary requirement to apply for the Internacional Doctor Degree at the University of Zaragoza.



Figure 1.6: Thesis outline.

Chapter 2

MACROSCOPIC SIMULATION OF CELL-MATRIX ADHESION

Cell adhesion is crucial for cells to not only physically interact with each other but also to sense their microenvironment and to respond accordingly. In fact, adherent cells can generate physical forces that are transmitted to the surrounding matrix through the formation and regulation of cell-matrix adhesions. This chapter describes a single cell–matrix adhesion model to investigate the binding dynamics of the adhesion sites and how cells transmit forces to the ECM. The numerical model is presented within the framework of the finite element method and is based on the principles of continuum damage mechanics. Through this approach it is investigated how different mechanical conditions in the cell or in the ECM can regulate the dynamics of cell-matrix adhesion. Finally, a validation of the results and a parameter sensitivity analysis are presented, and the role of cell–matrix adhesions for a whole cell is explored ¹.

¹ This chapter has been published in: M. C ndor and J.M. Garc a-Aznar, *A phenomenological cohesive model for the macroscopic simulation of cell–matrix adhesions*. Biomechanics and Modeling in Mechanobiology, 2017: p. 1-18 [17].

2.1. Introduction

Cell-matrix adhesions are dynamical macromolecular structures that transmit forces from the cytoskeletal actin network to the extracellular matrix (ECM) and vice versa, serving as mechanical links between the cell and ECM [40]. These mechanical connections are fundamental for maintaining tissue integrity and functionality. Therefore, understanding the regulatory role of cell-matrix adhesions is fundamental to unravel more complex biological phenomena, such as tissue regeneration, wound healing, morphogenesis and cancer development [37, 122].

The most relevant characteristic of cell-matrix adhesions is their dynamical and mechanical adaptive behavior, which causes them to grow or shrink as a result of turnover of their component proteins (commonly known as plaque proteins) in response to mechanical stress [123-125]. Different force transmission patterns can be found depending on the origin of the forces, which can be classified into internal (actomyosin-generated) forces or external (exerted by or through the surrounding matrix) forces.

Considerable research has focused on studying how cells adhere to the extracellular matrix through structures known as focal adhesions (FAs) [40, 126-129]. FAs are integrin-based adhesion organelles that physically link the actin cytoskeleton to the ECM through a membrane-associated macromolecular complex [125]. The transmembrane portion of FAs consists of integrin proteins, whereas the interior portion contains anchoring proteins (talin, vinculin, alpha-actinin) that bind to actin filaments in the cell (see Figure 2.1) [130].

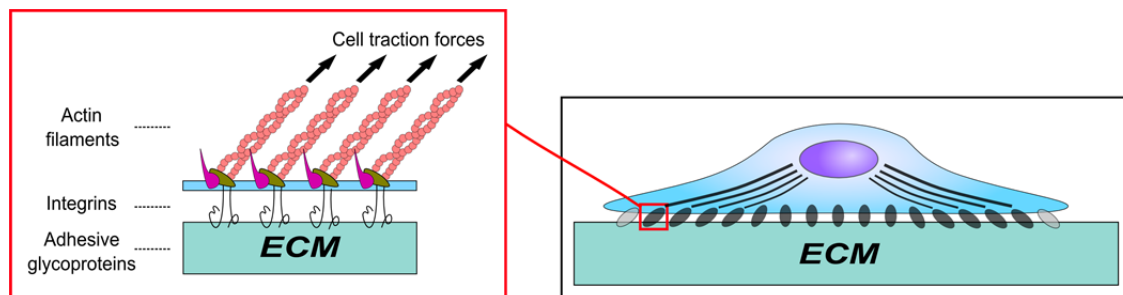


Figure 2.1: Schematic of discrete FAs connecting a cell to an ECM-coated substrate.

These adhesions act not only as mechanical linkers that transmit physical forces between cell and matrix, but also signaling centers that activate certain biochemical signaling molecules that diffuse through the cytoplasm toward the nucleus [131-134]. Various studies have investigated the mechanisms of force transfer through the FAs [32, 135] from the cell to the matrix or vice versa. These adhesions respond to ECM forces by inducing conformational changes in cytoskeletal proteins that mediate further FA dynamics. The growth and resorption strongly depend on the magnitude of the forces [136], which can be generated by either actomyosin contraction or external manipulation of the ECM [32, 41, 137]. Additionally, multiple studies have shown that certain types of cells are able to sense the mechanical properties of the ECM and use this information to regulate the adhesion process [138-141].

FA formation is a dynamic phenomenon characterized in part by actin polymerization and organization [37, 127, 142]. Adhesions initially form at the front edge of the migration direction of the cell in a region called the lamellipodium [143] and detach at the rear edge [144] (see Figure 2.2). These nascent adhesions either disassemble or elongate and grow in a process known as adhesion maturation, which is regulated by an organized 3-D molecular clutch [125]. The lifetime of nascent adhesions is short-lived (approximately 60 s) and is determined by the rate of lamellipodium protrusion; the nascent adhesion turnover is faster when the cell protrudes its leading edge and moves faster [145, 146]. For adhesions that are still attached, the maturation process continues over a relatively long time period during which their molecular constituents change. Finally, the FAs may mature into fibrillar adhesions that represent the endpoint of maturation; these structures play an active role in ECM organization [127, 147].

To address the complexity of this dynamic phenomenon, which is strongly dependent on mechano-chemical conditions, many theoretical and computational cell adhesion models have been developed to explain and predict the adhesion, spread and migration of cells [148, 149].

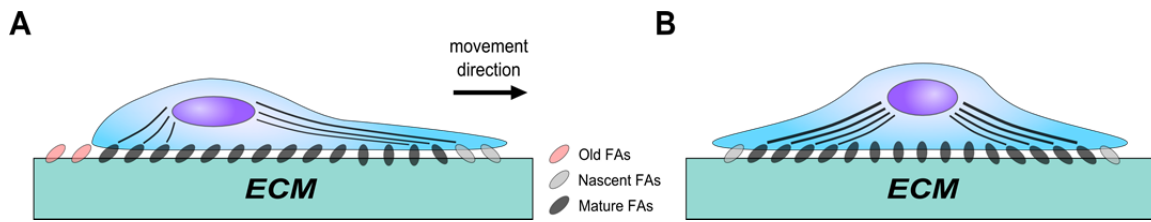


Figure 2.2: Schematic of the evolution of cell-matrix adhesions.

Cell-matrix adhesions evolve as function of cell configuration: A) protruding cell during cell migration; B) static cell adhered to the matrix.

Different mathematical models have aimed to elucidate the biophysics of FAs based on experimental observations at different scales. The first models of cell-matrix adhesions focused on the response of individual ligand-receptor bonds to mechanical cues; these include the models of Bell et al. [150] and Evans [151]. Following these reports, models were proposed by Deshpande et al. [152] and others who assumed that mechanical deformation increases the affinity of bound proteins to their neighbors. These models typically also assumed that the underlying substrate was rigid. Alternatively, models such as those developed by Nicolas et al. [137] and Olberding et al. [153] suggested that adhesion is driven by the minimization of the energy that the cell must provide to maintain a constant stress in the adhesion zone. Wang and Gao [154] treated the clustering of receptor-ligand binding via stability analysis, and Freund and Lin [155] studied the entropic free energy of the binder distribution as part of the total free energy of the system. Furthermore, stochastic models were developed (e.g., by Bruinsma et al. [156]) in which adhesion dynamics were a function of the stress-dependent lifetime of the bond. All these models were based on conformation-induced changes in the affinity of proteins. Shemesh et al. [157] proposed a model of the cell as a mechanosensory system, and the most recent subsequent models [158, 159] have focused more on the actomyosin cytoskeleton than on the ECM because cells respond to the mechanical properties of their environment by adapting their contractility to the resistance they oppose.

Recent work has also focused on modeling the contribution of each intracellular component to the integrated whole-cell response; for example, Chan and Odde [158] studied how cells detect stiffness to modulate their behavior via a stochastic model of force transmission based on a system of springs. Elosegui-Artola et al. [159] extended this approach to incorporate additional phenomena, such as binding dynamics and the recruitment of different integrins to reinforce the adhesion. Paszek et al. [160] demonstrated how integrins could function as sensory molecules that begin responding to matrix properties even before large multi-molecular adhesion complexes are assembled. A more recent approach, proposed by Escribano et al. [43], models the actin retraction velocity and adhesion size based on a Langevin approach. Although these models predict experimentally observed adhesion dynamics with good accuracy, they are based on a local approach that focuses on only a small part of the cell domain. Only some works have taken into account the total cell domain, as Ronan et al. [161] who studied the changes on the stress fiber and the focal adhesion formation as a function of the evolution of each integrin-ligand bond undergoing stretch on the interface area. Nevertheless, these studies do not consider the effect of other biomechanical processes as the adhesion reinforcement or the failure phenomena.

In this chapter, a formulation is proposed and computationally implemented to simultaneously simulate the coupled dynamics of cell-matrix adhesion and cell contraction, considering the cell as a whole. With this spatiotemporal simulation, we seek to understand how the force transmission from the FA molecular clutch to the ECM mediates the physical connection between the cytoskeletal actin and the ECM.

2.2. Cell-matrix adhesion model

In this section is introduced a mechanistic formulation for simulating cell-matrix adhesive behavior based on the mathematical theory typically used to model cohesive interfaces in standard engineering materials [162-164]. To do this, a continuous 2-D or 3-D phenomenological model is proposed to simulate the molecular adhesion of integrins to associated linker proteins within the ECM and the binding dynamics of these integrin-ligand bonds.

In the following subsections, is presented the constitutive law governing adhesion behavior, followed by the definition of internal variables and the mechanical stimuli that drive its temporal evolution. Next, binding-unbinding criteria are proposed to determine the spatiotemporal behavior of the adhesion, followed by the adhesion mechanical failure criterion and the reinforcement criterion. Finally, the numerical implementation of the proposed model is presented.

2.2.1. Constitutive law for mechanical adhesion

Recent advances in light microscopy have allowed the characterization of the protein distribution in FAs at the nanoscale level, which has revealed that nature FAs are vertically stratified along the axis perpendicular to the ventral plasma membrane [125, 130]. Therefore, given this stratified character, a cohesive zone model is an accurate approach to simulate the three-layered architecture of FAs, distinguishing among actin cytoskeleton, FA clutch molecules and ECM.

In addition, this mechanical adhesion is dependent on the number of recruited integrins on the cell surface that bind directly to the matrix. So, the multiple weak interactions generated by binding of thousands of integrin molecules to extracellular matrix proteins allow a cell to remain firmly anchored to the matrix. On the contrary, weak cell-matrix interactions occur when cells are migrating which requires creating and breaking specific contacts with the matrix. Therefore, cell-matrix adhesion is modulated by changes in the number of binding integrins to the matrix, regulating the adhesion degree. Hence, this phenomenon can be described by means of a cohesive interface with constitutive equations based on continuum damage mechanics, where the adhesion degree can increase or decrease, modeling the macroscopic dynamics of integrin binding/unbinding events [165].

The model is established in terms of interface relative sliding δ (also referred to as the jump of displacements between the cell and ECM surface) and interface tractions \mathbf{t} . We define a local reference system at the interface, assigning the 1-axis to the normal direction to the interface and the 2- and 3-axes to the tangential directions (see Figure 2.3A).

For simplicity, it is assumed that the cell-matrix adhesion exhibits linear elastic behavior² with respect to the associated relative displacement in both the normal and tangential directions (see Figure 2.3). Therefore, the constitutive relationship between tractions \mathbf{t} and relative sliding $\boldsymbol{\delta}$ of the adhesion complex is defined as:

$$\mathbf{t} = \mathbf{k} \cdot \boldsymbol{\delta} \quad (2.1)$$

where \mathbf{k} is the initial linear stiffness of the adhesion complex, which depends on the level of adhesion generated between the cell and matrix.

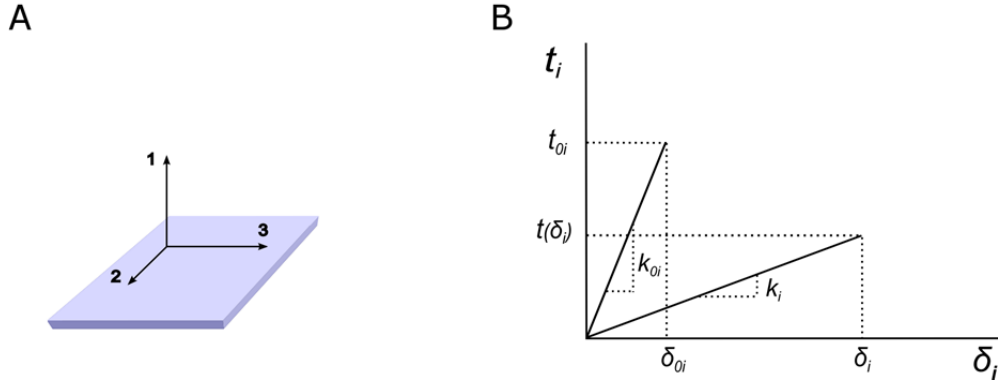


Figure 2.3: Interface constitutive model.

A) Local reference system at the interface. B) Constitutive-law representation of the stiffness variation for an individual cell-matrix adhesion.

To study how rapidly cells bind to the ECM and how long they remain bonded, we have defined an internal variable β that represents the degree of adhesion (DOA) between the cell and matrix. Therefore, $\dot{\beta}$ represents the rate of surface-bound receptor-ligand binding, corresponding to the area density that is capable of sustaining and transmitting forces through the cell-matrix interface. The adhesion level can vary between 0 and 1: a value of $\beta = 0$ implies that all receptor-ligand complexes are broken and thus that the adhesion is completely separated, whereas a value of $\beta = 1$ implies that all receptor-ligand complexes are bound and the cell is completely attached to the ECM.

² This linear elastic assumption could be replaced with a non-linear law if required; as a first approach, however, a linear elastic behavior is assumed.

In this manner, the initial linear stiffness of the adhesion can be expressed as a function of the DOA β and the stiffness of the completely bonded adhesion k_0 :

$$\mathbf{k} = \beta \mathbf{k}_0 = \beta \begin{pmatrix} k_{on} & 0 & 0 \\ 0 & k_{ot} & 0 \\ 0 & 0 & k_{ot} \end{pmatrix} \quad (2.2)$$

The adhesion was defined to exhibit the same mechanical behavior in both tangential directions (k_{ot}), which is different from the normal behavior under traction forces (k_{on}). Therefore, the adhesion model is formulated in terms of the normal and tangential traction components and their corresponding relative displacements. It is assumed that the n-axis is the normal direction and that the t-axis is the tangential direction of this relative displacement.

2.2.2. Mechanical stimuli that regulate adhesion

The elastic free-energy potential of the cell-material adhesion in each direction is defined as a function of the relative sliding δ and the DOA β as follows:

$$\psi(\delta, \beta) = \frac{1}{2} \mathbf{t} \cdot \boldsymbol{\delta} = \frac{1}{2} \boldsymbol{\delta} \cdot \mathbf{k} \cdot \boldsymbol{\delta} = \frac{1}{2} \boldsymbol{\delta} \cdot \beta \cdot \mathbf{k}_0 \cdot \boldsymbol{\delta} \quad (2.3)$$

The differentiation of ψ with respect to the independent variables δ and β provides the associated thermodynamic variables:

$$\mathbf{t} = \frac{\partial \psi}{\partial \boldsymbol{\delta}} = \mathbf{k} \cdot \boldsymbol{\delta} = \beta \cdot \mathbf{k}_0 \cdot \boldsymbol{\delta} \quad (2.4)$$

$$\mathbf{Y} = \frac{\partial \psi}{\partial \beta} = \frac{1}{2} \boldsymbol{\delta} \cdot \mathbf{k}_0 \cdot \boldsymbol{\delta} \quad (2.5)$$

In this model, the variables (\mathbf{t}, Y) , which modulate adhesion, are considered to be fundamental variables thermodynamically associated with the independent variables (δ, β) ³, analogous to the classical theory of inelasticity [166].

2.2.3. Binding/unbinding criteria

The degree of cell-matrix adhesion is assumed to be regulated by the adhesion-transmitted force. As a result, the amount of adhesion temporally evolves in such a way that it increases if the associated energy exceeds a critical threshold; otherwise, it decreases. The underlying biophysical mechanism is based on Bell's theory [150], proposed to consider the kinetics of force-induced bond rupture between a single receptor-ligand pair. Therefore, the binding/unbinding criteria that regulate the spatial-temporal evolution of adhesion formulated in the Y domain is defined as:

$$\begin{aligned} f_b(Y) &\leq 0 && \text{binding process occurs} \\ f_u(Y) &\leq 0 && \text{unbinding process occurs} \end{aligned} \tag{2.6}$$

where f_b and f_u correspond to the criteria that regulate the binding and unbinding process respectively.

FA dynamics occur over different regimes, as previously noted, and new adhesions formed during cell sliding are associated with a binding process and the rupture of old cell-matrix adhesions with an unbinding process mediated by traction/shear forces.

³ The time evolution of the free energy can be evaluated as:

$$\dot{\psi}(\delta, \beta) = \frac{\partial \psi}{\partial \delta} \cdot \dot{\delta} + \frac{\partial \psi}{\partial \beta} \cdot \dot{\beta} = \mathbf{t} \cdot \dot{\delta} + Y \cdot \dot{\beta}$$

Where \mathbf{t} and Y are the thermodynamically variables associated to the independent variables δ and β .

Thus, the following function⁴ is proposed as a macroscopic criterion to regulate the binding or adhesion process f_b :

$$f_b(Y) = (Y_{\text{lim}} - Y) - K_B T \exp\left[(Y_{\text{lim}} - Y) / K_B T\right] \quad (2.7)$$

where K_B is Boltzmann's constant, T is the temperature and Y_{lim} the energy barrier.

In addition, the unbinding function or adhesion removal f_u is defined as:

$$f_u(Y) = K_B T \exp\left[(Y - Y_{\text{lim}}) / K_B T\right] - (Y - Y_{\text{lim}}) \quad (2.8)$$

The threshold value Y_{lim} defines the different states in which the cell-matrix adhesion can be found and characterizes the transition between the bound and unbound states. Binding (or adhesion) occurs when the global mechanical contribution to the adhesion is positive and unbinding occurs or the FA is removed when the contribution is negative or equal to 0. In both cases, the corresponding DOA evolves according to the evolution law defined in section 2.2.4.

The mechanical threshold Y_{lim} represents the minimum energy required to activate the binding kinetics of receptor-ligand complexes and corresponding regulation of macroscopic cell-matrix adhesion. The limit of mechanical potential Y_{lim} is calculated as an estimate from [153] based on the hypotheses that no adhesion occurs for low loads (or in the absence of loads) and that a certain value of applied force activates binding kinetics.

⁴ This function is based on Bell's theory for modulating cell-cell and cell-matrix adhesion by means of forces. A similar expression was proposed by Olberding [153] and Bell [150].

2.2.4. Temporal evolution of the DOA

The temporal evolution of the DOA β is determined by the mechanical binding/unbinding process, which may involve an increase or decrease in DOA β [166], as can be observed in Figure 2.4.

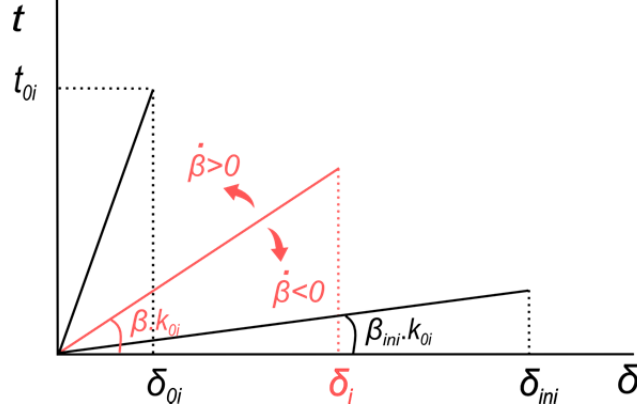


Figure 2.4: Schematic of evolution of the adhesion degree on time. Graphic representation of the evolution of state variable β as determined by the mechanical binding ($\dot{\beta} > 0$) or unbinding ($\dot{\beta} < 0$) process.

Therefore, the evolution law of the DOA β arising from mechanical factors is formulated as a function containing two terms associated with the binding and unbinding process following an associative flow rule [166]:

$$\dot{\beta} = \mu_u \frac{\partial f_u}{\partial Y} - \mu_b \frac{\partial f_b}{\partial Y} \quad (2.9)$$

where μ_u and μ_b are the unbinding and binding consistency parameters, which are assumed to obey the following Kuhn-Tucker complementary conditions:

$$\mu_b, \mu_u \geq 0; \quad f_b(Y), f_u(Y) \leq 0 \quad \text{and} \quad \mu_b \cdot f_b(Y) = \mu_u \cdot f_u(Y) = 0 \quad (2.10)$$

Hence, the flow rules for binding/unbinding process are defined as:

$$\frac{\partial f_b}{\partial Y} = -\left(1 - \exp\left[-(Y - Y_{\text{lim}})/K_B T\right]\right) \quad (2.11)$$

$$\frac{\partial f_u}{\partial Y} = \left(\exp \left[(Y - Y_{\text{lim}}) / K_B T \right] - 1 \right) \quad (2.12)$$

Cell-matrix adhesion is considered a time-dependent problem. This condition is defined by providing the constitutive equations for the consistency parameters $(\mu_b = \kappa_b; \mu_u = \kappa_u)$ and omitting the Kuhn-Tucker conditions (Equation 2.10). Actually, this process known as viscous regularization [166] provides the rate-dependent law for the adhesion degree:

$$\text{BINDING:} \quad \dot{\beta} = \kappa_b \left(1 - \exp \left[-(Y - Y_{\text{lim}}) / K_B T \right] \right) \quad (2.13)$$

$$\text{UNBINDING:} \quad \dot{\beta} = \kappa_u \left(\exp \left[(Y - Y_{\text{lim}}) / K_B T \right] - 1 \right) \quad (2.14)$$

where κ_b and κ_u are the binding and unbinding kinetic coefficients respectively.

2.2.5. Mechanical failure of the adhesion

It is assumed that the detachment of the cell from the ECM can arise through two different mechanisms. First, the cell may detach from the matrix progressively, as modeled by the unbinding equations presented in the previous subsection, particularly in Equation 2.12 (Figure 2.4). Second, the cell may be separated from the matrix instantaneously, which occurs when a sufficiently high force is applied to the interface. In the second case, instantaneous mechanical failure occurs when the applied force t_i ($i=n$ or t , depending on whether the force acts in the normal or tangential direction) is higher than the maximum strength $t_{i,\text{max}}$ supported by the total number of bonds that define the adhesion zone (Figure 2.5B). To differentiate the types of failure that can arise, failure is classified as Mode I if it occurs in the normal direction and Mode II if it occurs in the tangential direction. Accordingly, we propose the following mechanical failure law for each direction i :

$$f_{\hat{i}}(\delta_i, \beta) = t_i - t_{i,\text{max}} = \beta \cdot k_{0,ij} \cdot \delta_j - t_{i,\text{max}}(\delta_i) \quad (2.15)$$

This mechanical failure law is dependent on the maximum strength $t_{i,\max}$ characteristic of the adhesive interface. This property is assumed to be linear with the relative displacement (δ_i) , as it is shown on Figure 2.5, and it follows the linear expression:

$$t_{i,\max}(\delta_i) = \frac{t_{oi}(\delta_{ci} - \delta_i)}{\delta_{ci} - \delta_{oi}} \quad (2.16)$$

where t_{oi} is the maximum strength, δ_{oi} is the displacement at maximum strength and δ_{ci} is the maximum allowable displacement of the adhesion complex when it breaks.

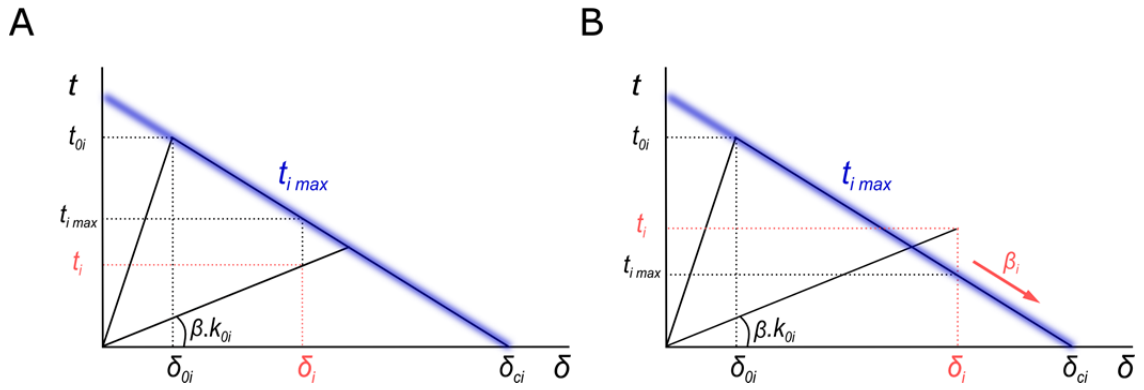


Figure 2.5: Schematic of cell-matrix detachment process.

Graphical representation of the cell detachment process from the extracellular matrix, when: A) $t_i < t_{i,\max}$ and f_{fi} is smaller than zero the cell is binding/unbinding to the matrix progressively and B) $t_i > t_{i,\max}$ and f_{fi} is greater than zero an instantaneous mechanical failure of the cell-matrix adhesion is produced and reinforcement mechanism is activated.

Thus, a failure criterion is added that regulates the mechanical failure process of the adhesion, forcing β to fall to zero when the failure function f_{fi} is larger than zero, as shown in Figure 2.5B.

2.2.6. Reinforcement criterion

When an instantaneous mechanical failure of the interface occurs, the DOA β decays up to zero, the force on the substrate is released and the adhesion is not more able to transmit forces to the matrix ($\beta = 0$). After this failure event, it has been experimentally

observed [159] that an increase of the integrin density is produced at the cell membrane, inducing an increase of the capacity of the adhesion to transmit forces.

To simulate this adhesion reinforcement mechanism we compute the adhesion degree through the temporal evolution of the DOA β as:

$$\text{REINFORCEMENT:} \quad \dot{\beta} = \kappa_r \left(1 - \exp \left[- (Y - Y_{\text{lim}}) / K_B T \right] \right) \quad (2.17)$$

where κ_r is the reinforcement kinetic coefficient, which is higher than the binding kinetic coefficient κ_b .

Once the reinforcement process occurs, the temporal evolution of the DOA β is again calculated through equation 2.9.

2.2.7. Numerical implementation

The mechanical cell-matrix adhesion model has been numerically implemented via the FEM based on an incremental loading approach through the user routine UMAT (User Defined Material) in the commercial code of ABAQUS 6.13. With this routine, the mechanical constitutive behavior of the interface can be defined for each integration point of the adhesion region via the solution-dependent state variables.

The UMAT subroutine is run for each interface element that simulates cell-matrix adhesion behavior. It has been implemented using an incremental loading approach that is evaluated for each integration point individually at each interface element, as shown in Figure 2.6.

The simulation starts with an initial value of the DOA β_{ini} , which means that cell and material are initially separated. The solution is assumed to be known up to a certain point in time t_n , so that for the time increment $\Delta t_n = t_{n+1} - t_n$, the external force increment vector applied to the model is $\Delta F_n^{\text{ext}} = F_{n+1}^{\text{ext}} - F_n^{\text{ext}}$. For each load increment, a displacement increment is obtained for each integration point ΔU_n^i . Using the equations given above and as a function of the mechanical stimuli t_i and Y_i , the DOA is calculated between the cell and matrix under static loads β_{n+1}^{i+1} , as well as the tractions

generated at the interface elements t_{n+1}^{i+1} and the stiffness matrix k_{n+1}^{i+1} . This process is repeated until convergence is achieved for each load increment.

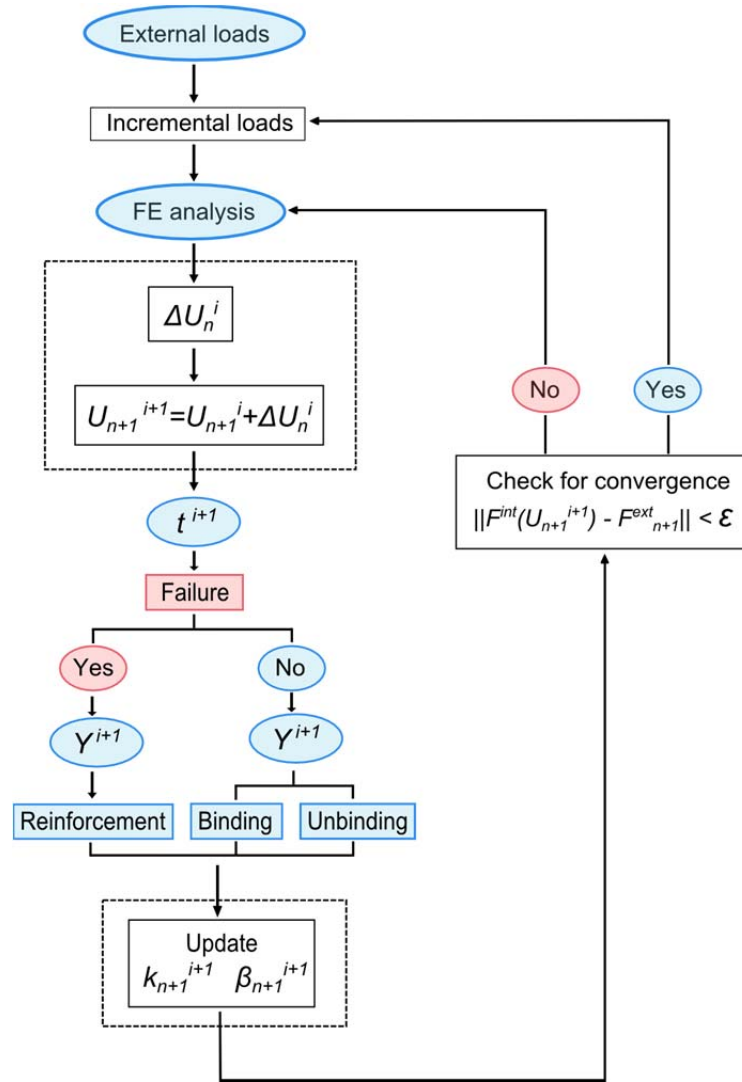


Figure 2.6: Iterative incremental-load algorithm.

2.3. Theoretical model validation: Local modeling of the dynamics of cell-matrix adhesion

To evaluate the predictive capacity of the theoretical model here presented, a simplified 3-D model was created that simulates the local cell-matrix interaction at a single filopodium. To that end, various loading conditions are applied to simulate cell contractility and analyze the adhesion behavior by identifying growth or resorption at the interface as predicted by the evolution of the DOA β .

2.3.1. Description of the finite element model and model parameters

Adhesion is simulated by creating a thin layer of interface elements between the cell and ECM to investigate mechanical adhesion behavior. To evaluate the usefulness of the theoretical model proposed here, a FEM was created with which it is possible to simulate different cell-matrix adhesion conditions. The model consists of three layers (actin, clutch molecules and ECM) that correspond to different materials and that contain in total 10 interface elements and 30 hexahedral elements. Of the hexahedral elements, 10 simulate the cytoskeleton (mainly the actin filaments), and the remaining 20 are located at the bottom part of the model to simulate the extracellular matrix or substrate (see Figure 2.7B).

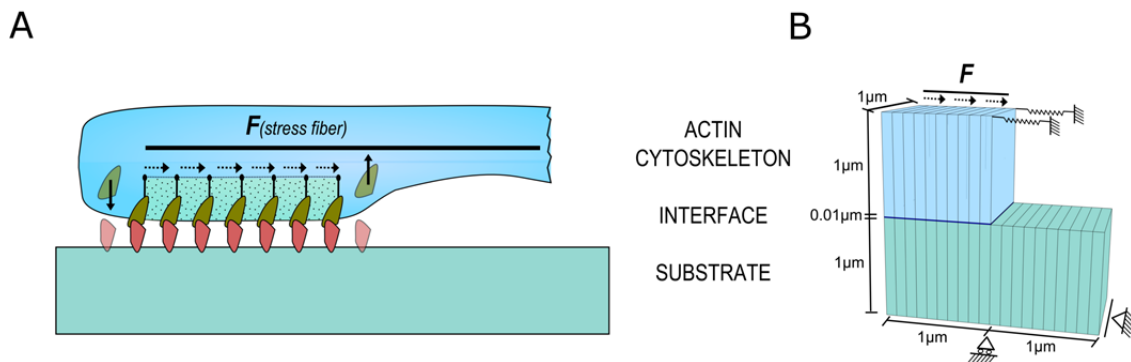


Figure 2.7: Schematic of the FEM used for simulating the local cell-matrix adhesion. A) Schematic and B) FEM of the cell-matrix adhesion of a single filopodium.

This model considers that myosin motors are pulling on actin filaments (force applied on the upper layer of the model), generating the characteristic rearward flow of actin towards the cell center. The interface layer represents the different integrins which are connected to the actin flow through adaptor proteins, competing for binding to substrate molecules with an effective degree of adhesion β . These clutch molecules (the interface layer) are at the same time connected to a compliant substrate. Once the DOA β begins to grow up, myosin forces are transmitted to the substrate through the interface layer or adhesion.

To regulate the actin flow velocity and to avoid the rigid body movement of the actin elements (upper layer of the model), we introduce a pair of springs into the FEM configuration (see Figure 2.7B). The spring constant is set to 700 pN/ μ m, which ensures that when a 150 pN force is applied with a Young's modulus of 100 Pa for the substrate, the resulting actin retrograde flow rate replicates experimental values obtained by Chan and Odde [158] and Elosegui-Artola et al. [159]. Therefore, these springs provide a linear force-velocity relation between the myosin force and actin retrograde speed according to the literature.

In all simulations, the values of different parameters that define the mechanical properties of the cell and the substrate are taken from previous studies simulating cell-matrix adhesion [159, 167, 168]. As a first approach, we use an elastic modulus of 1 GPa and a Poisson's ratio of 0.49 for the actin cytoskeleton [169] to ensure an appropriate load distribution along the surface, according to previous modeling works [158, 159]. With regard to the matrix properties, we apply a range of Young's modulus values between 100 Pa (i.e., relatively compliant) and 100 kPa (i.e., relatively stiff), as detailed in the relevant sections.

The parameters that define cell-matrix interface behavior are listed in Table 2.1. All interface model parameters were held constant in all simulations. The value for the limit potential (Y_{lim}) corresponds to the energy barrier to bond breakage, which can be modified by a suitably oriented force as proposed by Bell [150]. For the values listed in Table 2.1, we consider that unbinding kinetics is activated for an energy limit potential of $Y_{\text{lim}} = 1 \text{ pN} \cdot \mu\text{m}$, consistent with the value presented by Olberding et al. [153]. With

regard to the binding and unbinding coefficients, those were adjusted to match the cell-matrix adhesion dynamics observed in the studies of Chan et al. [158] and Elosegui et al. [159]. The value of the reinforcement coefficient (κ_r) was estimated as twenty times the binding kinetic coefficient, to induce an increase of the capacity of the adhesion to transmit forces.

Parameter	Description	Value	Remarks
k_{on}	Initial normal linear stiffness	10 nN/ μ m	§ [159]
k_{ot}	Initial tangential linear stiffness	1 nN/ μ m	* as 0.1 k_{on}
t_{on}	Apparent strength for the normal direction	1000 pN/ μ m ²	§ [32, 153]
t_{ot}	Apparent strength for the tangential direction	100 pN/ μ m ²	* as 0.1 t_{on}
δ_{cn}	Max. normal adhesion relative displacement	1 μ m	§ [170]
δ_{ct}	Max. tangential adhesion relative displacement	1.02 μ m	§ [170]
δ_{oi}	Normal/Tangential disp. at maximum strength	0.1 μ m	= t_{oi} / k_{oi}
Y_{lim}	Limit potential	1 pN. μ m	§ [153]
K_B	Boltzmann's constant	1.380648 ⁻⁵ pN. μ m/K	---
T	Temperature	310 K	---
κ_b	Binding kinetic coefficient	0.1 s ⁻¹	*
κ_u	Unbinding kinetic coefficient	0.01 s ⁻¹	*
κ_r	Reinforcement kinetic coefficient	2 s ⁻¹	* as 20 κ_b

Table 2.1: Major parameters that define the interface adhesion model.

In the table n and t refers to normal and tangential directions, respectively.

* Estimated / Adjusted parameters

§ Parameters derived from the referenced manuscript

2.3.2. Numerical results and sensitivity analysis

The simple FE model described above provides a tool to test how different mechanical and loading conditions can regulate the mechano-sensitive dynamics of adhesions. Next, it is described the different conditions used to simulate various application examples, as well as the results achieved for each example.

2.3.2.1. Influence of substrate stiffness on cell-matrix adhesion

As proposed in the spring-based models by Chan and Odde [158] and Elosegui-Artola et al. [159], matrix stiffness can regulate the loading rate of cell-substrate forces and the molecular unbinding rates. Therefore, the influence of matrix stiffness on FA formation/resorption is evaluated to predict traction force dynamics and the influence of substrate stiffness on actin retrograde flow speed and traction forces.

In this first approach, a simple load case of a filopodium is simulated by applying force in the shear direction onto the top elements of the model that correspond to actin filaments. With this simple model, we are able to quantify the temporal evolution of the DOA and the actin flow velocity in response to different degrees of substrate stiffness. To this end, different substrates have been simulated with Young's modulus values between 100 Pa (i.e., relatively compliant) and 100 kPa (i.e., relatively stiff) to examine how forces develop within adhesions as a function of substrate stiffness.

In these simulations, an increasing shear force is applied for a time of 1 second with a final magnitude of 150 pN distributed over a $1 \mu\text{m}^2$ area, consistent with the experimental data of Chan and Odde [158]. It is assumed that the cell is initially barely adhered to the substrate, with $\beta = 0.01$, and is exerting essentially zero traction force on the substrate.

Figure 2.8 depicts model predictions in the form of evolving actin flow velocity (Figure 2.8A) and the distribution of the DOA β over the interface elements (Figure 2.8B) at the end of each time increment as a function of substrate stiffness. The actin flow velocity refers to the maximum displacement of the actin elements of the model per second. Cases 1, 2, 3 and 4 correspond with the results obtained from the simulations with ECM Young's elastic moduli of 7, 15, 30 and 50 kPa, respectively.

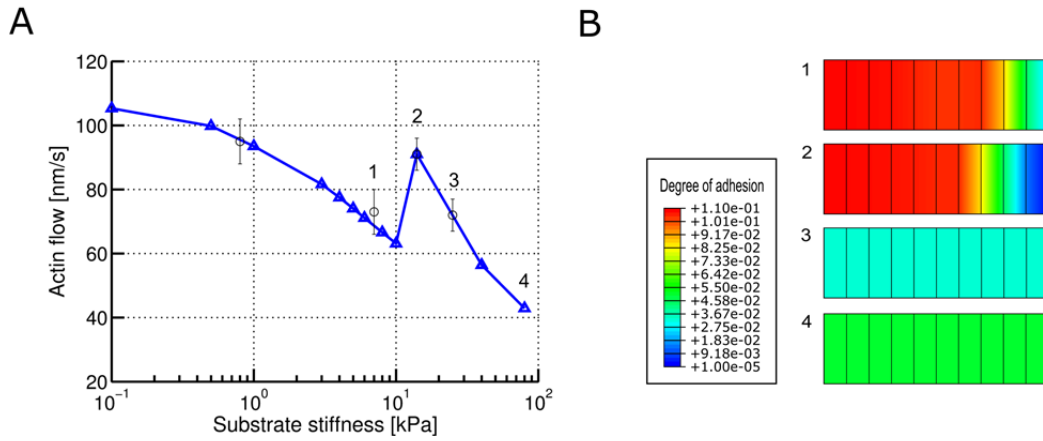


Figure 2.8: Influence of substrate stiffness on cell-matrix adhesion.

A) Actin flow velocity as a function of substrate stiffness (blue triangles and line) and experimental values obtained by Elosegui-Artola et al. [159] for cells with adhesion mediated by $\alpha_v\beta_6$ integrins (black circles). B) Distribution of the DOA in response to changes in substrate stiffness.

To test our model, first is considered the case presented by Elosegui et al. in which cell-substrate adhesion is mediated by the $\alpha_v\beta_6$ integrins. The results presented in Figure 2.8 reveal how cells respond differently to different substrate stiffness values, which produce significant changes on the dynamics of cell-matrix adhesion. As can be observed, three different regimes appear in response to the increasing cell-substrate forces. In the first regime, corresponding to low substrate stiffness, the cell is barely able to transmit loads to the matrix, and existing bonds detach before they can sustain high forces. In this regime, the actin flow velocity decreases monotonically as the DOA increases. With further increases in substrate stiffness beyond 5 kPa, the cell is now able to transmit loads to the substrate, and bonds break faster than they can form because the substrate begins to deform (Case 1). This process continues up to a certain stiffness value (beyond 10 kPa), at which point the kinetics is dominated by the unbinding process, causing a slight increase in actin flow velocity and a decrease in the DOA (Case 2). These characteristics mark the second regime which corresponds with the failure of the interface. Finally, a third regime is reached that exhibits a faster decline in actin flow velocity and rapid and uniform growth of the DOA, the consequences of improved force transmission to the deforming substrate. This phenomenon, called the rebinding or reinforcement process, can only occur once all the interface elements have been separated by failure. Continued force transmission generated after the rupture of the

adhesion complexes is the hallmark of this rebinding process (Cases 3 and 4). In this region, an inverse relationship exists between the actin flow velocity and the transmitted forces.

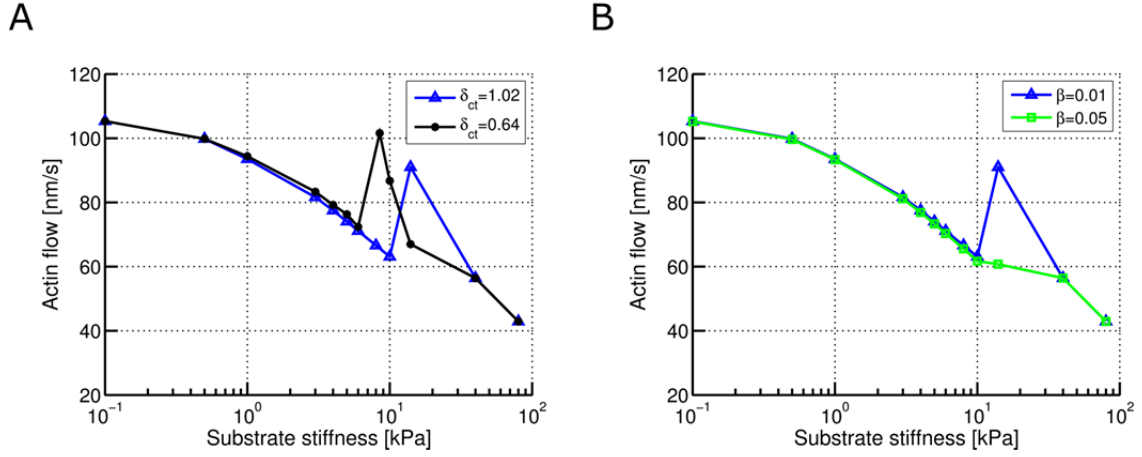


Figure 2.9: Influence of integrin type on cell-matrix adhesion.

Changes on actin flow velocity as a function of substrate stiffness by modifying: A) the maximal tangential adhesion relative displacement δ_{ct} and B) the initial degree of adhesion β_{ini} .

Next, it is tested whether the model is able to reproduce the different experimental values presented by Elosegui et al. [159], in which the cell-substrate adhesion is mediated by two different single integrin types: $\alpha_5\beta_1$ and $\alpha_v\beta_6$. The model predictions depicted on Figure 2.9A show how both integrins behavior can be captured by the model, by changing the maximal tangential relative displacement δ_{ct} and keeping all other parameters constant. The change of this parameter leads to an overall shift on the actin flow-substrate stiffness curve to the left, when this value is slightly reduced. Thus, simply changing this interface parameter that characterizes the mechanical failure of the interface is possible to simulate different integrin binding phenomena.

In contrast, to reproduce the case presented by Elosegui et al. [159] when cell-substrate adhesion was mediated by both integrins, it was not possible to capture this monotonic decrease by only changing the mechanical interface parameters. Therefore, to capture this behavior it is necessary to change the initial adhesion degree of the interface β_{ini} , increasing to fivefold the value of the initial degree of adhesion, and keeping all other parameters constant (Figure 2.9B).

This model demonstrates that for a certain range of substrate stiffness that cells can sense, cells exert larger forces when connecting with stiffer substrates. Thus, as has been observed in many studies, substrate stiffness can modify how traction force components are transmitted by the cell and how they induce directional cell migration on intermediate-stiffness substrates.

2.3.2.2. Influence of substrate stiffness on adhesion rupture

To study how substrate force transmission affects the lifetime of cell-matrix adhesions, a second case is presented in which the influence of substrate stiffness on FA rupture under a constant force is simulated.

A sensitivity analysis was performed to define the cell-matrix response to a change in substrate stiffness. To this end, an increasing shear force is applied with a final magnitude of 150 pN distributed over a $1 \mu\text{m}^2$ area, consistent with the experimental data reported by Chan and Odde [158]. Unlike the cases described above, we now apply the total force over a longer time period (100 s) to determine the bond lifetime and the conditions of unbinding [171]. It is assumed that the cell is initially barely attached to the substrate, with $\beta = 0.01$, and is in a steady-state regime. The model predictions are presented in Figure 2.10, which shows the influence of substrate stiffness on adhesion lifetime.

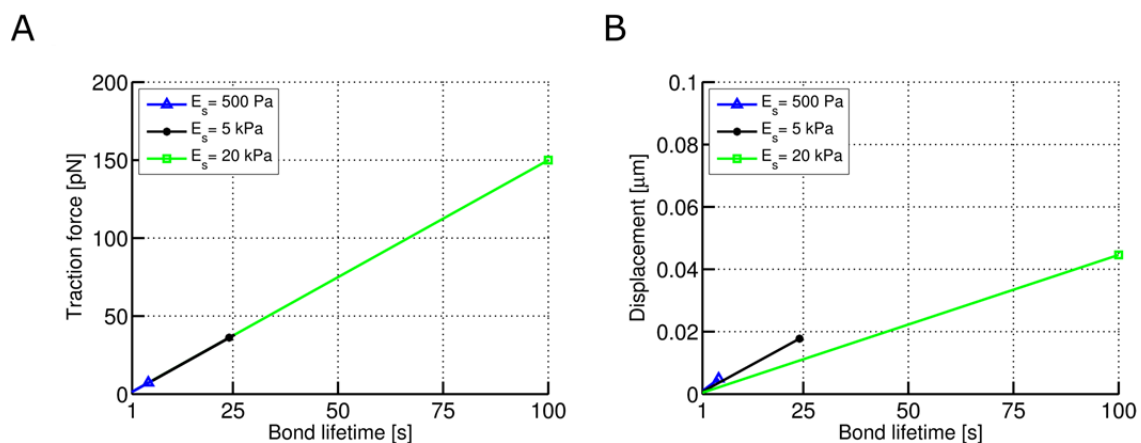


Figure 2.10: Influence of substrate stiffness on the lifetime of FAs.

A) Traction forces and B) displacements generated for each substrate stiffness case.

The simulation results shown in Figure 2.10 are consistent with results obtained in previous experimental studies [171, 172]. A larger substrate stiffness results in a longer bond lifetime and substrate displacement in the shear direction. This relationship arises from a force-sensing mechanism and is consistent with the results presented above because, over a certain range, larger substrate stiffness improves force transmission to the ECM.

2.3.2.3. Influence of cell force rate on adhesion rupture

The total force transmitted by the cell to the substrate is a time-dependent phenomenon that arises from the relationship between actomyosin contractility and the dynamics of stress fibers. Several experimental [173] and computational [171, 174] studies have concluded that cell contraction velocity is stiffness dependent. Based on these findings, the influence of cell force rate on FA rupture under constant substrate stiffness is simulated.

In this third series of simulations, a sensitivity analysis was performed to study the influence of cell contraction forces on the dynamics of cell-matrix interactions. To this end, three different cell loading rates were studied to compare with the bond dynamics presented by Evans et al. [172]. The main cell contractile loading rate of 100 pN/sg was obtained from the work of Crow et al. [171], who studied the contractile response of cells and observed the contraction velocity and force rate.

Similar to the previous simulations, a temporal linear relationship was applied for different values of shear forces onto the top surface elements of the model, distributed over a $1 \mu\text{m}^2$ area. As in the cases described above, the total force was applied over a longer time period of 100 s to determine the bond lifetime and the conditions upon unbinding [171]. Different cell force rates were studied. Again it is assumed an initial value for the DOA of $\beta = 0.01$. The model predictions for this case are presented in Figure 2.11.

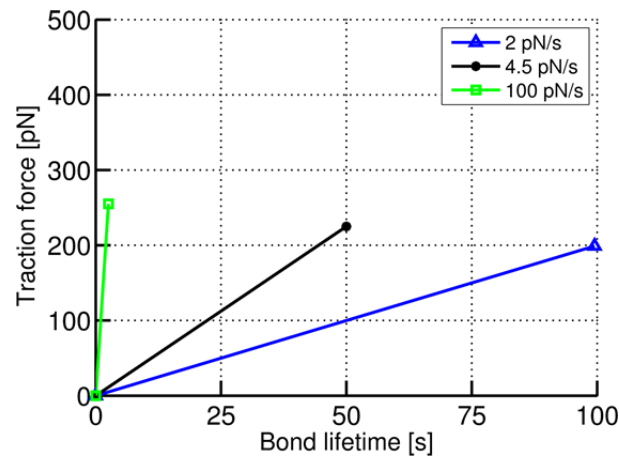


Figure 2.11: Influence of cell force rate on adhesion rupture.

As illustrated in Figure 2.11, increases in cell force rate correspond to decreases in the lifetime of cell-matrix adhesions. When we apply increasing load, the DOA grows exponentially with time; faster increases in force implies decreasing the time over which the cell remains attached to the ECM. Lower adhesion values along the interface result in smaller numbers of ligands between the cell surface and ECM. Consequently, the resulting traction forces are lower, producing slower cell contraction velocities.

Therefore, a larger cell force rate corresponds to a higher DOA and lower bond survival time. These results are consistent with experimental values of bond dynamics obtained by Evans and Calderwood [172], who reported a similar relationship.

2.3.2.4. Influence of traction forces on the cell-matrix adhesion

Finally, a sensitivity analysis was performed to study the influence of traction forces generated by cell contractions on cell-matrix adhesions. To study the influence of traction forces on DOA evolution, simulations applying normal, shear and combined tractions were performed to reproduce the cell contractile loads/displacements generated by the myosin heads and to apply local forces/displacements uniformly distributed over the elements at the top of the model.

This approach is able to quantify the temporal evolution of the DOA at the interface region with traction magnitudes above 0.1 pN and below 1000 pN distributed over a $1 \mu\text{m}^2$ area for an interface stiffness of 10 kPa, consistent with the studies of

Olberding et al. [153] and based on previous work by Balaban, Aroush and Nicolas [32, 137, 175]. The substrate used in these simulations has an elastic modulus of 7 kPa and a Poisson's ratio of 0.34, consistent with the substrates used in previous studies [158, 159, 167]. In these simulations, it is assumed that the cell is initially not entirely separated from the substrate; the initial DOA is assigned a value of $\beta = 0.1$. As in the first case, the duration simulated is 1 second. To consider the same effect of the springs on all directions, these have been introduced in the simulations in which a normal and combined traction force has been applied.

The influence of the traction forces on the evolution of the DOA is presented in Figure 2.12, which shows the average⁵ of the DOA β values over the interface elements at the end of each load increment.

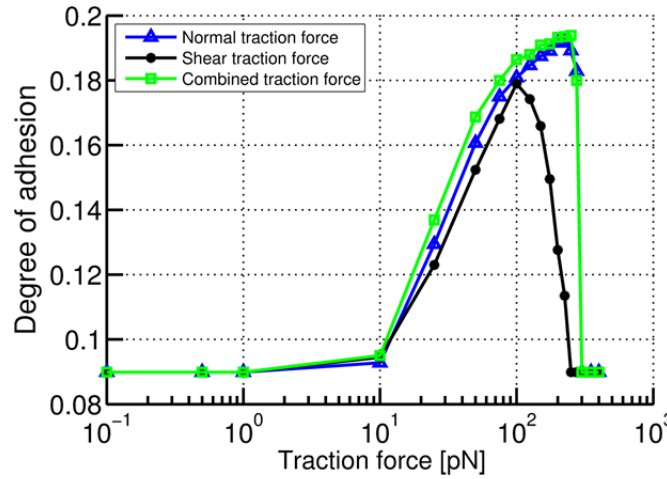


Figure 2.12: Influence of traction forces on cell-matrix adhesion. Evolution of the average DOA β in the focal adhesion domain as a function of the traction force and its direction: normal, shear and combined traction force.

As shown in Figure 2.12, four adhesion zones arise regardless of the direction of the applied force. The first, termed the neutral zone, is a region in which the DOA is insensitive to traction; that is, no adhesion develops for low loads (under 1 pN). The second is a nascent zone in which the cell is initially nearly separated from the substrate

⁵ The value of the DOA β of the interface for each load increment is calculated as the average of the DOA values for each interface element.

but begins to adhere for tractions larger than 1 pN. The third zone, corresponding to FA growth or evolution, exhibits a steep increase in DOA, reaching a point of maximum β whose exact value depends on the traction force direction. The fourth region is the failure zone, in which the adhesion stops growing and the transmitted load exceeds 100-500 pN, causing interface failure.

These results show that the evolution of the adhesion degree β is faster when we apply combined or normal traction forces on the cell compared with the same value of shear traction force. Thus, combined forces produce interfaces that can support larger loads. The different outcomes resulting from shear and normal loads are a result of the larger rotational moments that act on the interface, when shear loads are applied. The moments generated by normal traction and compressive loads at the periphery of the contact surface are only 20-50% of the values generated by shear loads. This force distribution has also been observed in studies by Legant and co-workers [167], who measured the 3-D traction forces exerted by fibroblasts on PEG hydrogels. They concluded that cells exert shear stresses that produce significant rotational moments about FAs when cells protrude or retract peripheral regions.

2.4. Numerical predictions: Global modeling of cell-matrix adhesions

In this section, it is explored the role of cell-matrix adhesions for a whole cell. In this manner, we aim to predict and understand how the geometry of the cell and its contractile properties can affect the dynamics of cell-matrix adhesions. For this purpose, a 3-D FE model of a single cell was created and different conditions to predict different adhesion scenarios were simulated.

2.4.1. Description of the FE model

To simulate the 3-D cell and substrate deformations, as well as the DOA evolution between the cell boundary and substrate surface, a 3-D FE model of a single cell was created that could represent a keratocyte, fibroblast or smooth muscle cell in a migration configuration. The cell shape in the model is inspired by the work of Zhong

and Ji [140]. The mean cell radius is $R = 30 \mu\text{m}$ and the maximum height is $13 \mu\text{m}$. The 3-D FE model used for the simulations is shown in Figure 2.13B and consists of 77481 cell elements, 2572 interface cohesive elements, 5144 substrate elements and 1258 elements for the cell nucleus. These different components were modeled with wedge and hexahedral linear elements, except for the interface, which was modeled with 6-node 3-D cohesive interface elements (triangular prisms).

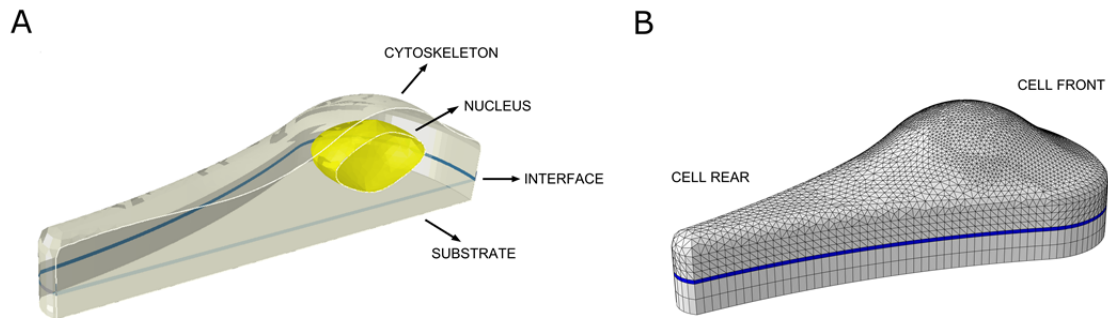


Figure 2.13: Schematic of the FEM used for simulating the global cell-matrix adhesion.

A) Schematic of a migrating cell in a stable position interacting with the substrate through interface elements. B) Rendering of the 3-D FEM used for the simulations.

The mechanical properties that define the constitutive parts of the model (see Figure 2.13A) are listed in Table 2.2, and the interface details are the same as those used in previous simulations (see Table 2.1 in Section 2.3.1).

Parameter	Description	Value	Remarks
E_s	Young's modulus of the substrate	7 kPa	§ [167]
E_c	Young's modulus of the cell body	1 kPa	§ [176, 177]
E_n	Young's modulus of the nucleus	5 kPa	* as $5 \cdot E_c$
ν_1	Poisson's ratio of the substrate	0.34	§ [167]
ν_2	Poisson's ratio of the cell and the nucleus	0.49	§ [177]

Table 2.2: Major parameters used in the 3-D model simulations.

* Estimated / Adjusted parameters

§ Parameters derived from the referenced manuscript

2.4.2. Influence of cell deformation on cell-matrix adhesion

As a first approach, a uniform contractile deformation is applied to the cell cytoskeleton to estimate or predict the spatial distribution of adhesion at the cell-matrix interface. This contraction value is estimated from experiments by Crow and Webster on individual cells [171]. In their assays, the steady-state contraction exerted by a cell embedded in an ECM with stiffness between 10 and 100 nN/ μm is on the order of 0.2 μm over a time period of 20 s (equivalent to cells contracting against an ECM with a Young's modulus between 1 and 10 kPa, respectively). Based on this cell contraction value and considering the fact that the cell height is 9.7 μm , we apply a contractile volumetric strain rate of 0.01s^{-1} . All simulations assume an initial DOA of 0.01, which means that the cell is initially nearly entirely separated from the substrate. The duration of the simulation is 10 s.

The computational model described above predicts cell adhesion regions as a result of DOA evolution in the elements comprising the bond region. Quantitative maps of individual cell behavior are presented in the following figures. Figure 2.14 shows model predictions of DOA evolution as well as the displacements generated in the horizontal direction at the interface region over time.

The maximum values of the DOA β (Figure 2.14A) as well as the maximum displacements in the horizontal direction (Figure 2.14B) occur at the cell front and rear regions and correspond to the maximum stress values generated in the cell. The maximum displacements and stresses generated at the bonded region are left-right symmetric around the center of the cell, as can be observed in Figure 2.14B. Furthermore, the deformation induced by cell contraction also causes a decrease on cell height.

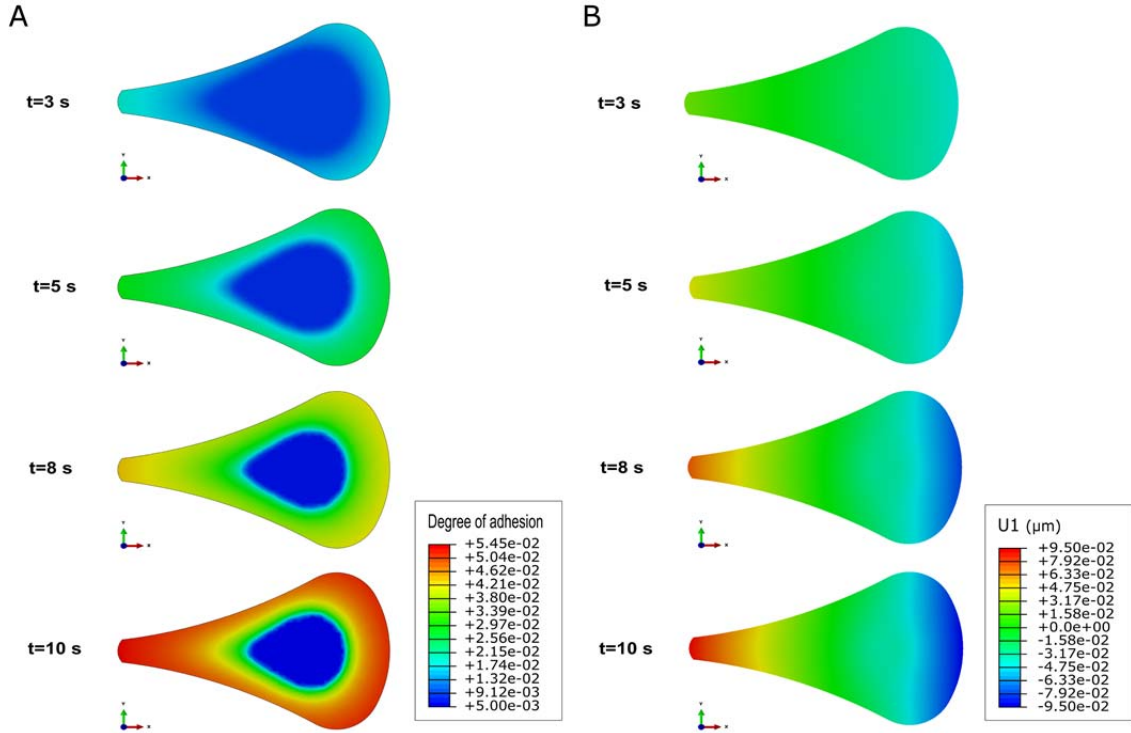


Figure 2.14: Influence of cell deformation on cell-matrix adhesion.

FE rendering of A) the evolution of the DOA β and B) the displacements generated in the horizontal direction, at the interface region over time for a cell contractile strain rate of $0.01s^{-1}$.

Nevertheless, Figure 2.14 only represents the case in which nascent FAs start to form at the front edge of the migration direction of the cell, in a region called lamellipodium. These nascent adhesions either disassemble or elongate and grow in the cell's lamella, in a process known as adhesion maturation [127]. To reproduce the mature FAs formation process, it was necessary to increase the cell deformation value by applying a contractile volumetric strain rate of $0.05s^{-1}$ and keeping all other parameters constant. Figure 2.15 shows model predictions of DOA evolution as well as the displacements generated in the horizontal direction at the interface region over time.

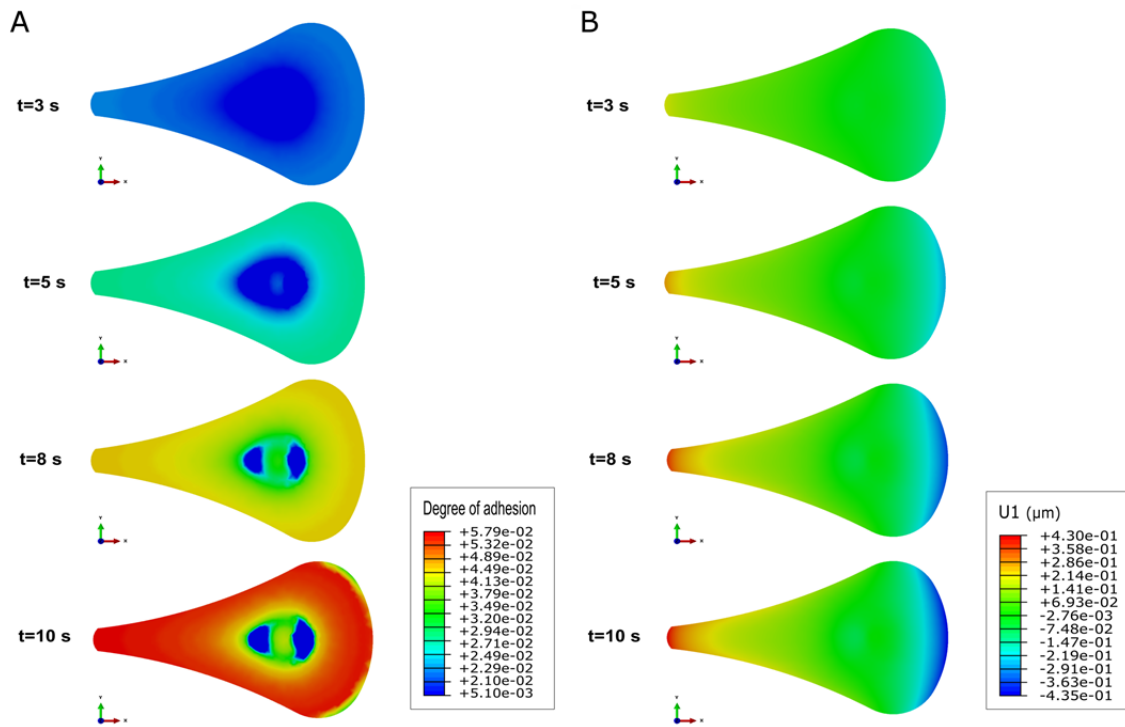


Figure 2.15: Influence of cell deformation rate on cell-matrix adhesion. FE rendering of A) the evolution of the DOA β and B) displacements generated in the horizontal direction, at the interface region over time for a cell contractile strain rate of 0.05s^{-1} .

Now, we can observe how the maximum displacements in the horizontal direction (Figure 2.15B) occur at the cell front and rear regions, which is not the case for the maximum values of the DOA β (Figure 2.15A). The maximum displacements generated at the interface region continue to be left-right symmetric around the center of the cell, as can be observed in Figure 2.15B. However, the maximum values of the DOA β (Figure 2.15A) begin to move towards the cell center as a consequence that some of the interface elements situated at the cell front region begin to fail.

As described above, these parameters are related to the nature of the traction forces between the cell and the substrate. The regions of maximum shear and normal tractions are at the cell periphery (Figure 2.16) as was also observed in experiments performed by Legant et al. [167] as well as on the numerical predictions obtained by

Ronan et al. [161]. Thus, the cell shape controls the traction force distribution in the cell and therefore it is able to regulate the driving force of cell migration.

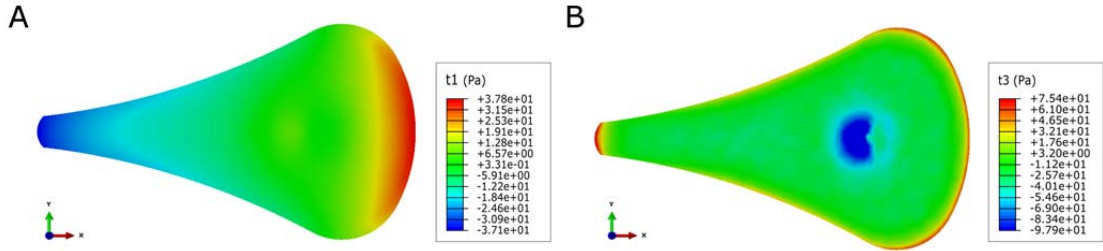


Figure 2.16: Interface stresses as a result of cell deformation.

FE rendering of the stresses in A) shear B) and normal direction, at the interface region at the end of the simulation for a cell contractile strain rate of $0.05s^{-1}$.

Therefore, with this approach, we can make qualitative predictions of individual cell adhesion processes for each time step as a function of the cell DOA evolution at the bond region that relates substrate displacements to surface tractions. One prediction is that higher adhesion forces correspond to a higher probability of FA growth because the stable-FA region is attained, resulting in cell spreading. But at the same time, when large forces are generated at the interface region, FAs are more unstable and more susceptible to detach at the lamellipodium of the cell, as was also observed in experiments performed by Zhong and Ji [140].

2.4.3. Influence of substrate deformation on cell-matrix adhesion

As a second approach, to study the influence of substrate deformation on the spatial distribution of the DOA a uniaxial force was applied aligned with cell's front-rear polarity, increasing linearly with time to 2700 pN, in the horizontal direction and at both ends of the substrate. As in the previous case, the simulations assume an initial DOA of 0.01, which means that initially, the cell is separated from the substrate. The simulated duration is 10 s. Figure 2.17 shows the resulting DOA data across an individual cell.

Figure 2.17 shows the maximum values of the DOA at the cell-matrix interface. In contrast to the previous case, the maximum values are concentrated at the cell front

and rear due to the maximum tractions generated in these regions by the substrate displacement.

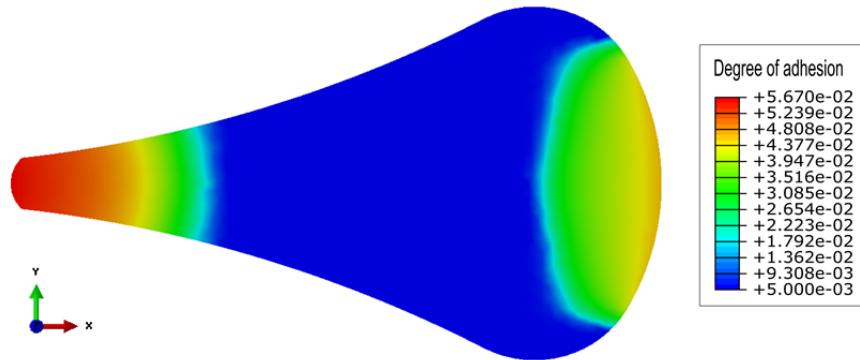


Figure 2.17: Influence of substrate deformation on cell-matrix adhesion. Spatial distribution of the DOA β at the cell-matrix interface region.

This finding reinforces the assumption that both internal properties of the cell and the external environment are affected by the evolution of cell-matrix adhesions. At the front and rear of the cell, shear and compression tractions are generated that promote ligand adhesion and activate the binding process, thereby increasing the DOA β between the cell and substrate (see Figure 2.17). Similar behavior was observed by Zhong and Ji [140].

2.5. Discussion

In this chapter, it is presented a novel model based on cohesive theories for simulating the adaptive and dynamic behavior of cell-matrix adhesions. It is demonstrated how the application of cohesive laws for modeling cell-matrix interactions can be a useful tool to simulate this complex behavior. This model is able to describe the dynamical and adaptive behavior of cell-matrix adhesions in response to transmitted mechanical stresses. This adaptive behavior corresponds with the increase or reduction of the degree of adhesion between the cell and ECM, as well as with the spatial growth or shrinking of cytoskeletal structures that regulate the size, shape, and location of FAs.

Therefore, many models have focused on the first aspect of this adaptive response, aiming to reproduce the recruitment or disengagement of FA components in response to different microenvironmental conditions, including ECM stiffness [159]. The

majority of existing models are based on discrete approaches [43, 158-160], in which sets of proteins are simulated as individual clutch components to predict the emergent behavior of these agent-based models. These models are useful in understanding the dynamics of cell-matrix adhesions at a local level.

In some cases, these discrete approaches have been extended to predict the growth or resorption of FAs under different conditions [43]. In all these cases, however, only one axis has been considered when simulating the dynamics of cell-matrix adhesions in a filopodium. The main advantage of using one-dimensional (1-D) models is their simplicity, allowing one to focus on understanding the adhesion phenomena, including two primary dynamic and adaptive properties of FAs: the increase/decrease of adhesion and the growth/reduction of size. Given the versatility of these 1-D configurations, we use this approach as a benchmark to evaluate the predictive capacity of our model. In fact, this continuum model is able to obtain predictions similar to the experiments and numerical results obtained by Chan and Odde [158] and Elosegui-Artola et al. [159].

To that end, single-filopodium behavior has been simulated on a continuous elastic substrate considering integrin reinforcement and tension-dependent strengthening of the adhesion through the evolution of the DOA state variable. The results reveal the existence of a mechanosensitive mechanism regulated by substrate deformation.

Nevertheless, these discrete approaches present some limitations; one is the high computational cost of their application to study whole-cell domains in three dimensions. Therefore, a simple alternative is the use of a continuum approach, as proposed here. In this work, different characteristics of cell-matrix adhesion growth are analyzed depending on the origin of the forces, which are classified into internal (actomyosin-generated) forces or external (exerted by or through the surrounding matrix) forces. In the case of forces generated by actomyosin contraction, adhesions begin to grow at the cell periphery and move inward relative to the location of the nucleus. This growth correlates with the origin of the forces produced in the body of the cell. However, for the case of external forces, adhesion onset also occurs at the cell boundary but not

along the entire external boundary. Adhesion starts at the boundary location closer to the direction of the forces, growing inward in these specific directions.

In addition, different conditions have been studied to provide better understanding of the dynamics and adaptive response of this model. To this end, the effect of the direction and rate of application of the traction forces generated by cells through cell-matrix adhesions was investigated. Cells adhere better on intermediate-rigidity substrates and generate stronger traction forces, in agreement with the results of Lo et al. [8]. Moreover, the loading direction influences the mechanical properties of the bond as a result of dynamic rotational moments exerted by cells, an effect that has been previously observed in the experiments of Legant et al. [167].

Finally, the model illustrated that the behavior of cell-matrix adhesions is strongly dependent on the rate of force application and duration of loading. That is, there is a biphasic behavior of the stability of FAs with respect to the magnitude of applied force. A relatively low force allows the growth and maturation of the FAs that stabilize the cell adhesion, while an excessively large force causes the disruption of cell adhesion. These predictions are consistent with the experimental results of bond dynamics obtained in the work of Evans et al. [172].

Therefore, a novel cohesive interface model capable of simulating dynamical and adaptive force-dependent adhesion phenomena that regulate the cell-ECM connection is presented. Actually, this model allows the study of adhesion dynamics for static cells. In addition, this model could be extended by means of using slide contact between both surfaces in order to simulate cell migration.

Moreover, cell-specific FE models based on confocal microscopy images [177] are an important component of the development of *in silico* cellular mechanics experiments. Previous models have generally underestimated the dynamic and adaptive properties of cell-matrix adhesions, instead considering a completely bonded adhesion between the cell and matrix. The incorporation of a cell-matrix adhesive constitutive law, such as the one presented here, can be easily implemented in this type of cell-specific models.

Chapter 3

IN VITRO MODEL FOR STUDYING CELL-MATRIX INTERACTIONS

Advances in microfabrication have allowed the development and popularization of microfluidic devices, which are powerful tools to recreate 3-D physiologically relevant cellular microenvironments. These microenvironments are usually generated by including biomimetic hydrogels and generating controlled chemical gradients. This chapter introduces an *in vitro* model based on microfluidic technology, to study the cell-matrix interactions inside a 3-D ECM, such as fibrin or collagen type-I hydrogels. First, the chemical gradient formation process within these microfluidic devices is explored by using a FEM. Secondly, the possible chemotactical and haptotactical cues generated inside these microdevices are evaluated. Finally, an intensive multiparametric analysis is carried out in four different microfluidic device geometries, to study the dependence of the geometrical parameters onto the gradient formation processes. In addition, a web-based application for automated quantification of chemical gradients induced in microfluidic devices is presented⁶.

⁶ The main insights and results of this chapter have been published in: M. Córdor, T. Rüberg, C. Borau, J. Piles and J.M. García-Aznar. *A web-based application for automated quantification of chemical gradients induced in microfluidic devices*. Computers in Biology and Medicine, 2018 [178]. O. Moreno-Arotzena, G. Mendoza, M. Córdor, T. Rüberg, and J.M. García-Aznar. *Inducing chemotactic and haptotactic cues in microfluidic devices for three-dimensional in vitro assays*. Biomicrofluidics, 2014 8(6) [179].

3.1. Introduction

The study of cell motility plays a key role in the understanding of numerous biological processes such as embryogenesis, immune defense, wound healing or the development of certain diseases such as cancer invasion or metastasis [180-183]. Several growth factors have been identified to stimulate cell motility, and the signaling mechanisms that mediate this induced cell movement have been thoroughly studied [184-186]. In particular, individual directional cell migration (which encompasses chemosensing, polarization and locomotion) is distinguished as a function of the signaling pathway [187]. Broadly speaking, depending on the chemical stimulus that originates the movement, two migration types are defined: chemotaxis, if cells migrate towards a soluble chemoattractant; or haptotaxis, if a growth factor (GF) bound to the ECM influences cell motility [188, 189]. Hence, the study of a GF diffusion behavior within the ECM, as well as the associated adhesion and degradation processes, is critical for the understanding of the chemotactic and haptotactic gradients generated by these biomolecules, which directly affect cellular behavior.

In recent years, numerous research studies have focused on recreating *in vitro* 3-D cell cultures capable to replicate many aspects of *in vivo* cell microenvironments [190]. The main advantages that *in vitro* assays present compared to *in vivo* studies are their relatively easy handling and high reproducibility. Furthermore, recent advances in microfluidic technologies have enabled the development of new generation microfluidic devices, allowing the production of physiologically relevant *in vitro* cellular microenvironments, by including biomimetic hydrogels and the generation of controlled chemical gradients [191, 192]. These models furthermore allow high quality visualization and quantification of cell responses *in vitro*, and in particular the study of GF behavior within 3-D matrices, as well as the associated adhesion and degradation processes [179, 193, 194].

Quantification of growth factor signaling in 3-D matrices has greatly increased the understanding of directional cell migration processes, addressing several issues: the degree to which these factors can concentrate within the 3-D matrices, such as collagen or fibrin hydrogels and, consequently, act as signaling molecules driving cell motility

[179]. Nevertheless, there are still several unresolved issues, such as the study of the dependence of the geometrical/design parameters of these devices on the gradient formation processes or the development of a powerful computational tool that allow an automatic quantification of growth factor signaling within a biopolymer network.

Thus, in this chapter we present a finite element model based on a reaction-diffusion transport model accompanied by a web-based application, to automatically calculate the distribution of different growth factors, across hydrogel-based matrices (specifically collagen type I and fibrin). This application yields an accurate prediction, based on previous experimental results, where diffusion and binding phenomena can be estimated within the microdevice. To that end, quantitative Enzyme-Linked Immuno Sorbent Assays (ELISA) for growth factor concentrations measurement were performed and the behavior of the dextran diffusion gradient was studied, validating therefore the proposed numerical model [179].

Among many others GFs, platelet derived growth factor-BB (PDGF-BB) and transforming growth factor- β_1 (TGF- β_1) have been selected to perform the sensibility/parametrical analysis across collagen and fibrin hydrogels. These GFs have received increasing attention in the last years due to their diverse biological effects. For instance, PDGF-BB is a pro-migratory factor that plays a key role in the early stage of wound healing, whereas TGF- β_1 stimulates fibroblasts differentiation into contractile myofibroblasts. Furthermore, the binding capability of these GFs to different ECM components exerting their biological activity has been reported [195-197]. Due to the considerable similarity encountered between synthetic hydrogels and the native extracellular matrix, synthetic hydrogels can serve as model systems for studying the transport of a soluble molecule and the formation of chemical gradients in biological systems. The hydrated polymer chains of synthetic hydrogels promote a slow movement of the solute as well as the macromolecules existing within the ECM, thus enhancing gradient formation [198, 199]. The diffusion of both GFs was studied on two different hydrogel-based matrices, namely collagen type-I and fibrin. Collagen I is one of the major components of the connective tissue, up to 30% of total human protein; and fibrin is an essential component of healing and angiogenic processes [200-202].

Moreover, the parameterization of four different base designs of microfluidic devices to analyze the diffusive behavior of a growth factor within a fibrillar network, thereby facilitating the main parameters that characterize the gradient formation process inside these microdevices. The finite element analysis of the numerical model proposed has been performed with an unstructured finite element mesh, based on linear triangle elements and an Euler backward time integration scheme [203]. The results demonstrate that growth factor diffusion within 3-D matrices clearly depends not only on the physics of diffusion, but also on the geometrical parameters that characterizes these complex devices.

In addition, a web-based application was developed to facilitate to any user an automatic estimation of the growth factor diffusion within 3-D matrices. This application allows the user to define the geometrical parameters that characterize each chip design (hydrogel height and width or number of posts among others); as well as the diffusion-related parameters: the type of growth factor (PDGF-BB or TGF- β_1), the initial GF concentration, the matrix (collagen or fibrin) and the diffusion time to simulate. This platform therefore facilitates any user the possibility to customize its own microfluidic device and automatically simulate the chemical conditions that would regulate *in vitro* 3D cell responses.

3.2. Microfluidic devices design and fabrication

Microfluidic devices fabrication is based on combination of soft lithography and replica molding techniques [204]. First, a SU8 mold is obtained by photolithography which is later reused for replicating molds multiple times of PDMS. Photolithography has a number of significant advantages, including the flexibility in designing geometries, so modifications of motives are easily overtaken.

With regard to the fabrication process, these microdevices are made of polydimethylsiloxane (PDMS-Dow, Dow Chemical) at a ratio of 10:1 polymer to crosslinker, using SU8-silicon wafers (Stanford University, CA) obtained by soft lithography (see Figure 3.1A). After fabrication, PDMS microdevices are autoclaved and dried at 80°C overnight. Finally, Surface plasma treatment was used to bond the PDMS

device with the glass-bottom of 35 mm petri dishes (Ibidi) followed by the addition of poly-D-lysine solution (PDL, Sigma-Aldrich) to enhance the surface-matrix attachment.

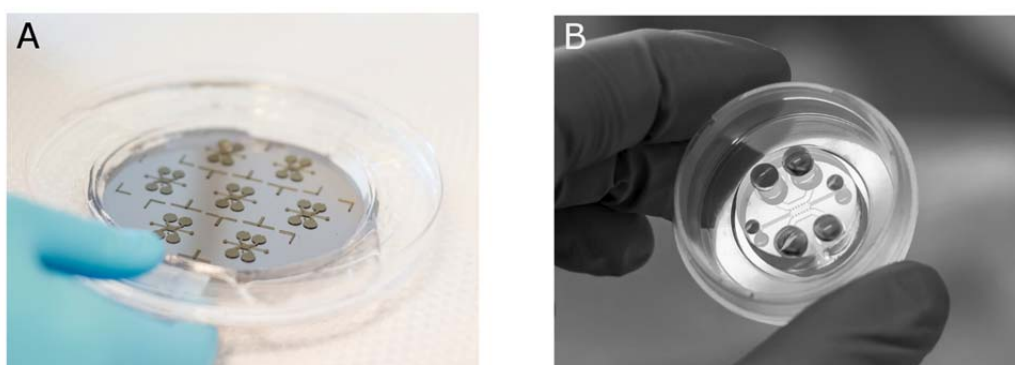


Figure 3.1: Fabrication of microfluidic-based devices.

A) SU8-silicon wafer were the liquid PDMS is spilled. B) Single microfluidic device ready for experiments, after PDMS curing, extracted from the mold and bonded to a glass coverslip (Ibidi Petri dish) [205].

The geometry of the microfluidic devices used for the experiments is shown in Figure 3.1B. It contained a central channel, in which the hydrogel with cells is located, and two media channels (condition and control channels) at both sides of the central channel in direct connection with the cell-gel solution, to ensure diffusion and hydration of the collagen gel and cells [179]. Moreover, the central channel is separated from the lateral ones by a set of micropillars which are responsible to retain the cell-hydrogel solution in the central area of the device. The geometries are explained with more detail in the following sections.

3.3. Study of GF transport within synthetic hydrogels inside microfluidic devices

In this section the GF transport within synthetic hydrogels is investigated by using microfluidic devices. These microfluid devices are currently used in real experimental assays for studying different biological processes, such as angiogenesis, directional cell migration, wound healing or even for drug screening experiments. For that reason, it is so important to have a better knowledge of the transport process of different biomolecules inside them.

3.3.1. Numerical model of GF transport within synthetic hydrogels

During the transport of a biomolecule within a synthetic hydrogel, these can interact in distinct ways with the fibrillar network: as a purely diffusive factor in the soluble fluid or bound to the matrix proteins. Moreover, the degradation of the factor takes place at the same time as a result of their interaction with other biomolecules [196, 206, 207].

To determine the concentration gradients established inside a synthetic hydrogel, we use a reaction-diffusion model where the rate of change of concentration depends on a diffusive term (which explains the movement of the factor) and a reaction term that incorporates the degradation and the binding of the factor to the fibrillar network:

$$\frac{\partial C(x,t)}{\partial t} = D_i \nabla^2 C(x,t) + R_i \quad i=1, 2 \quad (3.1)$$

where index i refers to the microfluidic domain where equation 3.1 is evaluated, C is the concentration of the factor, D_i is the effective diffusion coefficient and R_i the reactive term. We consider that that binding phenomena can only take place in the central domain of the device where the hydrogel is situated (see Figure 3.2). Therefore, the reactive term can be defined as a function of the microfluidic device domain:

$$R_i = \begin{cases} -k_d C(x,t) & \text{if } i=1 \text{ (lateral channel)} \\ -k_b C(x,t) & \text{if } i=2 \text{ (central channel)} \end{cases} \quad (3.2)$$

where k_d and k_b are the degradation and binding rates respectively. Both coefficients were numerically estimated for each particular case of study, to reduce the average difference on concentrations quantifications obtained experimentally [179].

The transport of a soluble biomolecule within a synthetic hydrogel depends not only on the solute properties but also onto the fibrillar network ones. Then, standard and effective diffusion coefficients were computed by means of Stokes-Einstein equation and Ogston-Kim formulation respectively [208-210]:

$$D_\infty = \frac{K_B T}{6\pi\eta r} \quad (3.3)$$

$$D_l = D_\infty e^{-\left[\sqrt{v_v} \left(1 + \frac{r}{r_f}\right)\right]} \quad (3.4)$$

where K_B is the Boltzmann constant, T the absolute temperature, η the viscosity of the fluid, v_v the void ratio of the matrix, r the radius of the biomolecule to diffuse and r_f the fiber radius of the fibrillar network.

For further information about the experimental quantification of GF concentration and degradation as well as diffusion coefficients estimation and matrix measurement properties, see our previous works [66, 179].

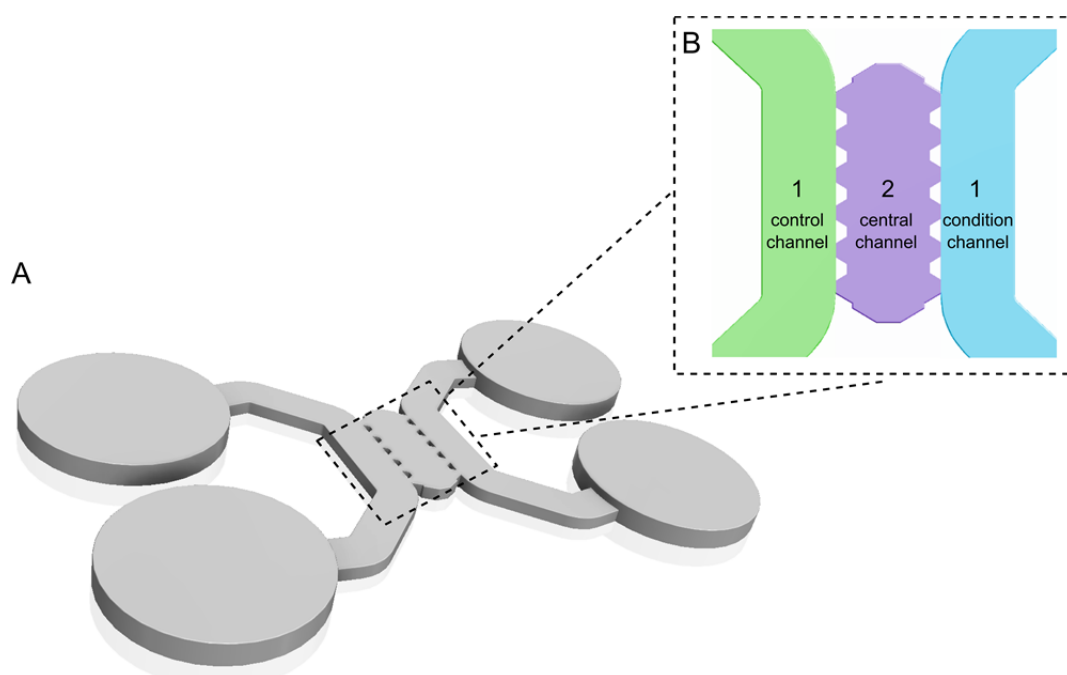


Figure 3.2: Geometry of the microfluidic-based device.

A) Three-dimensional view and B) detail of the central area of the device, specifying the different domains where the Eq. 3.1 is evaluated. Domain 1 corresponds with the control and condition channels (used to introduce a GF and induce a chemical gradient) and domain 2 corresponds with the central channel of the device where the hydrogel and cells are situated during the experimental setup.

3.3.2. Microfluidic device geometry parameterization

An automatic generation of microfluidic device geometries was implemented to facilitate an automatic quantification of a diffusion case inside any microfluidic device geometry. To study how the different geometrical parameters that characterize microfluidic devices affect diffusion gradients on *in vitro* 3-D cell cultures, four base

geometries of microfluidic devices were parameterized. These models are currently used in real experimental assays for studying different biological processes, such as angiogenesis [211], directional cell migration [179], wound healing [212], or even for drug screening experiments. In the following text, these 4 devices are referred as chip-1, chip-2, chip-3 and chip-4 attending to the nomenclature showed in Figure 3.3B-E.

These microdevices are basically composed by a central channel, in which the hydrogel or the matrix is located; and two lateral channels (condition and control channels) on both sides of the central channel and in direct connection with the hydrogel, ensuring therefore the diffusion and hydration of the hydrogel and the cells during the experiments development (see Figure 3.2). Due to their geometrical features, the most versatile device is possibly chip-1, which is used for studying 3-D directional cell migration processes. Also, chip-4 is worth highlighting because of its special design, composed by 2 different central compartments where two different hydrogels can be simultaneously introduced, allowing therefore studying wound healing processes and the interface region between two different scaffolds or hydrogels (e.g. collagen and fibrin hydrogels) [212].

The generation of concentration gradients inside a microfluidic device is highly dependent on the geometry of the gradient formation region, which is basically defined by the central area of the device where the hydrogel is situated, and conditioned by both lateral channels (control and condition channel). The diffusion gradient generated in the central channel of the device depends on the volume enclosed within it, being defined mainly by the hydrogel scaffold height and width (H_{gel} and W_{gel}). In addition to these two parameters, this region is also determined by the area enclosed by the posts as well as the post shape, mainly affecting the flow regime generated and to the flow speed. For studying the post role, two different column/post geometries have been implemented: trapezoidal (chip-1 and chip-2) and rectangular (chip-3 and chip-4). Moreover, for a given hydrogel height, the diffusion gradient will be conditioned by the height and the number of posts situated inside the device (H_p and N_p respectively) (Figure 3.3A).

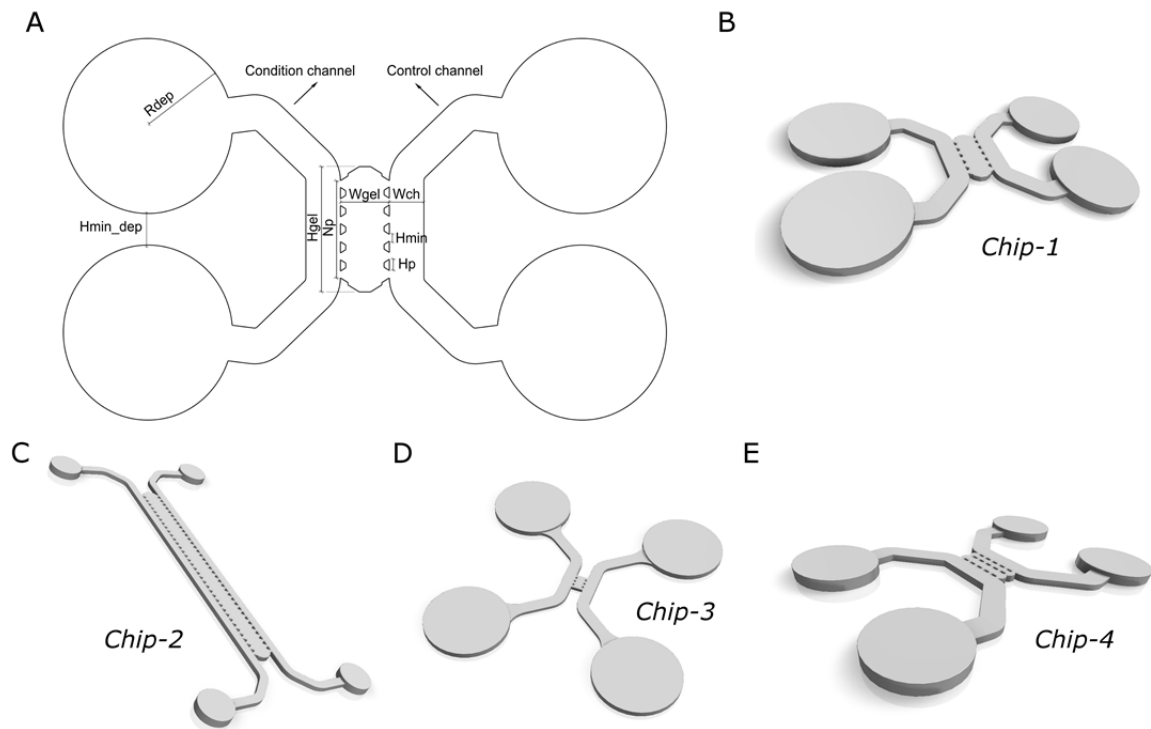


Figure 3.3: Parameterization of a microfluidic-based device.

A) Parameters defining automatic microfluidic device geometry. R_{dep} stands for the deposit radius (unnecessary for the simulations), H_{gel} and W_{gel} are the hydrogel height and width respectively, W_{ch} is the lateral channels weight, H_p and N_p are the post height and number of posts, and H_{min} and H_{min_dep} are the minimal height between posts and deposits respectively. The four device geometries used for the parametric study: B) Chip-1 which currently is used for studying directional cell migration, C) chip-2 which is employed for studying angiogenesis, D) chip-3 which is currently used for following-up and monitoring of drugs and E) chip-4 which is the double channel device and is used for studying wound healing processes. The parameter values that define the four chip geometries are all reported in Table 3.1.

Moreover, for *in vitro* cell migration experiments, the spatial distribution of the posts will limit the movement of cells between channels, being limited therefore by the available inter-space between the posts. If the separation between posts is smaller than the average cell size, cells will not be able to pass through the posts during experiments. The average size of eukaryotic cells usually ranges from 10-100 μm [213]. Thus, the minimum distance between two posts (H_{min}) was fixed equal to 50 μm and therefore cannot be modified by the user (see Figure 3.3A).

Parameter	Chip 1	Chip 2	Chip 3	Chip 4
H_{gel}	3.2	15.22	1.44	3
W_{gel}	1.3	1.3	1	1.5 (2x0.75)
W_{ch}	1	0.5	1	0.9
H_p	0.3	0.3	0.16	0.25
N_p	5	36	3	5

Table 3.1: Main geometrical parameters of microfluidic-devices.
All parameters are in mm.

With regard to the lateral channels, it is assumed that they have the same width (W_{ch}) and that there are no differences between control and condition channels radii, thus maintaining the symmetry of the microfluidic device. To avoid deposit overlapping during the automatic microfluidic device geometry generation, a minimum distance between deposits was established (H_{min_dep}). This distance is fixed, equal to 50 μm and not modifiable by the user (see Figure 3.3A).

Finally, to extend the two-dimensional geometry parameterization to a three-dimensional one, the depth of the hydrogel (D_{chip}) which is constant throughout the entire domain of the device, must be set for the simulations. For all devices the depth is fixed to 120 μm and not modifiable by the user.

Once all parameters are set, the microfluidic device geometry is generated with a custom python code. Through the parameterization of these microdevices, any device can be automatically generated based on six input parameters (H_{gel} , W_{gel} , W_{ch} , H_p , N_p and R_{dep}), without losing the model scale, allowing a semiautomatic generation of microfluidic devices, and therefore reducing design times and facilitating experimental validation processes as well as parameter selection.

3.3.3. 3-D Finite element model of a microfluidic device

The diffusion phenomena inside a microfluidic device is essentially planar, therefore we employed a 2-D finite element model based on an automatically generated mesh and an Euler backward time integration scheme. The finite element mesh is automatically generated with the mesh generator GMSH [214] and the calculation it is solved with a finite element method using the custom-made library *inSilico* [215].

The mesh was constructed using linear triangular elements with an automatic adaptive/flexible element size varying between 100 to 400 μm based on a Delaunay triangulation. The element size was inside the asymptotic region of convergence and represented a good trade-off between numerical accuracy and computational cost for all cases. Three different mesh domains were defined (Figure 3.4) (condition channel: red area, central domain: green area and control channel: blue area) to obtain a better adaptive element size on each domain and no distorted elements. Moreover, a locally mesh refinement was performed in the regions of interest, such as the central domain of the device or in the interface between the lateral channels and the central domain.

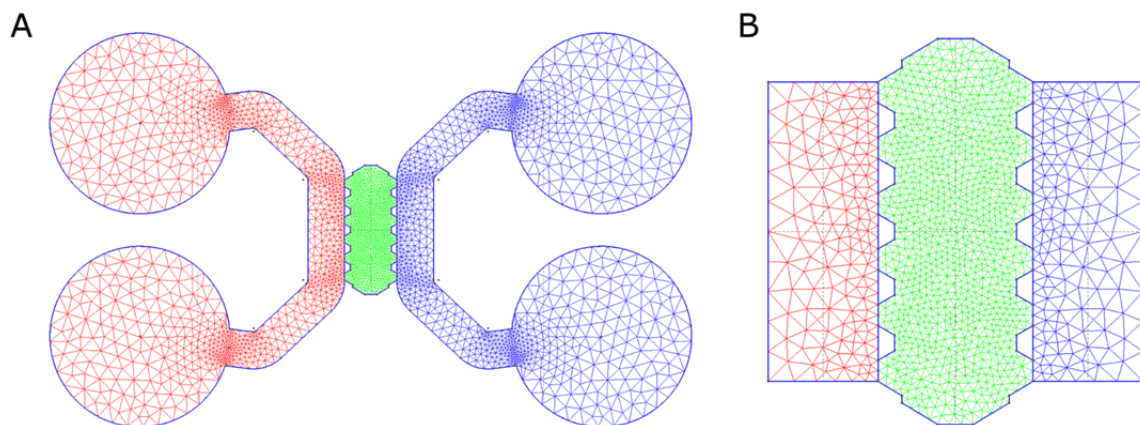


Figure 3.4: Finite element model of a microfluidic-based device.
A) Automatic FE mesh of chip-1 geometry and B) the simplified one.

To avoid unnecessary calculations and improve the time response to the user, the geometry was simplified by pruning the load channels. Doing this we are assuming that the chemical factor diffuses homogeneously throughout the condition channel of the device and the growth factor concentration at the initial time is constant in both lateral

channels. The simplified finite element model of chip-1 used for diffusion simulations is shown in Figure 3.4B and consists of a total of 1335 vertices and 2762 triangular elements. Thus, for the simplified model only 5 input parameters will be actually necessary to automatically reconstruct the device geometry: the hydrogel scaffold height and width (H_{gel} and W_{gel}), the lateral channels width (W_{ch}) and the post height and number of posts (H_p and N_p).

The simulation backend is based on a standard FEM formulation with Lagrange-type elements [216]. At the spatial boundaries homogeneous natural boundary conditions are used. As initial condition, a non-zero concentration was prescribed in the control channel, based on which the time-stepping started. For reasons of robustness, a simple Euler backward method is employed which is unconditionally stable [216]. Due to the small system size, Cholesky decomposition was used in order to solve the linear equations in each time step.

3.3.4. Web application for the numerical model proposed: Insilico-cell

A web-based application was developed for the numerical model proposed, allowing to any user the calculation of the concentration gradients established inside a microfluidic-based chip (see Figure 3.5). To do so, a PHP code was inserted into the website of the *Insilico-cell* project. This code reads the parameters from the user input and sends them to a private cluster which builds the geometry, performs the calculations and returns the computed results to the web portal screen in approximately 3 minutes. To avoid cluster overflow due to bot action, all users must create an account to be able to freely use the web application here presented.

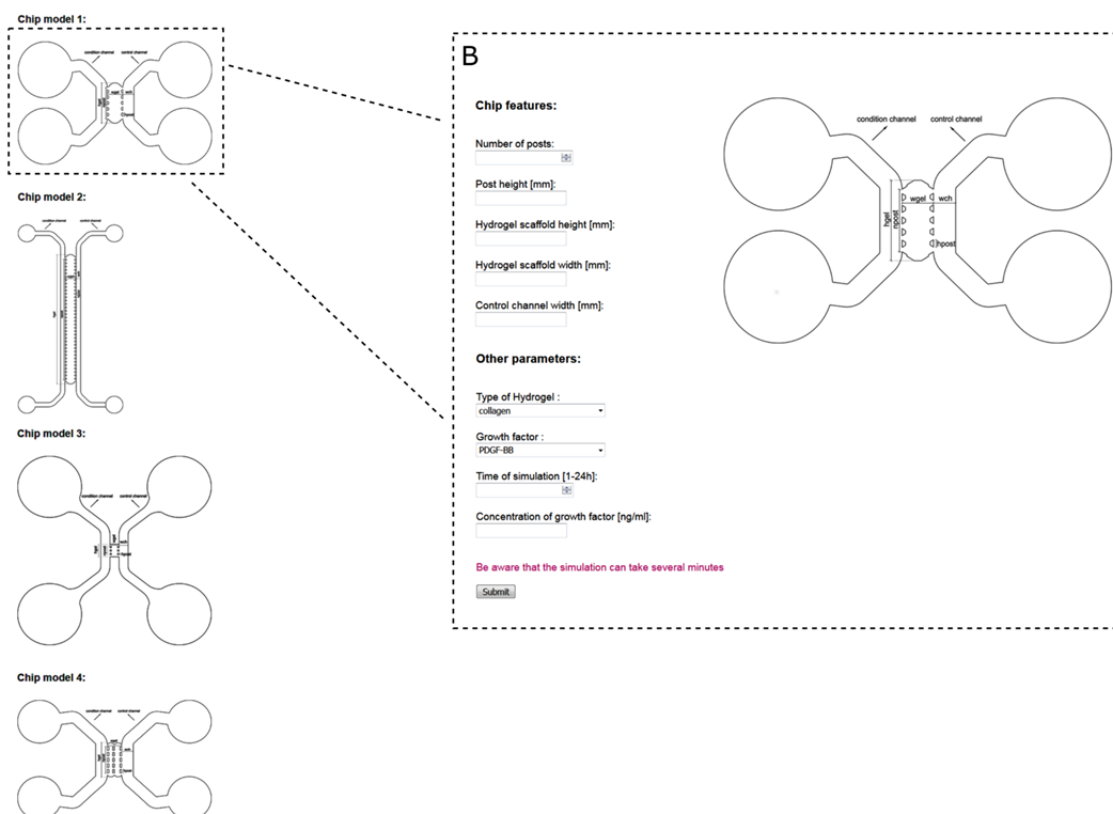
The computational requirements involved make a local calculation in the client infeasible. Even a server-side solution would put too much of a strain on server, possibly impacting the operation of the website itself, and hence causing a poor user experience. A cluster solution was thus developed where the website acts as a front-end that submits jobs to a remote computing resource using the HTCondor queueing management system [217].

The website will wait until the job has been processed, will then retrieve the results from the cluster, and will finally show them. This whole process is done in a way totally transparent to the user, which offers greater flexibility to upgrade the computing power according to the demand of the service. Furthermore, the computing resources used need not be exclusively dedicated to this task, since a job priority system allows to run jobs coming from the website (which are therefore much more sensitive to delays in their completion) before background ones.

A

Software

Please select one of the chip models below to perform the calculation:



The interface displays four chip models (Chip model 1, 2, 3, and 4) as clickable images. Chip model 1 is highlighted with a dashed box, and a dashed line connects it to a larger parameter input window labeled 'B'. This window contains the following sections:

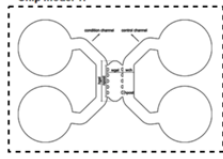
Chip features:

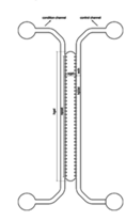
- Number of posts:
- Post height [mm]:
- Hydrogel scaffold height [mm]:
- Hydrogel scaffold width [mm]:
- Control channel width [mm]:

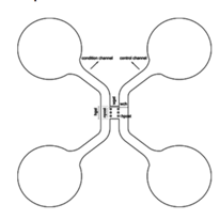
Other parameters:

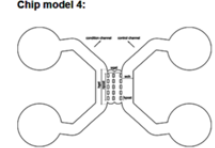
- Type of Hydrogel:
- Growth factor:
- Time of simulation [1-24h]:
- Concentration of growth factor [ng/ml]:

At the bottom of the input window, there is a warning: "Be aware that the simulation can take several minutes" and a "Submit" button.

Chip model 1: 

Chip model 2: 

Chip model 3: 

Chip model 4: 

B

Chip features:

Number of posts:

Post height [mm]:

Hydrogel scaffold height [mm]:

Hydrogel scaffold width [mm]:

Control channel width [mm]:

Other parameters:

Type of Hydrogel :

Growth factor :

Time of simulation [1-24h]:

Concentration of growth factor [ng/ml]:

Be aware that the simulation can take several minutes

Figure 3.5: Screenshot of the web-based application interface.

A) The four different models of microfluidic devices are presented as clickable images. B) Parameter input-window is opened after selecting any device (chip-1 on the image), where the user may select the input parameters that define the chip geometry and the calculation parameters.

The application allows users to simulate a diffusion case choosing among the 4 different base geometries previously presented (chip-1, chip-2, chip-3 and chip-4). Once the user has selected the device geometry, the corresponding parameters-input window is opened (see Figure 3.5B). Firstly, the user must set the 5 parameters defining the simplified device geometry: the hydrogel scaffold height and width (H_{gel} and W_{gel}), the lateral channels width (W_{ch}), the post height and the number of posts (H_p and N_p). Subsequently, the user must define the diffusion case defining: the growth factor (PDGF-BB or TGF- β_1), the initial growth factor concentration (any value in ng/ml), the hydrogel or scaffold (collagen or fibrin) and the diffusion time to simulate (up to 24 hours, see Figure 3.5B). These are all the possible combinations that can be currently simulated which correspond with the ones experimentally validated so far.

3.4. Results

In this section the chemical gradient formation process is explored by using the FEM introduced above. Firstly, the possible chemotactical and hapotactical cues generated inside these microdevices are evaluated for four different models of microfluidic devices. Secondly, an intensive multiparametric analysis is carried out in one microfluidic device, to study the dependence of the geometrical parameters onto the gradient formation process. Next, the effect of the combination of different hydrogels inside a microfluidic device is studied. Finally, a web-based application for automated quantification of chemical gradients induced in microfluidic devices and its usefulness is presented.

3.4.1. Numerical predictions of GF transport: 4 different geometries

To evaluate the predictive capacity of the theoretical model, the dextran diffusion gradient was simulated within chip-1. Moreover, four different cases were previously experimentally validated: 24 hours of diffusion of PDGF-BB and TGF- β_1 in collagen and fibrin. For all cases, the numerical simulations fairly accurately predicted the experimental concentrations obtained with the ELISA assays. For more information about the experimental quantification of GF concentration and degradation as well as the numerical model validation, see a previous published work [179].

To determine whether or not there are significant differences between diffusion gradients on different models of microfluidic devices, as a first approach, the same diffusion case was simulated for the four different base models of microfluidic devices presented before. To that end, the diffusion behavior of PDGF-BB growth factor on collagen gels was studied. The initial concentration of PDGF-BB applied was 50ng/ml in all cases and the total simulated time was 24 hours. The radius of this particle was estimated from Protein Data Bank to be $4.5 \cdot 10^{-9}\text{m}$, which according to equation 3 corresponds to a standard diffusion coefficient of $1.26 \cdot 10^{-11}\text{m}^2/\text{s}$, which in turn leads to an effective diffusion coefficient of PDGF-BB in collagen of $0.77 \cdot 10^{-11}\text{m}^2/\text{s}$. The collagen hydrogel characterization was previously performed with confocal reflection imaging and collagen fiber radius was estimated to be $79.51 \pm 33.16\text{nm}$ (mean \pm se) and the collagen void ratio to be $80.15 \pm 1.82\%$ (mean \pm se). The degradation and binding rates used in all simulations are $3 \cdot 10^{-6}\text{s}^{-1}$ and $1 \cdot 10^{-5}\text{s}^{-1}$ respectively, both experimentally adjusted [179]. In the case of chip-4, the double channel device, a double collagen type I hydrogel was simulated.

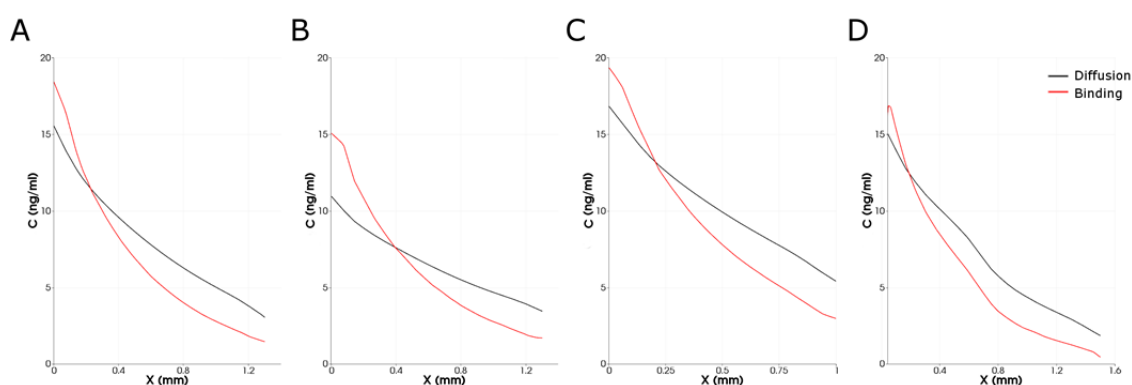


Figure 3.6: Numerical predictions of PDGF-BB diffusion within a collagen type I hydrogel for different microfluidic device geometries.

Diffusion and binding profiles obtained after 24 hours of diffusion of PDGF-BB in the central domain of: A) chip-1, B) chip-2, C) chip-3 and D) chip-4.

Figure 3.6 shows model predictions of diffusion and binding profiles generated in the hydrogel domain or in the central channel of the device, for the different models of microfluidic devices after 24 hours of diffusion of PDGF-BB. Model predictions show different diffusion and binding profiles on each device, for equal initial concentration of PDGF-BB. As expected, these data reveal that diffusion gradients are highly dependent

on the device geometric parameters and not only the diffusion-related ones. Thus, it becomes necessary to perform an intensive parametric analysis to establish which ones are particularly relevant.

3.4.2. Multiparametric analysis of gradient formation within a synthetic collagen-based hydrogel

The gradient formation region of these microdevices was initially designed to generate quasi-linear concentration profiles inside them. However, as stated before, geometrical parameters have a strong impact on the concentration profiles generated inside them. To define the main parameters that characterize the gradient formation processes within a synthetic hydrogel, a multiparametric analysis of the gradient formation region was performed.

To understand the dependence of geometric parameters of microfluidic devices onto the gradient formation processes, 6 different parameters were studied: the hydrogel scaffold height and width (H_{gel} and W_{gel}), the lateral channels width (W_{ch}), the post height (H_p), the number of posts (N_p) and the type or shape of posts (rectangular and trapezoidal). The simulated case was the diffusion of PDGF-BB growth factor within a collagen hydrogel and the total time simulated was 24 hours. The reference values for chip-1 device were: $H_{gel}=3.2$, $W_{gel}=1.3$, $W_{ch}=1$, $H_p=0.3$, $N_p=5$ and trapezoidal posts (all values in mm). Figure 3.7 shows the corresponding results of every case indicating the varied parameter. Degradation and binding rates are the same as previously, namely $3e^{-6}$ and $1e^{-5} s^{-1}$ respectively. The standard and effective diffusion coefficient were also maintained ($1.26 \cdot 10^{-11} m^2/s$ and $0.77 \cdot 10^{-11} m^2/s$ respectively).

Some parameters such as the hydrogel height and width (H_{gel} and W_{gel}), the lateral channels width (W_{ch}) or the posts height (H_p) presented strong effects on the diffusion and binding profiles generated in the central domain of the device (see Figure 3.7A-H), whereas the post shape repercussion was negligible. Differences on concentration for condition and control channels with respect to the reference case (chip-1 with the reference parameter values) were also quantified. Changes on hydrogel width generated differences of up to 21% on condition channel concentration and of about 24% on

control channel concentrations (Figure 3.7C-D respectively); On the other hand, changes on post height showed lower differences of 6% on condition channel concentration and of 13% on control channel concentrations (Figure 3.7G-H respectively).

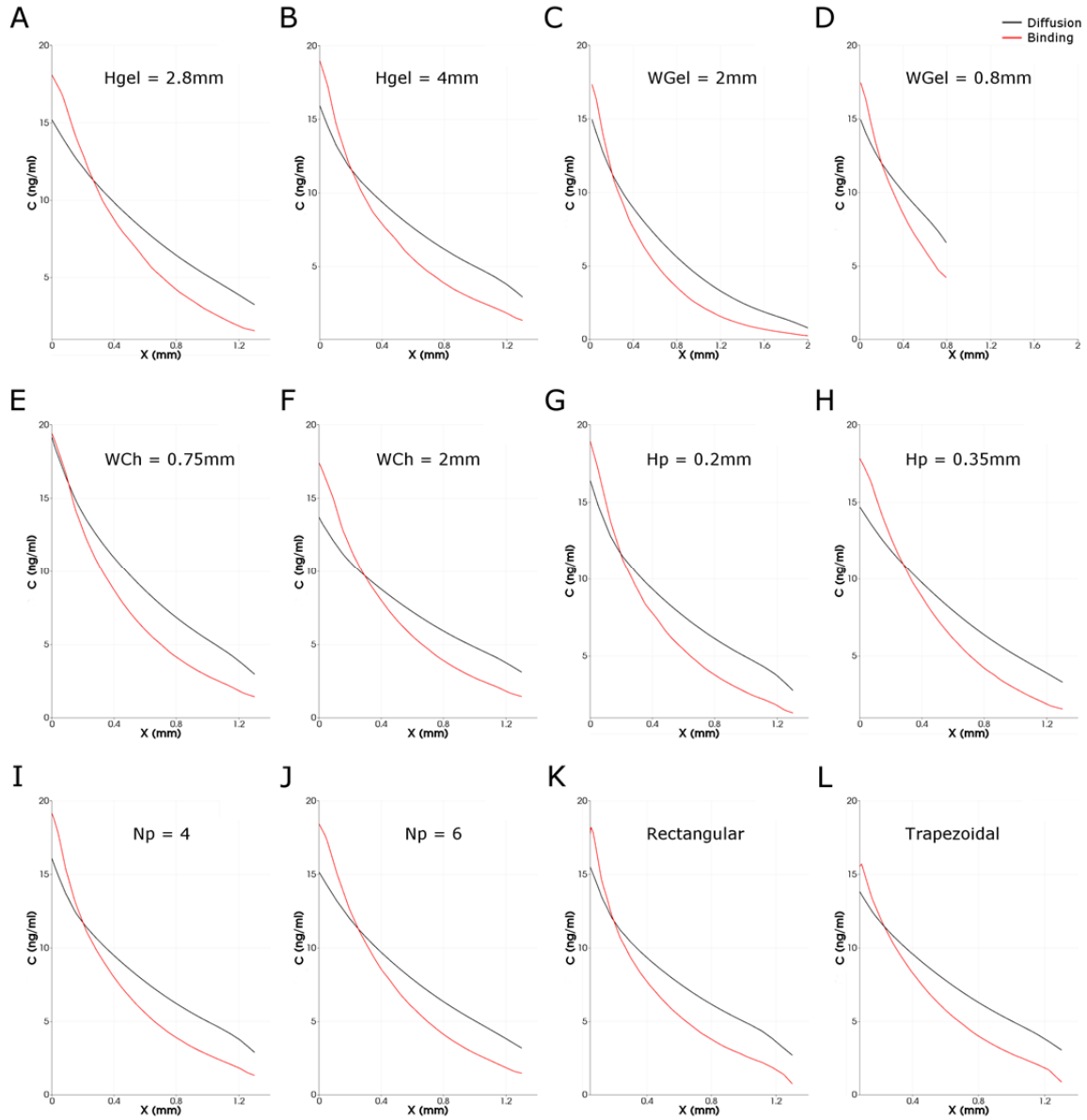


Figure 3.7: Results of the parametric analysis on chip-1 device.

Numerical predictions of diffusion and binding profiles after 24 hours of diffusion of PDGF-BB within a collagen type I hydrogel with: $H_{gel}=3.2\text{mm}$, $W_{gel}=1.3\text{mm}$, $W_{ch}=1\text{mm}$, $H_p=0.3\text{mm}$, $N_p=5$ (results showed in Figure 3.5A). Each panel shows the obtained results by varying the specified parameter: A) $H_{gel}=2.8\text{mm}$, B) $H_{gel}=4\text{mm}$, C) $W_{gel}=2\text{mm}$, D) $W_{gel}=0.8\text{mm}$, E) $W_{ch}=0.75\text{mm}$, F) $W_{ch}=2\text{mm}$, G) $H_p=0.2\text{mm}$, H) $H_p=0.35\text{mm}$, I) $N_p=4$, J) $N_p=6$, K) rectangular and L) trapezoidal type posts.

3.4.3. Numerical predictions of GF transport under different hydrogel combinations

Having explored the GF distribution within different microfluidic devices, the effect of the combination of different hydrogels inside a microfluidic device was studied. To that end, GF diffusion under two different hydrogel configurations within the chip-4 (the double channel device) was studied: collagen-fibrin and fibrin-collagen (see Figure 3.8). The simulated cases are the diffusion of PDGF-BB and TGF- β_1 growth factor between collagen and fibrin adjacent hydrogels under different configurations, and the total time simulated was 24 hours. The parameter values that define chip-4 device geometry are: $H_{gel}=3\text{mm}$, $W_{gel\ 1,2}=1.5\text{mm}$, $W_{ch}=0.9\text{mm}$, $H_p=0.25\text{mm}$, $N_p=5$ and with rectangular posts geometry.

To determine whether there were significant differences between diffusion gradients for the different simulated cases, the same initial concentration of GF was applied for each case (50ng/ml) and the total time simulated was 24 hours for all cases. The radius of TGF- β_1 particle was estimated from Protein Data Bank to be $3.8 \cdot 10^{-9}\text{m}$, which according to equation 3 corresponds to a standard diffusion coefficient of $1.49 \cdot 10^{-11}\text{m}^2/\text{s}$. The fibrin hydrogel characterization was previously performed with confocal reflection imaging and fibrin fiber radius was estimated to be $66.53 \pm 13.57\text{nm}$ (mean \pm se) and the fibrin void ratio to be $71.46 \pm 1\%$ (mean \pm se). The standard and effective coefficients of diffusion of PDGF-BB and TGF- β_1 in collagen and fibrin as well as the degradation and binding rates used in all simulations (experimentally adjusted, [179]) may be consulted in Table 3.2.

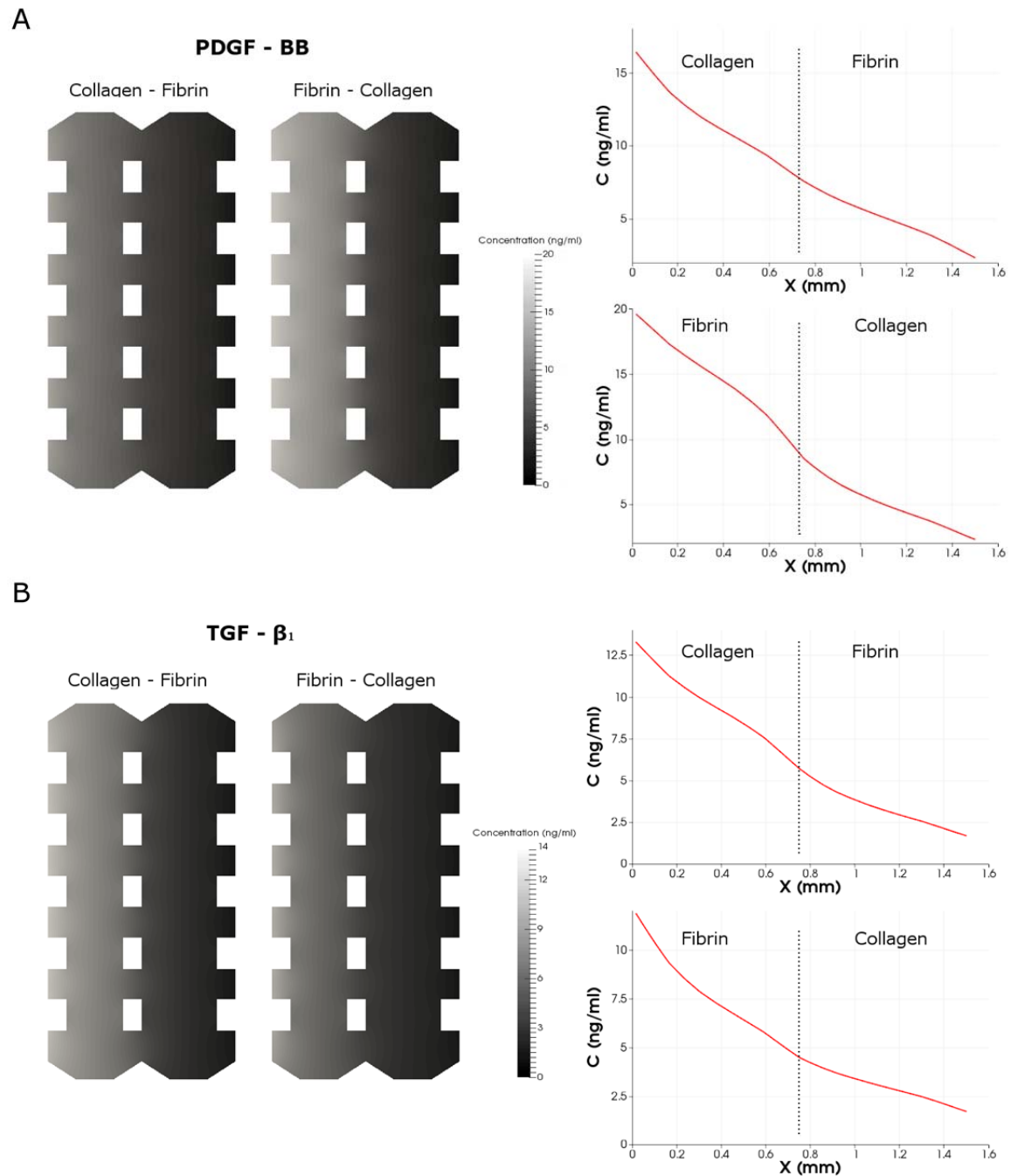


Figure 3.8: Effect of hydrogel combination on the diffusion profiles.

Numerical predictions of the spatial distribution and diffusion profiles obtained after 24 hours of diffusion of: A) PDGF-BB and B) TGF- β_1 , in collagen-fibrin and fibrin-collagen hydrogel configurations within chip-4 device.

Figure 3.8 shows diffusion profiles generated in the central domain of the device for the different studied cases. For both diffusion cases it can be found a slope change on the diffusion profiles as a consequence of a hydrogel domain change, which can be explained by the differences in the structural characteristics of each hydrogel, such as

the network concentration (pore size) or the fibril diameter. Moreover, the changes on the final concentration values obtained after 24 hours of GF diffusion simulation of PDGF-BB and TGF- β_1 can be mainly explained by the differences on the particle size and on the binding rates of each factor to the hydrogel.

Taken together, these results remark the importance to have a better knowledge on the behavior of a GF's within an extracellular matrix, more specially, in the interface between two different matrices or hydrogels to better understand relevant physiological processes such as wound healing processes. Actually, by this step-gradient hydrogel, we can recreate *in vitro* how cells behave under a strong alteration of the extracellular matrix guided by different chemical gradients [212]. Interestingly, these two-chambers microfluidic devices allowed us to analyze several cell functions through the interface of both materials and under different chemical gradients, including migration, proliferation, and matrix remodeling, in real time.

Parameter	Description	PDGF-BB	TGF- β_1
D_∞	Standard diffusion coefficient	$1.26 \cdot 10^{-11} \text{m}^2/\text{s}$	$1.49 \cdot 10^{-11} \text{m}^2/\text{s}$
D_c	Effective diffusion of a GF in collagen	$0.77 \cdot 10^{-11} \text{m}^2/\text{s}$	$0.92 \cdot 10^{-11} \text{m}^2/\text{s}$
D_f	Effective diffusion of a GF in fibrin	$0.70 \cdot 10^{-11} \text{m}^2/\text{s}$	$0.83 \cdot 10^{-11} \text{m}^2/\text{s}$
$K_{d,c}$	Degradation rate in collagen	$3 \cdot 10^{-6} \text{s}^{-1}$	$5 \cdot 10^{-6} \text{s}^{-1}$
$K_{d,f}$	Degradation rate in fibrin	$3 \cdot 10^{-6} \text{s}^{-1}$	$4.5 \cdot 10^{-6} \text{s}^{-1}$
$K_{b,c}$	Binding rate in collagen	$1 \cdot 10^{-5} \text{s}^{-1}$	$1 \cdot 10^{-5} \text{s}^{-1}$
$K_{b,f}$	Binding rate in fibrin	$1 \cdot 10^{-7} \text{s}^{-1}$	$2 \cdot 10^{-5} \text{s}^{-1}$

Table 3.2: Major parameters used in the simulations.

* c and f refers to collagen and fibrin hydrogels, respectively.

3.4.4. Automatic quantification of GF signaling: a web application

To facilitate the quantification of the chemical gradients generated within a synthetic hydrogel inside a microfluidic-based chip, an automatic quantification through a web application is presented. As proposed in materials and methods section, this application allows any user to automatically design a microfluidic device, starting from four different base models of microfluidic devices. Moreover, the user may choose the input parameters that define the diffusion case to simulate. The main objective of this application is to provide any user the characterization of gradient formation processes within a synthetic hydrogel and therefore reduce device design times and facilitate the experimental validation and parameter selection processes. To ensure the day-to-day applicability, user requirements were investigated prior to tool development (parametrical and sensibility study was performed) so that the 4 designs presented and their possible variations cover a wide range of common necessities. The tool may be consulted on http://m2be.unizar.es/insilico_cell under the *software* tab, and freely used by any user after registration. The use of this software is restricted to site members. Therefore, any user may register as a new user by filling the required fields.

Figure 3.9 shows the panel seen by the user after parameter selection (top) and the results returned to the website after the simulation (bottom). Chip-1 device was selected as example with the following geometric parameters of: $H_{gel}=3.2\text{mm}$, $W_{gel}=1.3\text{mm}$, $W_{ch}=0.8\text{mm}$, $H_p=0.3\text{mm}$, $N_p=5$ and with trapezoidal posts geometry. The diffusion case simulated was the PDGF-BB diffusion within a collagen type I hydrogel during 24 hours and with an initial concentration of the growth factor equal to 50 ng/ml.

Chip 1

These are the selected values:

Number of posts: 5
 Post height [mm]: 0.3
 Hydrogel scaffold height [mm]: 3.2
 Hydrogel scaffold width [mm]: 1.3
 Control channel width [mm]: 0.8
 Hydrogel type: 1
 Growth factor: 1
 Concentration of growth factor [ng/ml]: 50
 Time of simulation: 24

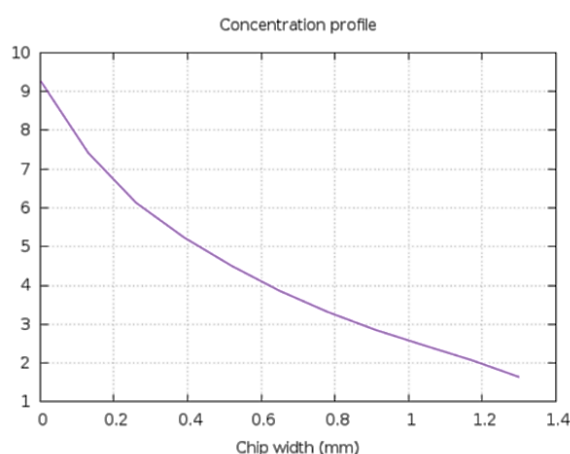
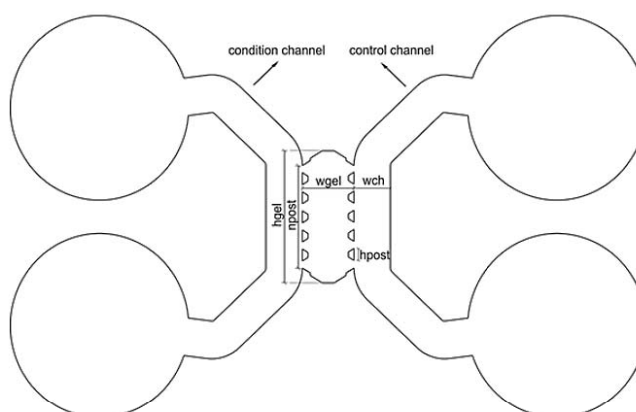


Figure 3.9: Web application screenshot.

Top panel shows the set of user-selected parameters as well as a scheme of the chosen chip. Bottom panel shows the diffusion profile generated within the hydrogel domain returned to the website, indicating the microfluidic device as well as the calculation parameters selected.

3.5. Discussion

Due to the importance that microfluidic technology has acquired during the last few years on *in vitro* 3-D cell cultures, multiple systems have been developed to study the mobility of cells under different controlled conditions, such as fluid flow and chemoattractant or chemorepellent molecules [212, 218, 219]. Thus, it is crucial to deeply study the spatio-temporal distribution of the chemical substances within a synthetic hydrogel to better understand the cell response under different signaling pathways.

The finite element model here presented is based on a reaction-diffusion transport model and allows an automatic prediction of the chemical gradients generated inside a microfluidic device for any GF or chemical substance for a wide range of geometries. Furthermore, a web-based application is developed to automatically calculate the spatio-temporal distribution of a growth factor, across hydrogel-based matrices (specifically collagen type I and fibrin) bringing to any user the opportunity to explore different geometries and conditions before investing on real experiments. In fact, this application yields an accurate prediction, based on previous experimental results, where diffusion phenomenon can be estimated within a microdevice. To that end, quantitative ELISA-assays for growth factor concentrations measurement were previously performed and the behavior of the dextran diffusion gradient was studied, validating therefore the numerical model proposed [179].

Firstly, four different microfluidic device geometries were defined to study the dependence of the geometrical parameters onto the gradient formation processes. To that end, and to notably decrease the computational time, a simplification of the device geometry was performed (disregarding the deposits) and assuming that the chemical factor diffuses homogeneously throughout the condition channel of the device and the initial growth factor concentration is constant in both lateral channels. The numerical predictions obtained after diffusion of 50 ng/ml of PDGF-BB within a collagen gels for the four different models of microfluidic devices, showed differences on the concentration profiles obtained for each case.

Thus, to understand how the different parameters that characterize these microfluidic devices influence the behavior of the diffusion processes in 3-D, an intensive multiparametric analysis was performed. As expected, the results demonstrate that growth factor diffusion within 3-D matrices clearly depends not only on the physics of diffusion, but also on the geometrical parameters that characterizes these complex devices. Consequently, and after studying the diffusion and binding profiles generated for the different cases, we found a stronger impact on the gradient formation process for the following parameters: the hydrogel scaffold height and width (H_{gel} and W_{gel}), the lateral channels width (W_{ch}), the post height (H_p) and the number of posts (N_p). Differences on concentration for condition and control channels with respect to the

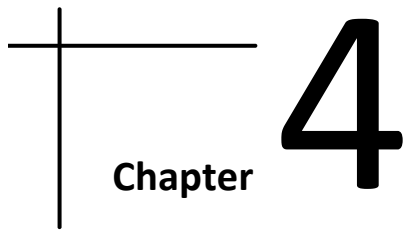
reference case (chip-1 with the reference parameter values) were quantified. For instance, changes on hydrogel width generated differences of up to 21% on condition channel concentration and of about 24% on control channel concentrations; and changes on post height showed differences of 6% on condition channel concentration and of 13% on control channel concentrations.

Additionally, the effect of the combination of different hydrogels inside a microfluidic device was investigated. In particular, PDGF-BB and TGF- β_1 diffusion under two different hydrogel configurations within the chip-4 was studied: collagen-fibrin and fibrin-collagen. Results showed differences on the slope of the diffusion profiles generated in the central domain of the device for the different cases of study, then highlighting the importance of studying the combination of different matrices or hydrogels on physiologically relevant microenvironments.

To understand the spatial distribution of the complex chemical gradient generated by diffusion into the hydrogel scaffold, two-dimensional finite element simulations have been previously presented by using commercial software's, such as COMSOL or ANSYS [220, 221]. However, the commercial software's do not offer the possibility to determine the concentration gradients as a function of a reactive term that incorporates additional phenomena, such as the degradation and the binding of the factor to the fibrillar network.

In sum, the novel web application here presented provides to any user an automatic estimation of growth factor diffusion within 3-dimensional matrices inside a microfluidic device without prior knowledge of CAD or Finite element modeling. This application allows the user to design his/her own device by defining online the main geometrical parameters that characterize these devices (hydrogel height and width, lateral channels width, post height and number of posts); as well as the input parameters that define the diffusion case: the growth factor to diffuse (PDGF-BB and TGF- β_1), the initial growth factor concentration, the type of matrix (collagen or fibrin) and the diffusion time to simulate. Thus, the automatization of microfluidic device geometries generation provide a powerful tool which facilitates to any user the possibility to automatically create its own microfluidic device, greatly reducing the

experimental validation processes and advancing in the understanding of *in vitro* 3-D cell responses without the necessity of using commercial software or performing real testing experiments.



Chapter 4

RECURSIVE METHOD FOR RECONSTRUCTING CELL TRACTION FORCES

Cell traction forces are crucial in many biological processes such as inflammation, wound healing, angiogenesis and metastasis. Consequently, the ability to measure cellular traction forces is critical to better understand the cellular and molecular mechanisms behind many basic biological processes at both cell and tissue level. This chapter presents a novel numerical model for solving cell traction forces on non-linear materials by using a finite element approach. To illustrate the proposed recursive method, it is applied to human dermal fibroblast cells (NHDF) migrating inside a 2 mg/ml collagen-based gels. Finally, this chapter discusses how the mechanical properties of both cell and collagen gel determine the quality of the predictions⁷.

⁷ This chapter will be published in: M. C ndor and J.M. Garc a-Aznar, *A recursive finite element-based approach for solving inverse problems in traction force microscopy* (in preparation).

4.1. Introduction

Cell migration through a 3-D matrix depends strongly on the ability of cells to generate traction forces. In contrast to cell migration in a 2-D matrix, when cells migrate through a 3-D matrix, they must overcome not only the adhesion forces, but also the resisting forces imposed by the surrounding matrix [9, 11, 222]. Thus, traction forces exerted by cells during cell migration depend not only on the matrix properties but also on the cell properties and shape. For that reason, studying the dependency of these forces on the mechanical properties of cells and the surrounding matrix is therefore important for a mechanistic understanding of many physiological and pathological cell functions in health and disease that involve cell adhesion, shape changes and migration [8, 20-23].

Traction forces can be computed from cell-induced deformation of the matrix, using different mathematical frameworks. Basically, the displacement field of the hydrogel caused by the cell tractions is quantified by tracking the positions of embedded beads before and after cell tractions are relaxed with a drug cocktail containing trypsin and/or high concentrations of actin-disrupting drugs such as cytochalasin-D. Once the matrix displacements are known, the matrix strain field can be computed [223].

In order to quantitatively measure the traction field generated during cell migration, several techniques have been developed. These include surface wrinkle analysis, deflection of micropillars and Traction Force Microscopy (TFM) [35, 78, 103, 113, 224, 225]. The most popular technique relies on the Boussinesq solution in the Fourier space, the so called Fourier Transform Traction Cytometry (FTTC) [102, 103], but this solution is limited for 2-D substrates undergoing small strains (with a linear elastic behavior of the substrate). However, more recent studies have demonstrated important differences when comparing cell behavior in 2-D vs. 3-D environments. Accordingly, 3-D TFM techniques have increased in sophistication and now feature high-spatial displacement resolution and advanced computation formalisms to connect the displacement information to complex material constitutive laws [101, 225, 226].

To measure the 3-D forces several research groups, such as Legant et al. have proposed the use of Finite Element Methods (FEM) to solve the inverse problem [113].

However, previously published approaches mostly ignore the non-linear behavior of 3-D biopolymer networks, such as reconstituted collagen gels. There have been only a few attempts at solving 3-D non-linear TFM problem [115-117], by using non-linear constitutive models and finite element analysis.

Some of the previous models assumed idealized shapes for cells and intracellular structures and just a few of studies used microscopy-based realistic cell geometries for cell traction forces reconstruction [113, 116, 177]. The precise knowledge of the cell surface domain contributes to reducing the computational cost for solving the inverse method, while at the same time provides the possibility to understand the effect of internal cell properties and other intracellular structures on the cell traction forces reconstruction.

In this chapter, we describe a method for quantifying cell traction forces during cell migration in physiologically relevant 3-D matrices with highly non-linear mechanical properties, such as collagen type-I hydrogels. To that end, we use Laser Scanning Confocal Microscopy (LSCM) images of human dermal fibroblast (NHDF-GFP) to develop 3-D finite element models of *in vitro* cell geometries. Subsequently, these models are used to explore the influence of both cell and matrix mechanical properties on the cell traction force reconstruction method. The imaging of cells was performed inside the microfluidic-based chip presented in chapter 3, to ensure live cell conditions and to recreate the physiological microenvironment of real tissues [212]. Moreover, microfluidic devices allow us to have a better control of the boundary conditions of the problem to solve.

We propose a numerical method to solve the inverse problem based on a recursive optimization algorithm. The objective function is defined by least-square minimization of the difference between the target/measured and the computed deformed configuration of the cell by means of a recursive formulation, which is based on the solution of several direct mechanical problems. First, from the measured deformed configuration the known displacements serve as boundary conditions for the first direct mechanical problem to be solved. Subsequently, the reaction forces obtained on the previous direct calculation serve as boundary conditions for the second direct

mechanical problem to be solved. The so obtained deformed configuration is compared with the measured deformed configuration. If this difference is smaller than a critical value, the iterative algorithm has converged to a solution. If not, this process is repeated until convergence is achieved. Moreover, this method presents a well-posed discretizing inverse elasticity problem in the absence of regularization, as demonstrated in other previous works [227].

To illustrate the proposed recursive method we apply the theoretical model to some examples where cell traction forces are computed on real geometries of human dermal fibroblast cells (NHDF) migrating inside a 2 mg/ml collagen-based gels. Moreover, the effect of incorporating the real mechanical properties of both domains (cell and hydrogel) onto the cell traction force solution obtained with the FEM method is investigated.

4.2. Material and methods

In this section, the different methodologies used for imaging living cells inside a microfluidic-based device are presented. Moreover, a methodology for generating 3-D FE models of single cells migrating in a 3-D matrix is introduced, which will be subsequently used for studying the dependency of cell traction forces with the mechanical properties of cells and the surrounding matrices. Finally, the numerical method for solving cell traction forces is presented.

4.2.1. Cell culture and preparation of 3D collagen gels

Normal human dermal fibroblast (NHDF, obtained from Lonza) transfected with lentiviral particles and isolated by cell sorting were kept in 25cm² cell culture flasks with Fibroblast Growth Medium-2 (FGM-2 BulletKit, Lonza) at cell culture conditions (37°C, 5% CO₂ and 95% humidity). GFP-expressing fibroblasts (NHDF-GFP) were passaged every 2nd day using 0.05% trypsin/EDTA.

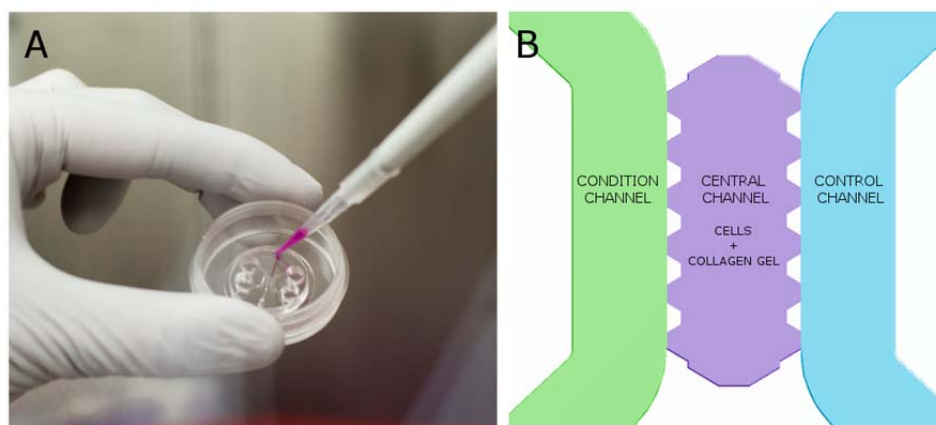


Figure 4.1: Preparation of collagen gels for injection into a microfluidic device.

A) Collagen gel injection within a microfluidic device before gel polymerization. B) Detail of the central area of the device, where the hydrogel is injected in the central channel of the device (purple, whose dimensions are 2.5 x 1.3 mm) and both lateral channels (green and blue) are filled with complete cell culture media.

To prepare 200 μl of 2 mg/ml collagen type I hydrogels, we carefully mixed 133.3 μl of rat tail collagen (3mg/ml, BD Bioscience), 20 μl 10x Dulbecco's Phosphate Buffered Saline (DPBS, Gibco), 10.3 μl of distilled water and 6.4 μl of Sodium hydroxide (0.5N NaOH, Sigma) to adjust the pH to 7.4 of the collagen solution. 30 μl of NHDF-GFP cells suspended in complete cell culture medium (FGM-2, Lonza) were carefully mixed with the final collagen solution before gel polymerization at a ratio of 50000 cells/ ml. All ingredients were kept on ice during the collagen preparation process. 20 μl of the final cell-collagen solution was pipetted within a microfluidic device (see Figure 4.1) and polymerized in a tissue culture incubator at 37°C, 95% relative humidity and 5% CO₂ for 20 minutes. After polymerization time, 300 μl of complete cell culture medium was added in both lateral channels to prevent dehydration of the collagen gel. For more information about the critical parameters and troubleshooting for the collagen gels preparation see a recent published protocol [223].

4.2.2. Live cell imaging inside a microfluidic device

After overnight cell-collagen solution co-incubation within microfluidic devices, individual live cell imaging was performed. Confocal microscopy imaging (Nikon D-Eclipse C1 Confocal Microscope) with a Plan Fluor 40x/1.30 Oil objective was used to obtain a set of planar images that will subsequently be used to reconstruct the 3D

individual cell geometry, as well as to compute the traction force-induced deformations of the biopolymer network. The image stack is recorded by exciting the samples with a 488 nm Argon laser (green channel), with a distance of the confocal z-sections of 0.63 μm (see Figure 4.2A).

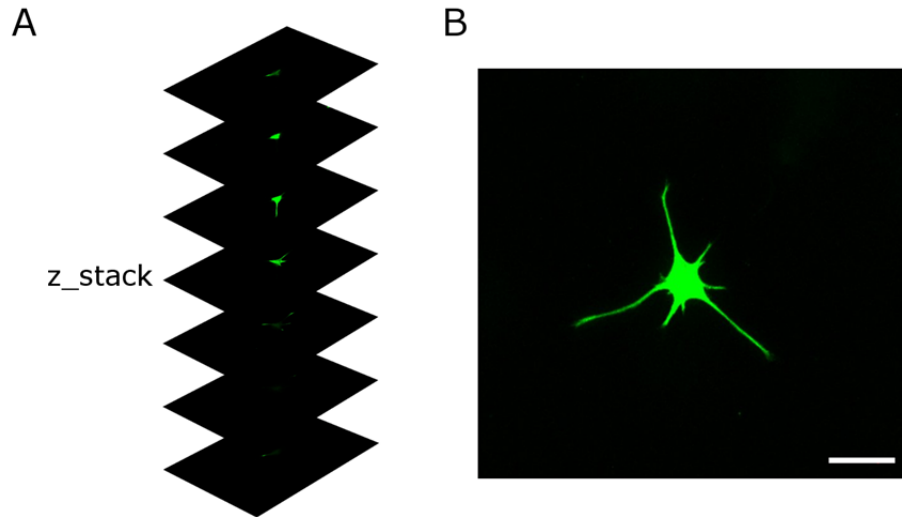


Figure 4.2: Confocal microscopy imaging of an individual NHDF-GFP live cell spreading into a 3-D collagen gel.

A) Representative focal planes of an image z-stack. B) Volume rendering of an individual cell (green), based on a set of planar confocal images. Scale bar is 50 μm .

With typically 100 z-stacks and 512×512 pixels in the x-y plane, voxel dimensions selected for the cell image acquisition were 0.63 μm horizontally in the x and y direction, and also 0.63 μm vertically in the z direction. The selected cell is always located at least 50 μm away from the top or bottom gel surface or from neighboring cells, to avoid the contact with the microfluidic device and with neighboring cells. Before selecting a cell for imaging, it is also checked that the hydrogel in the region of interest does not show any irregularities. To ensure physiologically imaging conditions within the imaging chamber, cell culture conditions (37°C, 5% CO₂ and 95% humidity) were maintained during all time lapse recording.

4.2.3. 3-D cell-specific segmentation and FE mesh development

The individual cell geometry is reconstructed by using the image z-stack which corresponds with the deformed configuration. The image stack is imported to *Mimics*® software (18.0 Materialise, Belgium) and a semiautomatic segmentation of the cell and the collagen gel is performed for their corresponding 3-D geometrical reconstruction (Figure 4.3A-B). Both single cell and collagen gel geometries are subsequently exported to *3-matic*® software (10.0 Materialise, Belgium) and the individual surface FE meshes are generated using a semi-automatic meshing procedure. A non-manifold assembly is defined between the cell geometry and the collagen gel to obtain a more realistic result avoiding mesh discontinuities and frictional effects between both geometries in the following FE simulations. Finally, the volume mesh of the assembly (see Figure 4.3C) is exported to *Abaqus*™ software (6.13 Dassault Systèmes Simulia Corp., France) to perform the finite element analyses.

The volume mesh of the assembly is constructed using 4-node 3-D linear tetrahedral elements (C3D4) with a maximum element size of 3 μm for the cell geometry and 10 μm for the collagen gel (see Figure 4.3C). The element size was inside the asymptotic region of convergence and represented a good trade-off between numerical accuracy and computational cost for all cases.

A sensitivity analysis was performed to determine the optimal mesh size for the collagen gel elements to obtain an accurate solution. Three different tetrahedral element sizes were tested: 8 μm , 10 μm and 12 μm ; resulting in a maximum element size of 10 μm for the gel elements. The resulting 3-D FEM is shown in Figure 4.3C and consists of 14774 cell elements and 327264 elements for the collagen gel.

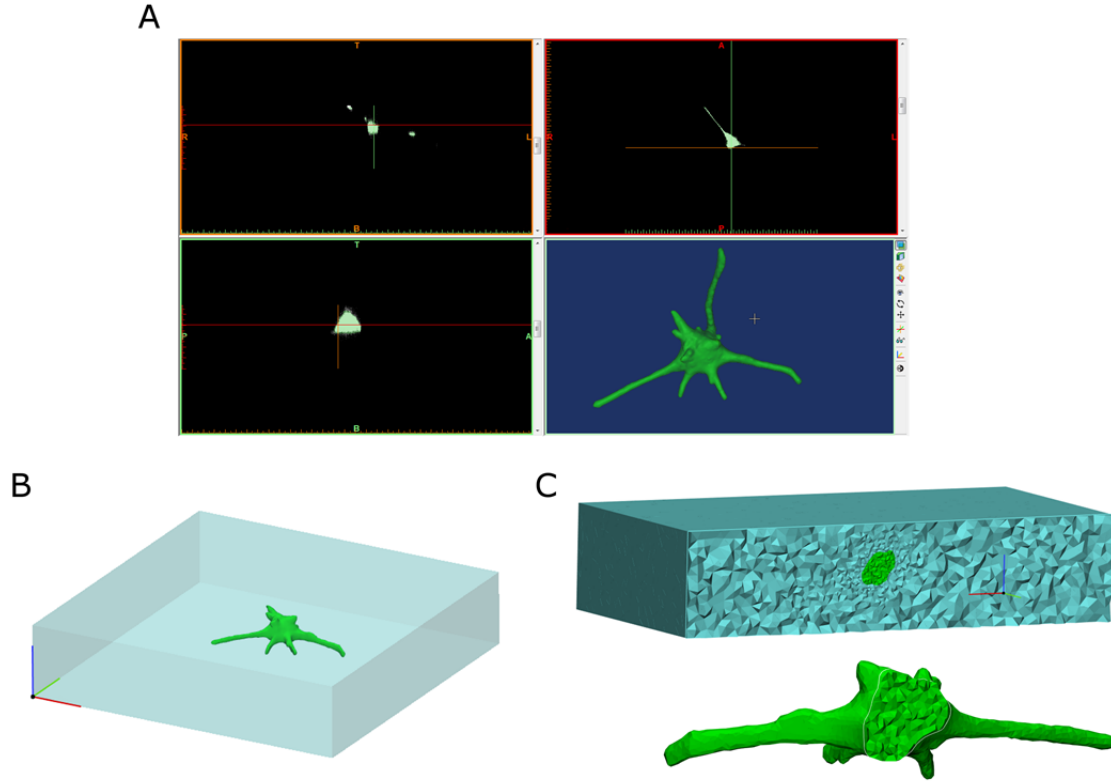


Figure 4.3: Generation of a three-dimensional finite element mesh of a NHDF-GFP cell embedded on a 2 mg/ml collagen type-I hydrogel.

A) Segmentation and 3-D reconstruction of a NHDF-GFP live cell geometry. B) Assembly of both cell and collagen gel geometries. C) 3-D FE mesh of an individual NHDF-GFP cell embedded in a collagen gel.

4.2.4. 3-D finite element model and examples of application

To solve cell traction forces during cell migration, both 3-D cell and collagen geometries and meshes were imported to the FE solver *Abaqus™*. The 3-D FEM used in the simulations is shown in Figure 4.3C and all model components were modeled with 4-node 3-D linear tetrahedral elements (C3D4).

In the simulations, it is assumed that both cell and collagen gel are elastic and are modeled as isotropic compressible materials with a Neo-Hookean strain energy density function [177], with the following constitutive relationship:

$$W = C_{10}(\bar{I}_1 - 3) + \frac{1}{D_1}(J_{el} - 1)^2 \quad (4.1)$$

where W is the strain energy per unit of reference volume, C_{10} and D_1 are the material constants, I_1 is the first deviatoric strain invariant and J_{el} is the elastic volume ratio. Thus, to define the Neo-Hookean materials both C_{10} and D_1 parameters must be known and can be formulated as a function of the initial shear and bulk modulus.

In this work, different examples of application have been simulated to test the inverse numerical model proposed and to investigate the effect of introducing the correct cell properties onto the cell traction forces solution. To that end, different Neo-Hookean materials are defined for both cell and hydrogel domains. In the first simulations, cell cytoskeleton shear and bulk modulus are defined as 84 Pa and 5 KPa respectively, assuming cells as an incompressible material with a Poisson's ratio of 0.49 [228]. The shear and bulk modulus for the collagen gels are defined as 40 Pa and 2.1 KPa respectively [229]. Collagen gels are assumed as well as an incompressible material with a Poisson's ratio of 0.49 [115]. In the following, this case is referred as *Cell + gel* case. In a second set of simulations, all the bulk is considered with the same material behavior, assuming that both cell and hydrogel domains have the hydrogel material. This case will be referred in the following as *All gel* case.

Finally, and with the aim to study the effect of considering the correct cell properties onto the cell traction forces solution, two new cases are presented by only varying the mechanical properties of the cell domain. In the first scenario, the shear modulus of the cell domain is increased to 168 Pa. In the second scenario, cell's shear modulus was doubled from the original values to 336 Pa. In these two cases the mechanical properties of the gel domain remain unchanged. These two cases will be referred in the following as *Cell* + gel* and *Cell** + gel* cases. Notwithstanding that only non-linear materials have been used to solve traction forces in the numerical examples here presented, this model provides the possibility to implement any type of material model, linear or non-linear, to solve cell traction forces.

The loading conditions used in the simulations are subsequently detailed in the numerical model section where the inverse approach is explained. The collagen gel boundary conditions were set to mimic those of the TFM experiments with frictionless interactions between the cell and collagen gel contact surface. Furthermore,

displacements were constrained in all directions of the external surface nodes of the collagen gel ($u_x = u_y = u_z = 0$), since a zero displacement field was quantified in the collagen gel boundary.

4.3. Numerical reconstruction of cell traction forces

In this section, a numerical method for solving cell traction forces on non-linear materials is presented. To that end, a recursive formulation is used by combining different finite element analyses.

4.3.1. Introduction

To determine individual cell traction forces, a numerical method to solve the inverse problem based on a recursive optimization is presented, as a function of the deformation field induced on the surrounding matrix after inducing cell relaxation. The whole domain $\Omega \subset \mathbb{R}^3$ is composed of two elastic domains Ω_{cell} and Ω_{matrix} which are separated by a surface Γ (see Figure 4.4). Along this interior surface Γ , a traction field t acts, which is unknown, and leads to the deformation of the matrix domain. The displacement u^* of this deformation is experimentally measured in some parts of the matrix domain Ω_{matrix} .

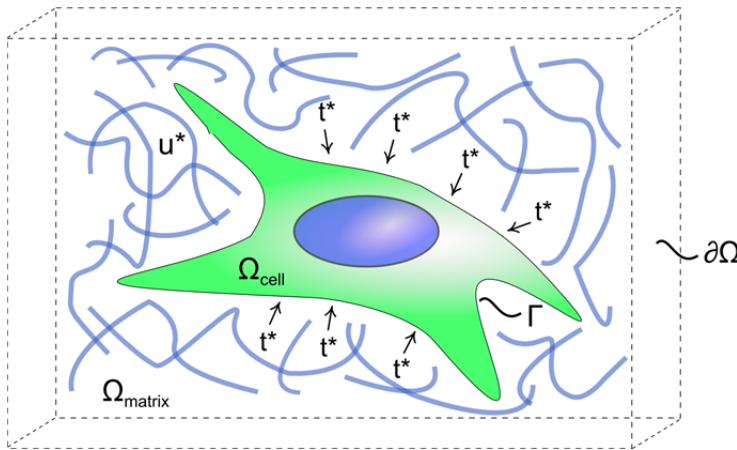


Figure 4.4: Deformed configuration of the problem.

The measured displacement field in the gel domain is u^* , Ω_{cell} and Ω_{matrix} are the cell and matrix domain respectively, Γ refers to the cell-matrix surface domain, $\partial\Omega$ to the gel contour domain and t^* is the traction field in the cell boundary.

Let u denote the displacement field and u_i is the restriction to the domain Ω_i , where $i = \{cell, matrix\}$. Therefore, the mechanical problem for determining the cell traction forces is defined by:

$$\begin{aligned}
 \nabla \cdot \sigma(u_i) &= 0 & x \in \Omega_i \\
 u_{matrix} &= 0 & x \in \partial\Omega \\
 \sigma_{cell} \cdot n &= t^* & x \in \Gamma \\
 u_{cell} &= u_{matrix} & x \in \Gamma
 \end{aligned} \tag{4.2}$$

where t^* is a given traction field in the cell boundary, which is the unknown variable of the problem, and ensuring that the displacement field in the matrix domain fulfils that:

$$u_{matrix} = u^* \quad x \in \Omega_{matrix}.$$

In both cell Ω_{cell} and matrix Ω_{matrix} domains is assumed to be a non-linear elastic material as detailed above in the finite element model subsection.

The inverse problem is solved as an optimization problem, where the cell traction forces are computed by minimizing the difference between the target/measured deformed configuration u^* and the current computed configuration $u^{computed}$ of the cell, by means of a recursive algorithm (see Figure 4.5). First, from the target deformed configuration, a direct mechanical problem is computed, where the known displacement field serves as boundary conditions. Subsequently, the reaction forces obtained on the previous direct calculation serve as boundary conditions for the second direct mechanical problem to be solved. The so obtained deformed configuration $u^{computed}$ is compared with the measured deformed configuration. Basically, if this difference is smaller than a critical value, the iterative algorithm has converged to a solution. If not, this process is repeated until convergence is achieved.

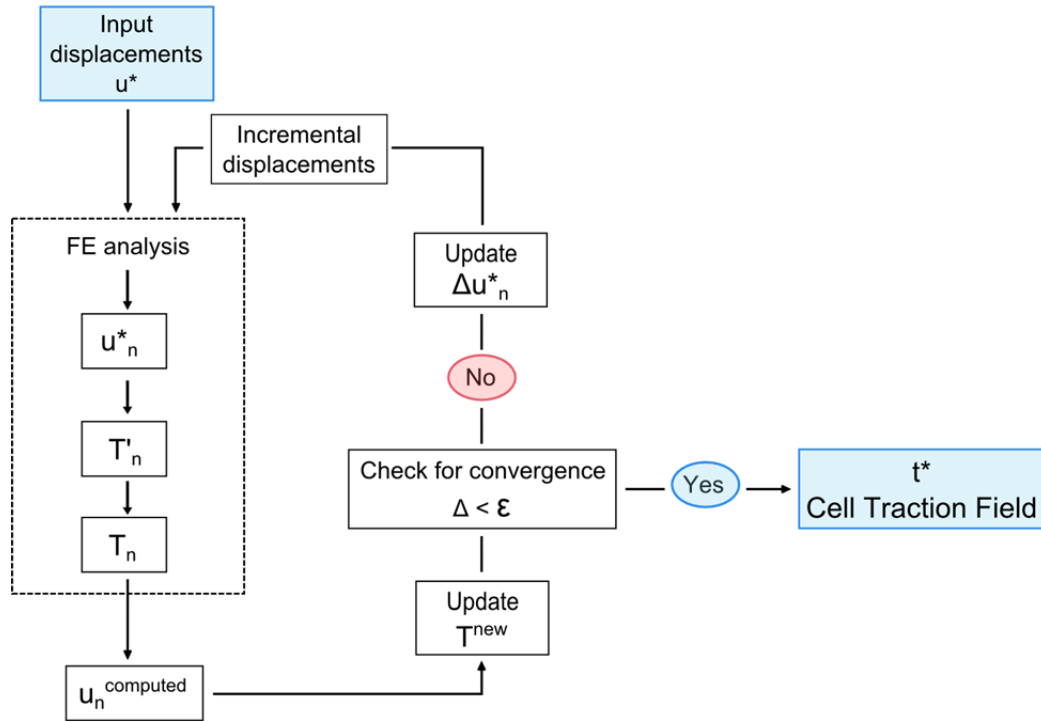


Figure 4.5: Schema of the recursive algorithm.

The algorithm starts to iterate with an input displacement field u^* , which can be obtained experimentally or computationally. Three different FE analyses are computed to obtain a set of intermediate reaction forces T' and cell traction forces T at the cell boundary domain, as well as the computed displacement field $u^{computed}$ at the gel domain, which is used to calculate a cell traction field at the cell contour domain. The process is repeated until convergence is achieved, which means that a possible cell traction field has been found.

4.3.2. Direct problem for determining the reaction forces

In this section, it is presented briefly the direct mechanical problem, where the measured field of displacements u^* is imposed in order to evaluate some intermediate reaction forces:

$$\begin{aligned}
 \nabla \cdot \sigma(u_{matrix}) &= 0 & x \in \Omega_{matrix} \\
 u_{matrix} &= 0 & x \in \partial\Omega \\
 u_{matrix} &= u^* & x \in \Omega_{matrix} \\
 u_{matrix} &= 0 & x \in \Gamma
 \end{aligned} \tag{4.3}$$

From this analysis, the reaction forces T' at the cell boundary Γ are computed.

4.3.3. Direct problem for applying reaction forces and determining traction forces

In this second direct mechanical problem, a new deformation field of the matrix domain is determined, by applying the reaction forces previously obtained as external forces on the cell boundary:

$$\begin{aligned}
 \nabla \cdot \sigma(u_i) &= 0 & x \in \Omega_i \\
 u_{matrix} &= 0 & x \in \partial\Omega \\
 \sigma_{cell} \cdot n &= -T' & x \in \Gamma \\
 u_{cell} &= u_{matrix} & x \in \Gamma
 \end{aligned} \tag{4.4}$$

After applying the reaction forces T' , a preliminary displacement field in the matrix domain $u'^{computed}$ is computed.

Then, the traction forces are adjusted by minimizing the mismatch between the simulated or computed displacement field $u'^{computed}$ and the measured local gel displacement field u^* as:

$$u^* \simeq w \circ u'^{computed} \tag{4.5}$$

where $w = \{w_x, w_y, w_z\}$ components are determined by means of the least-squares solution and \circ denotes the so-called entry-wise Hadamard or Schur multiplication.

Then, a possible solution of the cell traction field is estimated as:

$$T = w \circ (-T') \tag{4.6}$$

After this iteration, the same direct mechanical problem is solved but now using the current computed cell traction field T :

$$\begin{aligned}
 \nabla \cdot \sigma(u_i) &= 0 & x \in \Omega_i \\
 u_{matrix} &= 0 & x \in \partial\Omega \\
 \sigma_{cell} \cdot n &= T & x \in \Gamma \\
 u_{cell} &= u_{matrix} & x \in \Gamma
 \end{aligned} \tag{4.7}$$

from which the full displacement field of the matrix domain $u^{computed}$ is obtained.

4.3.4. Recursive formulation for solving the inverse form problem

In order to solve the inverse problem, a recursive algorithm is developed by using the direct mechanical formulations described above. Following the scheme shown in Figure 4.5, initially, a known displacement field is applied in the gel domain u^* to finally obtain a cell traction field T in the cell contour domain Γ . The application of this traction field results in a computed displacement field. In order to address if the computed displacement field $u^{computed}$ matches the bead displacements generated in the bulk u^* , the error in the computed displacements are compared quantitatively according to:

$$\Delta = \frac{\sum_1^N \frac{\|u^* - u^{computed}\|_2}{\|u^*\|_2}}{N} \quad (4.8)$$

where the norms are the Euclidean norms and N are the number of nodes of the gel domain.

If $\Delta < \varepsilon$ is verified in the entire gel domain, with a convergence tolerance $\Delta < 1.10^{-2}$, the searched deformed matrix configuration u^* was found. If the convergence tolerance is not reached, the process is repeated until convergence is achieved. A new input displacement field Δu^* is defined for the next iteration as the difference between the target displacement and the computed displacement field:

$$\Delta u^* = u^* - u^{computed} \quad (4.9)$$

This new displacement field Δu^* is used in Eq. 4.3, obtaining a new increment of the reaction forces ΔT in the cell boundary domain Γ . This increment of traction forces is therefore added to the previous computed traction forces as:

$$T^{new} = T + \Delta T \quad (4.10)$$

This recursive algorithm is repeated until convergence is reached (see Figure 4.5).

4.4. Results

In this section, the main results of the numerical simulations are presented. First, a cell contraction is simulated by using a real cell geometry, therefore obtaining a displacement field that will be used as input of the inverse algorithm in the following simulations. Next, the inverse solution is computed for different examples to test the inverse numerical model proposed and to investigate the effect of considering the correct cell properties for the cell traction force solution.

4.4.1. Direct problem: Determination of the input displacement field

To illustrate the proposed recursive method, we have applied the theoretical model to some illustrative examples by using real cell geometries obtained experimentally, in particular normal human dermal fibroblasts (NHDF) migrating inside a 2 mg/ml collagen-based gels. In TFM, to compute cell traction forces, it is necessary to know the displacement field generated after cell relaxation with a drug cocktail. To precisely quantify the displacement field in the collagen gel domain, TFM algorithms used the tracking of 3-D positions of fluorescent beads tightly embedded in the collagen matrix [120].

To mimic the displacement field obtained in real experiments, a direct force was simulated, thereby obtaining a displacement field u^* in the gel domain that will subsequently be used as input of the inverse algorithm. To that end, forces at cell boundary nodes along all cell protrusions were applied in the 3 directions $t^{in\ silico} = (t_x, t_y, t_z)$. The direction of the traction field applied is pointed to the cell center to simulate traction fields previously obtained experimentally [167]. The material properties for both domains were defined before, in the finite element model section. The magnitude of the computed displacement field is shown in Figure 4.6. The calculations were performed with the FE solver Abaqus™ 6.13.

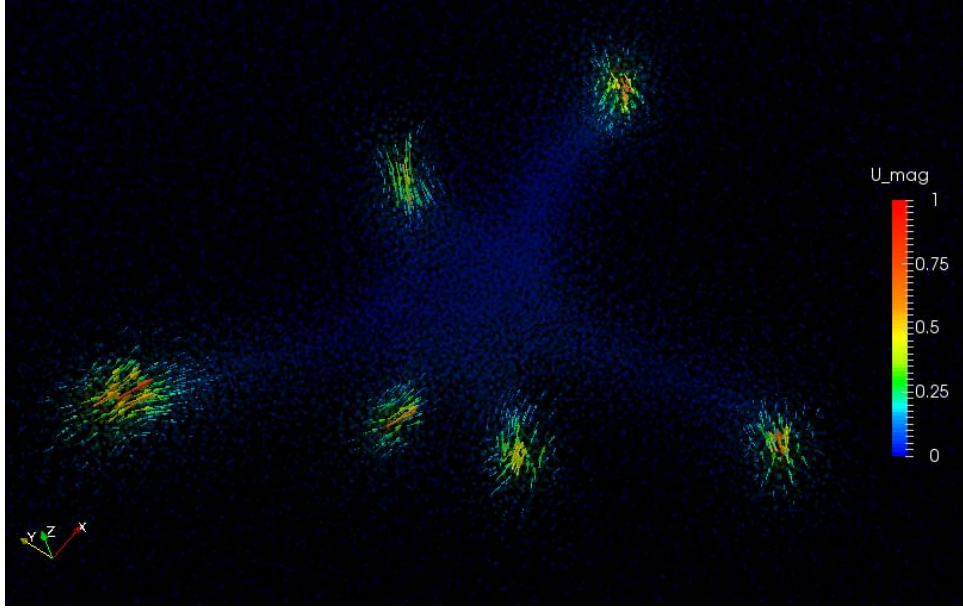


Figure 4.6: Simulated displacement field around an individual NHDF cell. The magnitude of the displacements vectors are in microns.

As expected, the maximum displacement values are obtained at the tip of each cell protrusion and close to the cell-matrix interface area (see Figure 4.6), which correlates with sites where tractions forces are applied.

4.4.2. Inverse FE problem: Numerical model validation

In this section, the inverse solution is computed for different examples to test the inverse numerical model proposed. To evaluate the predictive capacity of the inverse model, the error obtained in the displacements field is quantified by means of Eq. 4.8.

Moreover, to test the accuracy of the inverse solution the error in the computed cell tractions is compared quantitatively according to:

$$ECT = \frac{\sum_1^N \frac{\|t^* - t^{in\ silico}\|_2}{\|t^*\|_2}}{N} \quad (4.11)$$

where the norms are the Euclidean norms, in this case N are the number of nodes of the cell contour domain, t^* are the searched or computed traction forces and $t^{in\ silico}$ refers to the set of traction forces applied on the cell domain.

Two different cases are considered to test the inverse numerical model proposed. In the first scenario, tractions are solved through the inverse algorithm by using the

same mechanical properties used to solve the forward problem presented before. In a second case, the traction solution was computed by using the inverse method but now the entire sample volume is considered as a single material, so we ignore the cell body. To that end, the Neo-Hookean material used to describe the mechanical behavior of the collagen gel is also used to define the mechanical behavior of the cell domain. This last case was postulated with the aim to understand the effect of considering the real cell properties for the traction reconstruction through inverse algorithms. These two cases are referred as *Cell + gel* and *All gel* case.

The input displacement field of the inverse algorithm is common for both cases, those showed in Figure 4.6. The resulting tractions vectors obtained for both cases are shown in Figure 4.7.

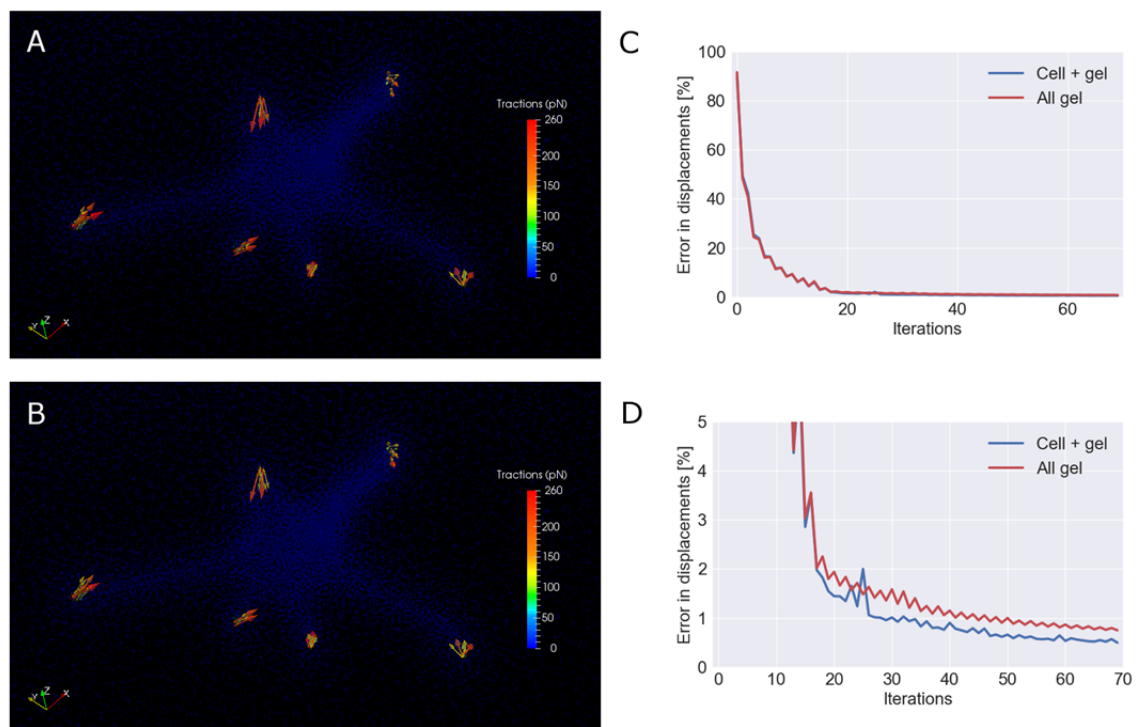


Figure 4.7: Traction maps predicted around an individual NHDF cell.

The magnitude of the tractions for: A) *Cell + gel* case, where the cell properties are the same used in the forward case (shear modulus of 84 Pa for cell cytoskeleton and 40 Pa for the gel domain, both are considered incompressible materials) and B) *All gel* case, where the mechanical properties in the cell domain are assumed equal than properties in the gel domain (shear modulus of 40 Pa for the entire domain, both are considered incompressible materials). C) Percentage of error committed for each iteration for *Cell + gel* and *All gel* cases. D) Detail of the convergence curve for both *Cell + gel* and *All gel* cases.

As shown in Figure 4.7, the maximum values of the computed tractions are pointed to the cell center for all cell protrusions. Only traction values are obtained in those nodes of the cell boundary where initially a force was applied in the direct case. For the rest of the cell boundary nodes, traction values are smaller than 5 pN. This effect may be due to the fact that a point force was applied in some nodes of cell protrusions instead of a smoothly interpolated load between other nodes of the region. To avoid the contribution of these residual forces to the computation of the error on the cell traction forces (ECT), the force vectors with values smaller than 10% of the maximum force value has not been taken into account for the calculation of the error.

The convergence on the first case (*Cell + gel*) is achieved after 29 iterations and the error obtained in the computed displacement field is equal to 0.95%. In the second case (*All gel*), where cell properties are assumed to be equal to the gel properties, the convergence is achieved after 43 iterations with an error in the resulted displacement field of 0.98%. Thus, these results indicate that the mechanical properties of the cell domain are affecting the cell traction force solution convergence (see Figure 4.7D). However, both cases showed errors in displacements smaller than 2%, after less than 20 iterations (see Figure 4.7C-D).

Regarding the traction maps, the resulted tractions vectors in the *All gel* case are relatively smaller than those obtained in the *Cell + gel* case. The error obtained in the computed traction field is equal to 5%, by means of eq 4.11. The maximum traction force obtained in the *All gel* case is equal to 243 pN, in contrast to the maximum force value obtained in the case of *Cell + gel* of 255 pN. Moreover, when comparing both cases, small changes may also be appreciated in the direction of the traction vectors, for example in the top right protrusion of the cell (see Figure 4.7A-B). However, traction vectors are obtained in the same nodes of the cell boundary domain for both cases.

4.4.3. Effect of cell properties onto the traction force solution

To study the effect of cell properties for computing cell traction forces, two new cases are presented where we vary the mechanical properties of the cell domain. In the first scenario, the shear modulus of the cell domain was increased from the original values (84 Pa) to 168 Pa. In the second scenario, cell's shear modulus was doubled to 336Pa. In

this section, the mechanical properties of the collagen gel remain unchanged. In the following these two cases are referred as *Cell* + gel* and *Cell** + gel* case. The input displacement field was common for both cases and corresponds to those shown in Figure 4.6. The resulting traction vectors obtained in both cases are presented in Figure 4.8.

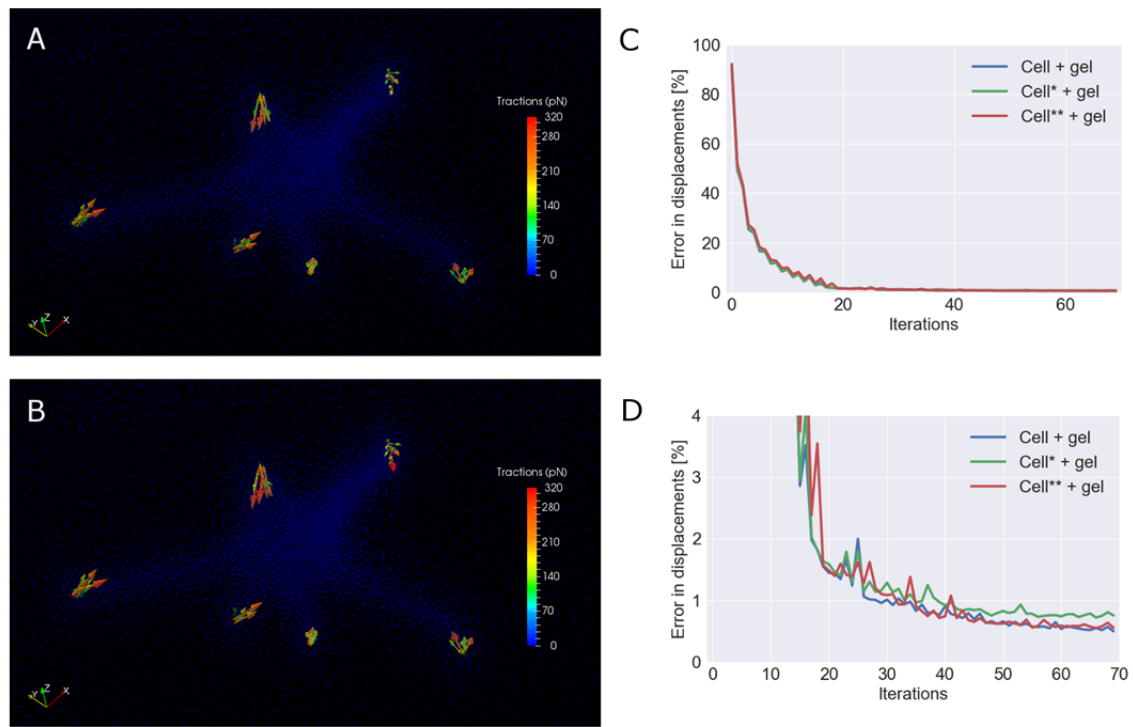


Figure 4.8: Effect of cell mechanical properties on traction maps reconstruction through the inverse algorithm.

The magnitude of the tractions for: A) *Cell* + gel* case, the shear modulus is set to 168 Pa for the cell domain and 40 Pa for the gel domain, both are considered incompressible materials. B) *Cell** + gel* case, the shear modulus is set to 336 Pa for the cell domain and 40 Pa for the gel domain, both are considered incompressible materials. C) Percentage of error at each iteration for *Cell + gel*, *Cell* + gel* and *Cell** + gel* cases. D) Detail of the convergence curve for *Cell + gel*, *Cell* + gel* and *Cell** + gel* cases.

As expected, the maximum values of the computed tractions are recovered in the same cell-matrix interface nodes as in the previous cases and point to the cell center in all cell protrusions. However, in these two new cases, the traction values are slightly increased compared to the traction values obtained in the *Cell + gel* case (286 pN for *Cell* + gel* case and 310 pN for the *Cell** + gel* case, see Figure 4.8A-B). This is a direct consequence of the increase in the mechanical properties of the cell domain.

In the *Cell* + gel* case, the convergence of the algorithm was reached after 35 iterations and the error obtained in the computed displacement field is equal to 0.96%. In contrast, for *Cell** + gel* case, where cell mechanical properties values were doubled from the *Cell* + gel* case, the convergence was achieved after 32 iterations with an error in the resulted displacement field of 0.93% (see Figure 4.8C-D). In spite of both cases have taken a similar number of iterations to reach convergence, both have taken almost twice the number of iterations compared to the *Cell + gel* case.

In summary, the results obtained from computations shown similarities in the convergence and error values for both cases while, at the same time are not far away from tractions results obtained in the *Cell + gel* case (see Figure 4.7 and Figure 4.8). Thus, these data indicate how the mechanical properties of both domains are important for arriving to the correct results when using inverse traction force reconstruction algorithms, however, have only a minor effect on the resulted traction values.

4.5. Discussion

In this chapter, a new methodology for computing cell traction forces is presented. To this end, a numerical model for solving cell traction forces on non-linear materials based on a recursive algorithm in the absence of regularization is presented. To illustrate the proposed recursive method, it is applied to a human dermal fibroblast cells (NHDF) migrating inside a 2 mg/ml collagen-based gels.

To reconstruct the cell geometries, LCSM imaging of individual cells inside the microfluidic-based devices presented in chapter 3 was used. Subsequently, the so-obtained z-slices are segmentated to generate single 3-D models of the cell and gel geometries. These real geometries are then meshed and used to generate the FE model of the cell and the gel matrix that is then used in the different numerical simulations.

To perform the simulations, a non-linear behavior was selected for both cell and hydrogel domains. Notwithstanding that only non-linear materials have been used to solve traction forces in the numerical examples here presented, it is possible to implement any type of material model, linear or non-linear, to solve cell traction forces.

With the results generated from computations it is demonstrated the application of the algorithm and it is explored the effect of the mechanical properties of both cell cytoskeleton and hydrogel domains, onto the cell traction force solution. The force reconstruction algorithm converges after a relatively small number of iterations, generating errors lower than 1% for the displacements field in the entire gel domain and errors of 5% for the tractions field in the cell contour domain.

Through the different cases proposed, we determined that the precise knowledge of the mechanical properties of both domains improve the quality of the predictions; however we are aware of the difficulty to determine the exact mechanical properties of the cell domain. The results obtained from computations shown similarities in the convergence and error values for the different cases. Thus, these data indicate how the mechanical properties of both domains are important for arriving to the correct results when using inverse traction force reconstruction algorithms, however, have only a minor effect on the resulted traction values.

A key advantage of the new approach is that it allows the computation of cell traction forces for any type of material (with a linear and non-linear behavior). Moreover, in contrast to previously published approaches no regularization is needed for solving cell traction forces. However, it should be noted that in this work only *in silico* displacement data were used for calculating cell traction forces and it is possible that in the presence of noise, a regularization parameter need to be introduced.

Another advantage of this method is that can be easily implemented in any type of FE software and can be extended to any type of contractile cell. Regarding the experimental setup, no cell fixation is needed to perform the confocal imaging of cells and ensures cell viability and cells are fully embedded on a 3-D fibrillar network, then allowing the study of *in vitro* 3-D cell-specific changes over time. Thus, this methodology will enable to study the effect of more complex cell substructures *in vitro*, such as the mechanical properties of the cell nucleus or other cellular organelles, onto the traction forces exerted by cells during cell migration or tissue invasion.

However, the method relies on the knowledge of the cell geometry or the cell boundary, which in the future would be ideal to extend to an unconstrained methodology.

Chapter 5

EFFECT OF CELL MECHANICAL PROPERTIES ON TRACTION FORCES

In this chapter it is investigated how steric effects affect cell contractile forces during cancer cell invasion without altering the mechanical properties of the ECM. To this end, it is investigated how cells respond to changes in steric hindrance that arise from altered cell mechanical properties. To that end, we measure traction forces, morphology and invasiveness of MDA-MB 231 breast cancer cells in 1.2 mg/ml three-dimensional collagen-based gels, by studying two different cases in which breast cancer cells present altered cell mechanical properties. First, the different methodologies used are presented and finally the results of the different experiments are discussed. This work is the result of a PhD stay in the Center for Medical Physics and Technology of Erlangen, led by the professor Ben Fabry⁸.

⁸ Part of this research has been published in: M. Córdor, J. Steinwachs, C. Mark, J.M. García-Aznar and B. Fabry. *Traction Force Microscopy in 3-Dimensional Extracellular Matrix Networks*. Current protocols in cell biology, 2017. The main insights and results of this research will be published in: M. Córdor, C. Mark, R. Gerum, J.M. García-Aznar and B. Fabry. *Breast cancer cells adapt contractile forces to overcome steric hindrance*. 2018 (in preparation).

5.1. Introduction

Most cells that are able to adhere, spread and migrate on a 2-D extracellular matrix can also adhere, change shape and migrate when embedded in a biopolymer network of suitable adhesiveness, stiffness, and network porosity. However, when cells migrate through a 3-D matrix, they must overcome not only the adhesion forces as in a 2-D environment, but also the resisting forces imposed by the surrounding matrix [9, 11]. Resisting forces mainly arise from steric effects. This steric hindrance in turn depends on the matrix properties (pore size and fiber stiffness [9, 12-14, 230]) as well as cell properties (cell size and cell stiffness, [13, 15-18, 231]). Studying cell-generated forces as the cells migrate through an extracellular matrix with varying degrees of steric hindrance is important for a mechanistic understanding of numerous physiological and pathophysiological cell functions in health and disease that involve cell adhesion, shape changes and migration, such as tissue formation during embryogenesis, tumor metastasis formation, or the homing of immune cells. Moreover, quantifying these forces is important for understanding the function of highly contractile cells, such as cardiomyocytes or fibroblasts.

To investigate cell migration under varying degrees of steric hindrance, previous studies have changed the protein concentration of a 3-dimensional biopolymer network [9, 12], the pore size [13, 232] or the network fiber stiffness [12]. These studies have consistently found a decreased cell migration or invasion with increasing steric hindrance of the matrix. What is unknown, however, is whether cells can partially compensate for this increase steric hindrance, either by an increased generation of traction forces or by changes in force polarity, which both have been previously shown to be essential for 3-D cell migration [120].

Although it is possible to measure cell-generated forces in a 3-D biopolymer network, it is problematic to compare measurements from gels with different protein concentrations and hence pore size and fiber stiffness, as this can drastically change the non-linear behavior of the matrix [115]. Moreover, an altered matrix protein concentration inevitably leads to altered adhesive ligand density [9]. An alternative way to modulate steric hindrance is to stiffen the biopolymer fibers with low doses of

glutaraldehyde [12], but this in turn lowers the proteolytic degradability of the matrix and may lead to changes in cell migration that are unrelated to effects of steric hindrance.

In this study, we therefore follow an alternative approach: instead of changing the extracellular matrix properties, we altered the cell mechanical properties. To do so, we either increased the nuclear stiffness of breast cancer cells by overexpression with the nuclear protein lamin A [19], or we introduced into the cells polystyrene beads with a diameter larger than the average pore size of the extracellular matrix. Although both interventions may also cause secondary cellular responses that are difficult to predict, we argue that the ability to measure cell-generated traction forces and migration behavior under identical matrix conditions compensates for the potential disadvantages.

Overall, we found that increasing the steric hindrance by stiffening the nuclear lamina caused an appreciable decrease in the percentage of invasive cells but less so in invasion speed, which was accompanied by an increase in force polarity but not traction force magnitude. By contrast, the migration of cells carrying polystyrene beads with a diameter larger than the average pore size of the 3-D matrix was dramatically impeded, and these cells increased their traction forces compared to control cells. Together, our data demonstrate that breast cancer cells are capable to adapt their traction forces and force polarity to the steric hindrance imposed by the surrounding matrix.

5.2. Material and Methods

In this section are described the main methods used in this chapter for studying the effect of increasing the steric effects imposed by the matrix on traction forces exerted by MDA-MB 231 cells during migration. To that end, not only experimental assays but also computational procedures used for quantifying the obtained experimental data are described.

5.2.1. Cell culture

MDA-MB 231 breast cancer cells (obtained from ATCC) were kept in 75cm² cell culture flasks with low glucose (1g/L) Dulbecco's modified Eagle's medium (DMEM, Biochrom)

supplemented with 10% fetal calf serum (FCS, Greiner) and 1% penicillin and streptomycin at 37°C, 5% CO₂ and 95% humidity. For lamin A transfected cells, 1 µg/ml puromycin is added to the medium. Cells were passaged every 2nd day using 0.05% trypsin/EDTA.

5.2.2. MBA-MD 231 Lam-A lentiviral transduction

For generating MDA-MB 231 cells expressing enhanced green fluorescent protein (eGFP)-lamin A, lentiviral transduction is used as described in [232]. In brief, HEK293T cells are co-transfected with the vectors pMD2.G, psPAX2 and pLVX containing the coding sequence of lamin A N-terminally fused to eGFP using Lipofectamine LTX (Invitrogen). The cell culture supernatant is collected daily and replaced with fresh DMEM medium for the next 4 days. The collected medium containing assembled virus particles is pooled and filtered through 0.45 µm pores, supplemented with 8 mg/ml polybrene and added to MDA-MD 231 cells for 18h. Starting from day 2 after lentiviral infection, cells are selected using 1 µg/ml puromycin.

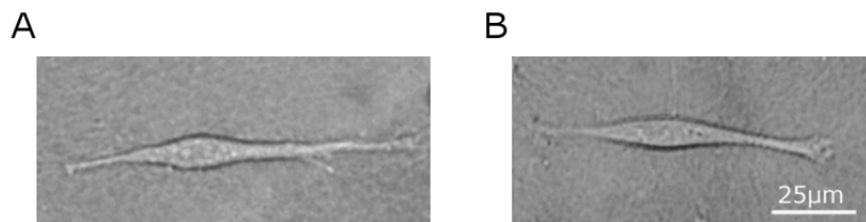


Figure 5.1: Representative cells invading a 1.2 mg/ml collagen gel. Brightfield imaging of a: A) MDA-MD-231 cell, B) MDA-MD-231 cell with lamin A overexpressed.

Immunoblot analysis showed different indigenous eGFP-lamin A levels for MDA-MB 231 [232]. Following transduction, expression of eGFP-lamin A is detectable in 95% of cells, and total average lamin A levels are approximately triple the endogenous lamin A levels. Wildtype cells (MDA-MB 231) and cells transduced with eGFP-lamin A show similar morphology during invasion in a soft collagen gel (Figure 5.1).

5.2.3. Internalization of latex beads

For increasing the steric effects imposed by the matrix, cells are loaded with non-degradable polystyrene beads that are larger than the average pore size of 3.8 μm for a 1.2 mg/ml collagen gel [12, 232]. Approximately 2×10^5 5- μm diameter carboxylated beads (Thermo Fisher) are sonicated, added to a 35mm cell culture dish and incubated overnight. Previous reports have shown that already after 30 minutes of bead incubation, approximately 70% of beads are internalized by MDA-MB 231 cells [233-235]. On the next day, cells are rinsed twice to remove unbound beads, harvested with 0.5% trypsin/EDTA, mixed with collagen and cultured for another 12 h before traction measurements, or for 3 days for performing invasion assays, as described above. 90% of all cells in the collagen gels carried between 1 and 3 beads. For traction force and invasion assay analysis, we selected only cells carrying exactly one bead.

5.2.4. Bead internalization analysis with tdTomato-farnesyl live cell membrane staining

Fluorescent imaging of cells expressing td-Tomato-farnesyl was performed to check whether the beads were internalized or not by the cells. MDA-MD 231 cells were transfected with (Lipofectamine 2000, Life Technologies) with the appropriate constructs, according to manufacturer's instructions [236]. Subsequently cells (0.5×10^5) were seeded on Fibronectin-coated coverslips (22x22mm) and incubated overnight. After that, cells were mounted using complete cell culture medium (DMEM, Biochrom) before fluorescence imaging.

To analyze the cell bead internalization, image z-stacks over the cell depth were taken with a z-distance of 0.5 μm , using a motorized Leica 6000 Inverse fluorescence microscope with a 63 x 1.40NA oil immersion objective (see Figure 5.2).

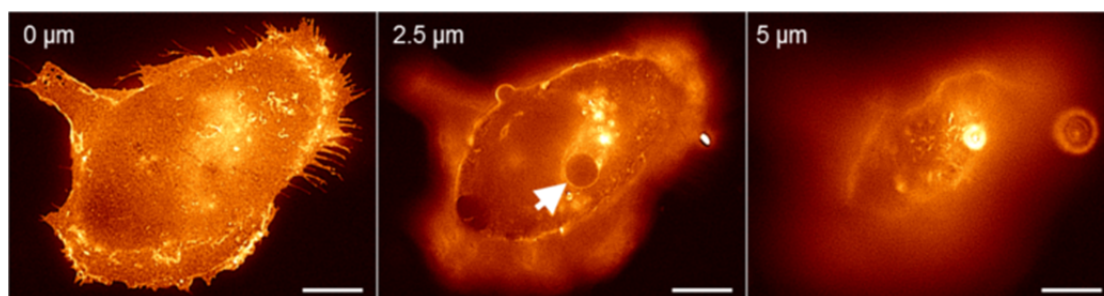


Figure 5.2: Live cell membrane staining with td-Tomato-farnesyl. Fluorescence imaging of different z-sections of a MDA-MD 231 cell with an internalized polystyrene bead (arrow). Scale bar is 10 μm .

5.2.5. Preparation of 3-D collagen hydrogels

To prepare 1.2 mg/ml collagen type I hydrogels, we mix 1.2 ml of rat tail collagen (Collagen R, 2mg/ml, Matrix Bioscience), 1.2 ml Bovine skin collagen (Collagen G, 4mg/ml, Matrix Bioscience), 270 μl NaHCO_3 (23mg/ml), 270 μl 10x DMEM (Biochrom) and 43 μl of NaOH (1M) to adjust the pH to 10. The solution is then diluted with 3 ml of a mixture of 1 volume part of NaHCO_3 (23mg/ml), 1 part of 10x DMEM and 8 parts of distilled H_2O . All ingredients were kept on ice during the preparation process. 2 ml of the final collagen solution was pipetted in a 35mm Petri dish and polymerized in a tissue culture incubator at 37°C, 95% relative humidity and 5% CO_2 for 1 hour. After polymerization, 2 ml of complete cell culture medium was added to prevent dehydration of collagen gels. For more information about the critical parameters and troubleshooting for generating collagen gels, see [223].

5.2.6. Collagen gel mechanical characterization

To quantify the traction force-induced deformations of the biopolymer network during cell migration, it is necessary to know the mechanical properties of the matrix. Based on the Steinwachs et al. [115] work, we assumed that the collagen gels deforms in a non-affine and non-linear way. This behavior can be described with 4 parameters: a linear elastic stiffness K_0 , a strain range L_s at which the matrix starts to stiffen, a strain scale d_s describing the exponential stiffening under stretch, and a strain scale d_0 describing the

exponential softening under compression. To measure these 4 parameters, two different macrorheological experiments were performed. The first experiment, the stress versus strain relationship of the matrix for simple shear deformation is measured in a cone-plate rheometer (see Figure 5.3A). In the second experiment, the vertical contraction of the matrix under horizontal uniaxial stretch is measured (see Fig. 7B). For more information about these experiments, see Supplementary notes in [115].

The four material parameters used in this work to describe the behavior of the 1.2 mg/ml collagen gels were estimated as: $K_0=1645$, $d_0=0.00032$, $L_s=0.0075$ and $ds=0.033$. To estimate them, the data from the macrorheological measurements (stress versus strain, and vertical contraction versus horizontal stretch) are compared to the calculated response of the four parameters until minimize the mismatch between experimental data and computational predictions [115]. Figure 5.3 shows the model predictions (blue lines) compared with data from two different rheological experiments (red lines).

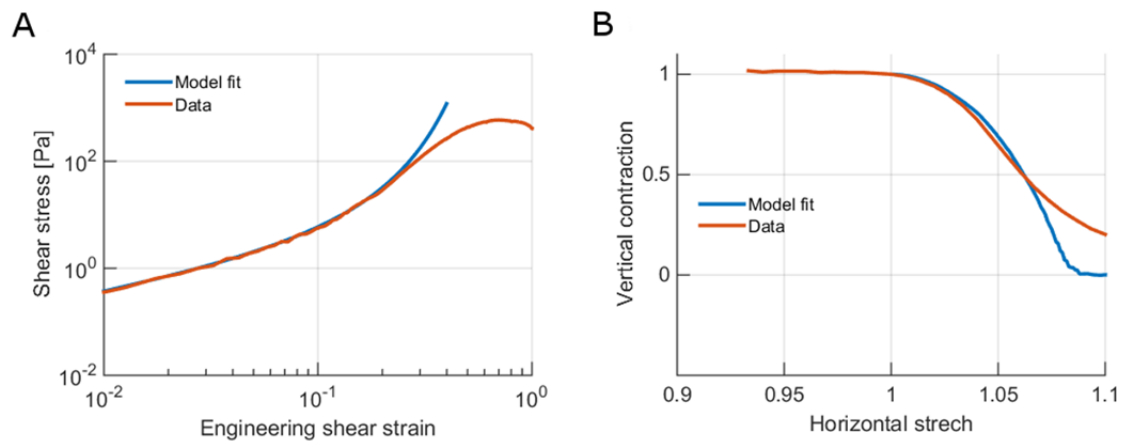


Figure 5.3: 1.2 mg/ml collagen gel characterization.

A) Material stress as a function of the engineering shear strain predicted by the semi-affine model (blue), and the corresponding data measured with a cone-plate rheometer (red), B) Vertical contraction as a function of the horizontal stretch predicted by the semi-affine model (blue), and the corresponding data measured in a uniaxial stretch experiment (red). The experimental data correspond to the response of two different 1.2 mg/ml collagen gels.

5.2.7. Invasion assay in a 3-D collagen gel

50000 cells are seeded on top of 1 mm thick 1.2 mg/ml collagen gels and allowed to invade for 3 days. After 3 days, cells are fixed for 30 min with 2 ml of 2.5% glutaraldehyde in PBS, and cell nuclei are stained for 20 min with 1 µg/ml Hoechst 33342 (Sigma). To analyze the cell invasion profile, z-stacks with a z-distance of 2 µm were imaged with a motorized fluorescence microscope (Leica) using a 20x 0.4 NA objective. The z-position of cell nuclei (see Figure 5.4) are determined for 36 fields of view, each corresponding to a volume of 430µm x 330µm x 500µm (x, y, z). For each condition, at least 3 independent experiments are performed. In the case of cells with beads, only cells that contain at least one bead are included in the data analysis.

The invasion profile is plotted as a cumulative probability of finding a cell at or below a given depth of the gel, and is fitted with a superposition of two exponential functions, representing the invasion behavior of two subpopulations:

$$P_{cum}(z) = f_{invaded} \exp\left(\frac{-z}{d_1}\right) + (1 - f_{invaded}) \exp\left(\frac{-z}{d_2}\right) \quad (5.1)$$

The parameter d_1 describes the characteristic invasion depth of the invasive cell fraction $f_{invaded}$, and d_2 describes the z-distribution of the non-invasive cell fraction $(1 - f_{invaded})$ near the collagen gel surface. To account for the invasion front, the second exponential function was truncated at a maximum invasion depth z_{max} .

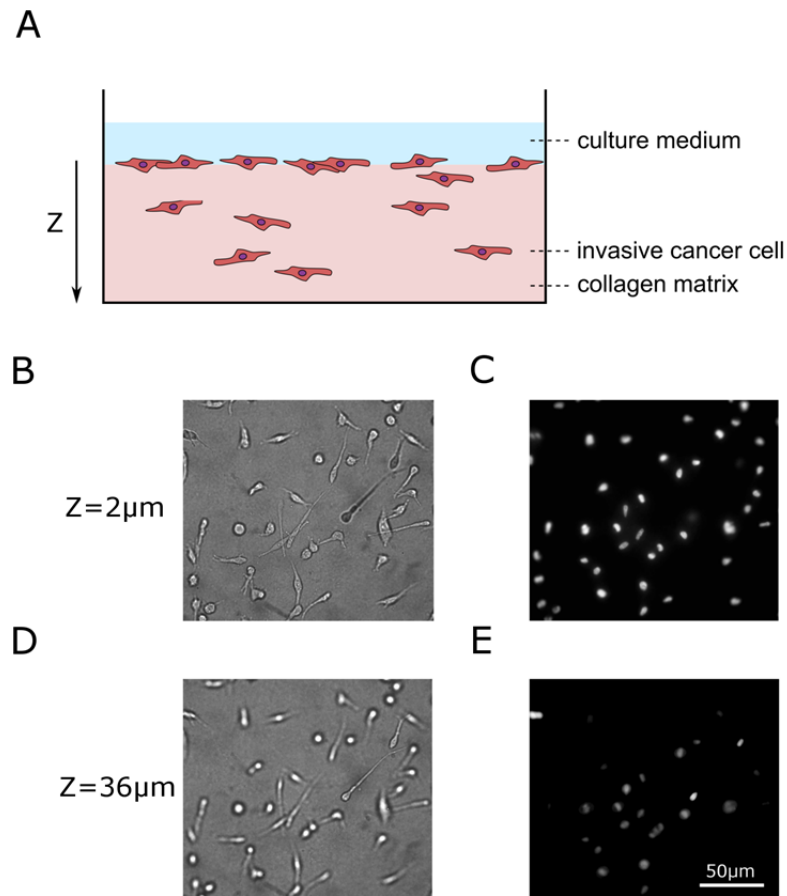


Figure 5.4: Cell invasion assays.

A) Schematic of the cancer cell invasion assay. B-C) Bright field image and D-E) fluorescent image of stained nucleus with Hoechst 33342 of MDA-MD-231 cells migrating within a 1.2 mg/ml collagen gel, for different z planes.

5.2.8. 3-D Traction force microscopy assay

15000 cells are mixed with 1 ml unpolymerized collagen solution and incubated for 12 h before experiments. To compute the traction force-induced deformations of the biopolymer network, the collagen fibers are imaged with confocal reflection microscopy using a 20x dip-in water-immersion objective with NA 1.0. One image stack is recorded before cell traction forces are relaxed with cytochalasin-D, and a second image stack is recorded 30 min after cytochalasin-D addition (see Figure 5.5). The first image stack represents the deformed state, whereas the second image stack represents the undeformed force-free configuration of the matrix.

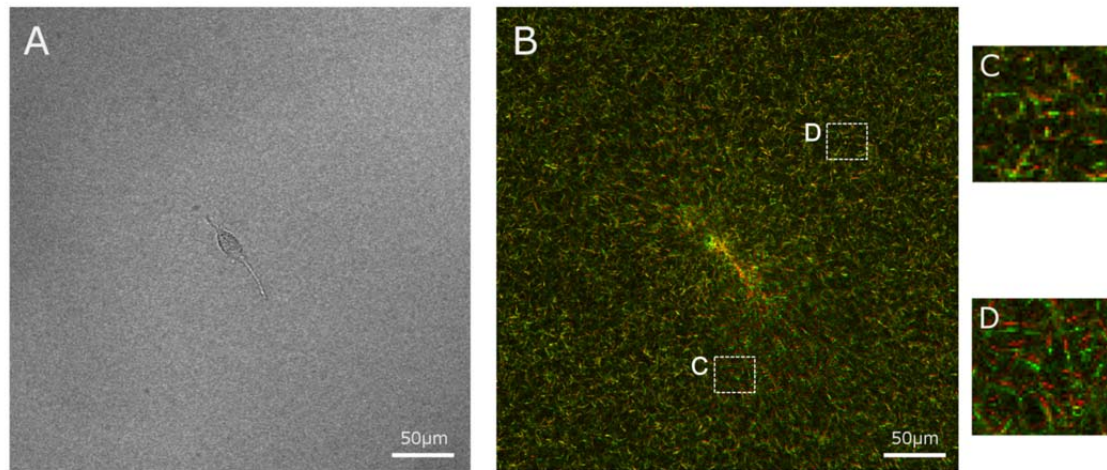


Figure 5.5: Cell traction force reconstruction.

A) Bright field image of a MDA-MD-231 breast carcinoma cell migrating within the collagen gel. B) Overlay of confocal reflection images of collagen fibers before (red) and after (green) cell relaxation with Cytochalasin-D. Enlarged section of two regions of the overlaid image with C) small and D) large deformations due to cell forces.

5.2.9. Unconstrained traction force reconstruction

To compute the traction force-induced deformations of the biopolymer network was used the approach described in [115]. The input data for the algorithm are the two image stacks (deformed and undeformed state) as well as the 4 parameters that describe the material properties of the collagen network (K_0 , d_0 , L_s and d_s). The software first computes the displacement field of the collagen network between the deformed and the undeformed image stack. To do so, both image stacks are aligned to remove stage drift and z-focus drift. The alignment algorithm used is based on rigid registration. Once the images are aligned, the program computes the matrix displacement field with particle image velocimetry. Second, the software performs an unconstrained force reconstruction algorithm to calculate the cell traction forces. To this end, the matrix volume is tessellated and subdivided into a mesh of small finite elements of tetrahedral shape. For each tetrahedron, the constitutive equation that describes the relationship between the forces at the 4 nodes of the tetrahedron and the stresses and deformations of the 4 faces are computed numerically. An iterative method is then used to modify the nodal forces of all finite elements until the measured and calculated matrix displacements match. For more information about the unconstrained force

reconstruction method, see Supplementary notes in [115] and a recent published protocol [223].

5.2.10. Cell shape analysis

Cell aspect ratio was computed from maximum intensity projections of bright field image stacks. From the image projection, we calculate the aspect ratio as the distance between the two points of the cell outline with the largest separation (major axis length), divided by the largest cell dimension found anywhere perpendicular to the long axis (minor axis length).

5.2.11. Statistical analysis

Results were obtained from at least three independent experiments. Differences between measurements were considered statistically significant at $p \leq 0.05$ by a Student's two-tailed-t-test (comparing two groups) assuming unequal variances including the outliers. Throughout the chapter, * denotes $P \leq 0.05$, ** denotes $P \leq 0.01$, and *** denotes ≤ 0.001 .

5.3. Results

In this section the results obtained of the different experiments are presented and it is divided in four main parts. The first one summarizes the results from the invasion assays for the 3 different groups of study and shows the effect of increasing cell stiffness on cell invasion. The second part shows the traction force analysis for the 3 groups of study. Subsequently, the strain energy and matrix stiffening is evaluated under different degrees of steric hindrance. And finally, the effect of steric hindrance on cell morphology is investigated.

5.3.1. Effect of cell stiffness on cell invasion

We hypothesized that cells with higher cell stiffness experience more steric hindrance when migrating through confining matrix pores. To test this, we modulated the stiffness of MDA-MB 231 breast cancer cells through two different approaches. The first approach relies on overexpression of the nuclear protein lamin A using lentiviral

transduction, which leads to an increase in lamin A expression levels of 200% and causes an increase in overall cell stiffness by 47% [16, 19, 232]. This increase in cell stiffness after lamin A overexpression was estimated from the increase of transit time when the cells are flushed through 5- μm microconstrictions, which is slightly larger than the average pore size in our collagen gels (3.8 μm [237]).

In a second approach, we increase the apparent cell rigidity by binding or internalizing non-degradable 5- μm polystyrene beads to the cells. Polystyrene beads have been previously used to study remodeling processes of the cytoskeleton by tracking their spontaneous motion [233-235]. MDA-MB 231 breast cancer cells readily internalize these beads. After 30 minutes of bead incubation, approximately 70% of beads are internalized by the cells [235]. To increase the fraction of internalized beads further, we incubate the cells with beads overnight. Fluorescent imaging of cells expressing tandem tomato-farnesyl for labeling membranes was performed to confirm that the beads are internalized (see Figure 5.2).

To measure invasive behavior, cells are seeded on top of 1 mm thick 1.2mg/ml collagen gels. After an incubation time of 3 days, cell invasion into the gels is quantified by optical sectioning to determine the z-position of the cell nuclei stained with Hoechst 33342 (Figure 5.4A-E). The cell density as a function of the invasion depth was determined in 36 fields of view of three independent gels for each cell group. From the z-position of each nucleus, we compute the invasion profile, which is expressed as the cumulative probability $P_{cum}(z)$ of finding a cell at or below a given invasion depth z . The invasion profile is fitted with a superposition of two exponential functions, yielding the fraction of invaded cells as well as the characteristic invasion depth (Figure 5.6A-C).

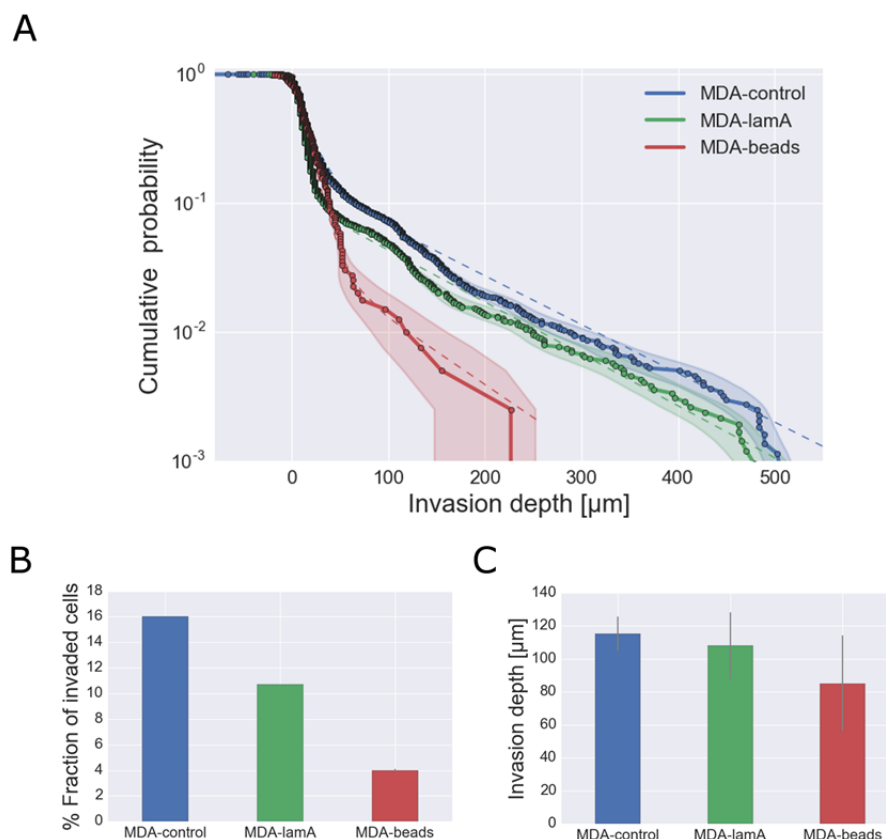


Figure 5.6: Results of invasion assays.

A) Invasion profiles (cumulative probability of finding a cell at or below a specified invasion depth) after 3 days. Dashed lines are the fitted curves for each case. B) Fraction of invaded cells and C) characteristic invasion depth obtained with the fitting functions. Control cells (blue), lam-A overexpressing cells (green), cells with 5- μm polystyrene beads (red).

After 3 days of cell invasion, the percentage of invasive MDA-lamA cells was reduced compared to MDA-control but the characteristic invasion depth of the cells that succeeded to invade into the gel was unchanged, as indicated by the similar slope of cumulative probability versus invasion depth in Figure 5.6F. By contrast, both the percentage of MDA-bead that succeeded to invade the collagen gel, and their characteristic invasion depth was strongly decreased (Figure 5.6F).

These data show that by increasing apparent cell stiffness with polystyrene beads, steric effects of the matrix are enhanced, supporting the hypothesis that cell stiffness is inversely correlated with cell invasiveness [232, 238]. However, a less dramatic increase of nuclear stiffness had a surprisingly small effect on cell invasiveness, suggesting that the cells may have responded with counteracting measures.

5.3.2. Adaptation of contractile forces to altered steric hindrance

In this section, is tested if cells can actively counteract steric effects by generating higher contractile forces. Cell of the three groups studied (MDA-control, MDA-lamA and MDA-beads) were mixed with 1.2 mg/ml unpolymerized collagen. After initiating collagen polymerization by increasing the pH and temperature to 37°C, cells were allowed to migrate in the collagen gels for 12 hours. Subsequently, we imaged the cell morphology as well as the collagen network around cells with confocal reflection microscopy before and after cell relaxation with cytochalasin-D (see Figure 5.7). Cellular forces are then computed (Figure 5.7B) from the local displacements field of the collagen matrix (Figure 5.7A) using a non-linear semi-affine finite element 3D force reconstruction algorithm [115].

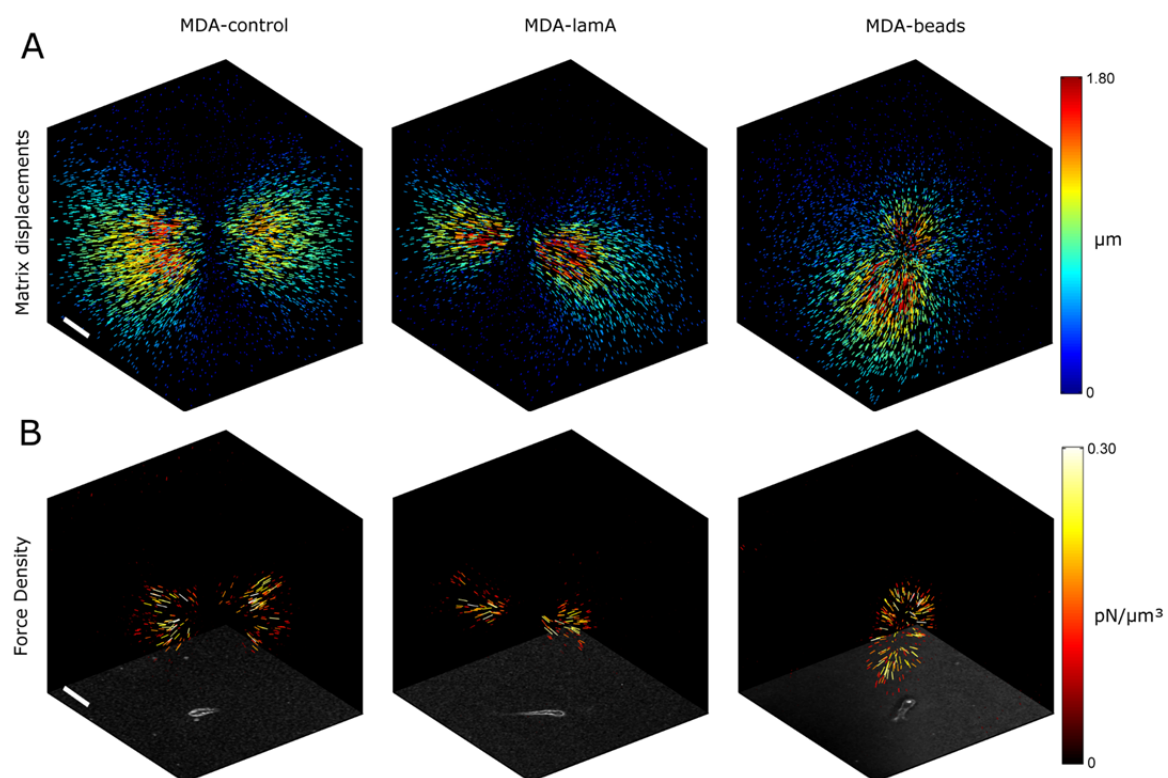


Figure 5.7: Cell traction forces around MDA-MB 231 cells.

A) 3-D matrix displacement field and B) 3-D force density and brightfield z-projection of a MDA-MD-231, a MDA-MD-231 cell with lam-A overexpressed and a MDA-MD-231 cell with a 5- μm polystyrene bead migrating within a 1.2 mg/ml collagen gel. For displacement and force plots, density and color intensity of marks indicate the magnitude of the local displacement vector and local force density respectively. Scale bars in figure correspond to 50 μm .

Force maps of cells from the 3 groups (Figure 5.7) show inward-directed (contractile) forces that are highly polarized, but no obvious differences between the groups are visible (see Figures 5.8-5.13 for a complete set of the experiments).

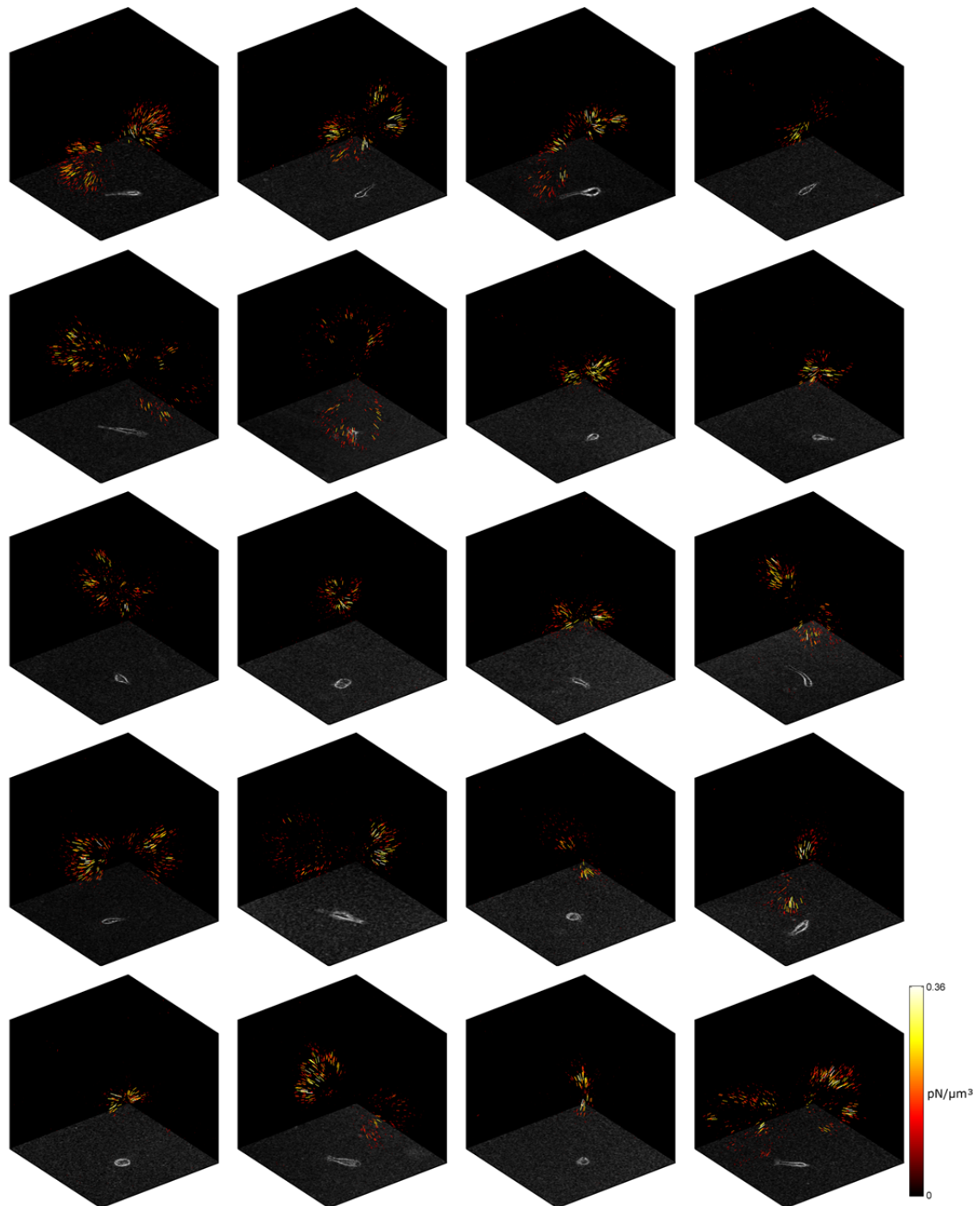


Figure 5.8: 3-D density plots around the MDA-MB 231 breast carcinoma cells included in this study.

The arrow density and color corresponds with the local force magnitude. The total volume displayed is a cubic box with edge length $130\mu\text{m}$. The bottom face of the displayed box shows a brightfield z-projection of each cell analyzed.

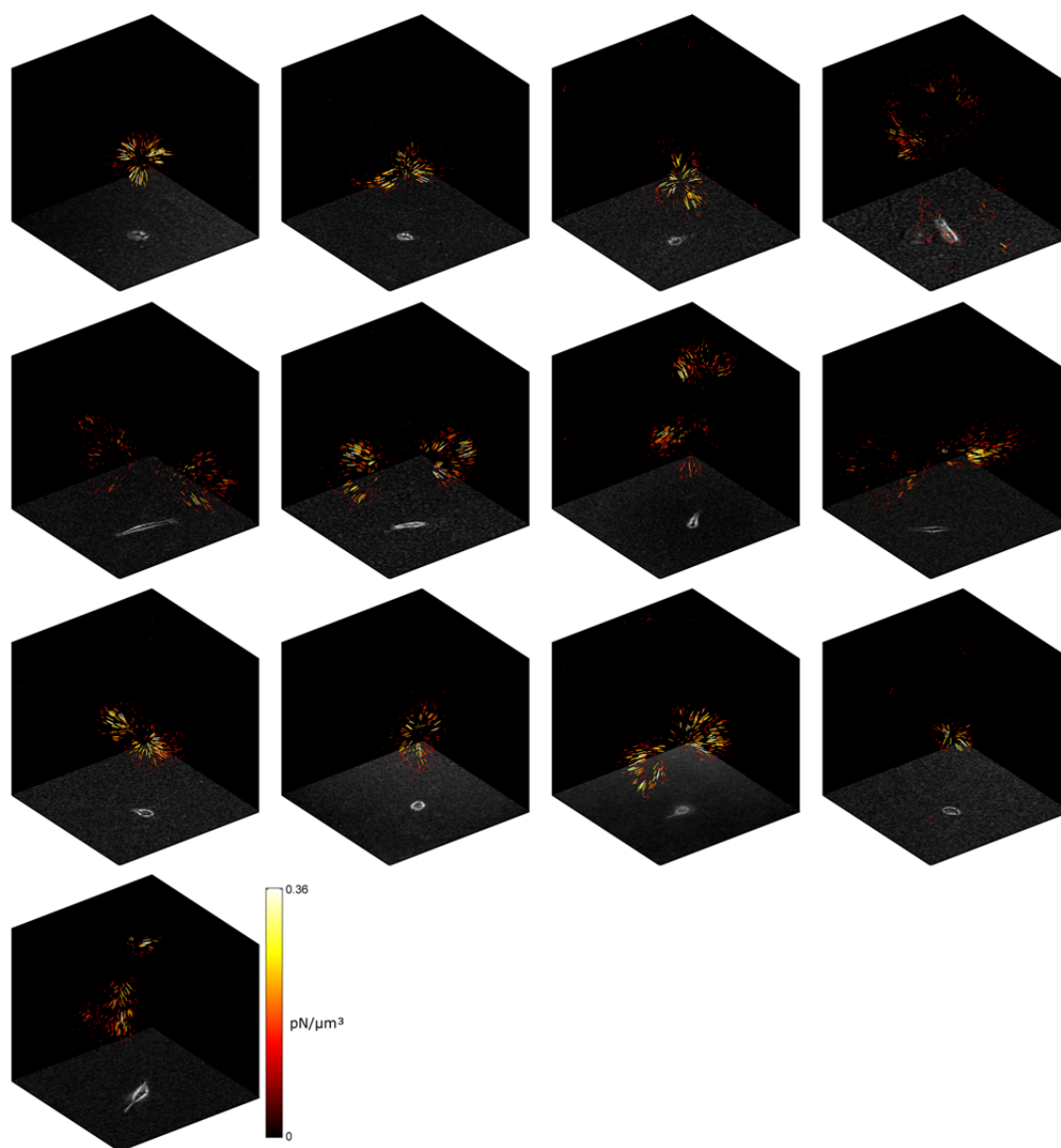


Figure 5.9: 3-D density plots around the MDA-MB 231 breast carcinoma cells included in this study.

The arrow density and color corresponds with the local force magnitude. The total volume displayed is a cubic box with edge length $130\mu\text{m}$. The bottom face of the displayed box shows a brightfield z-projection of each cell analyzed.

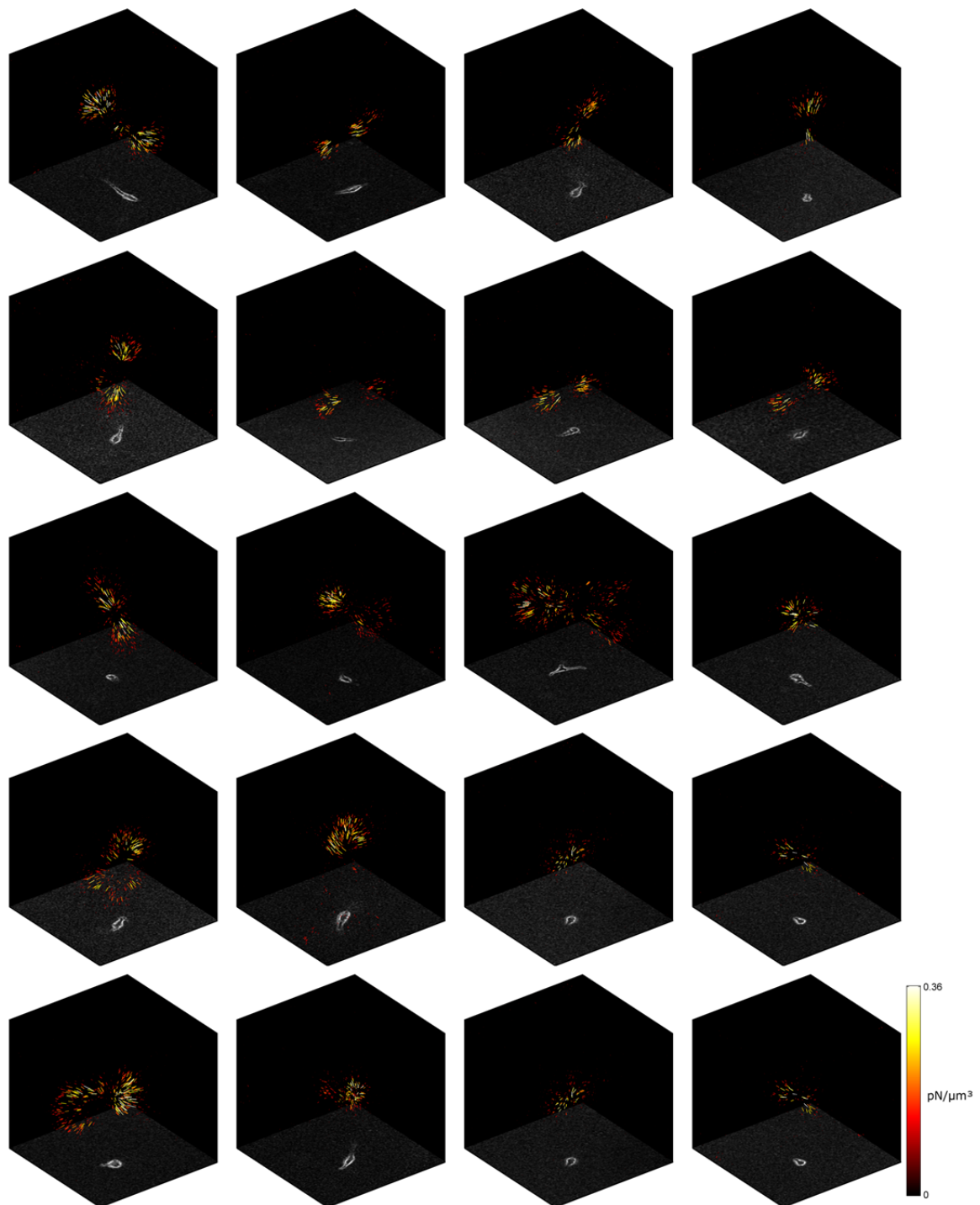


Figure 5.10: 3-D density plots around the MDA-MB 231 breast carcinoma cells with lam-A overexpressed included in this study.

The arrow density and color corresponds with the local force magnitude. The total volume displayed is a cubic box with edge length $130\mu\text{m}$. The bottom face of the displayed box shows a brightfield z-projection of each cell analyzed.

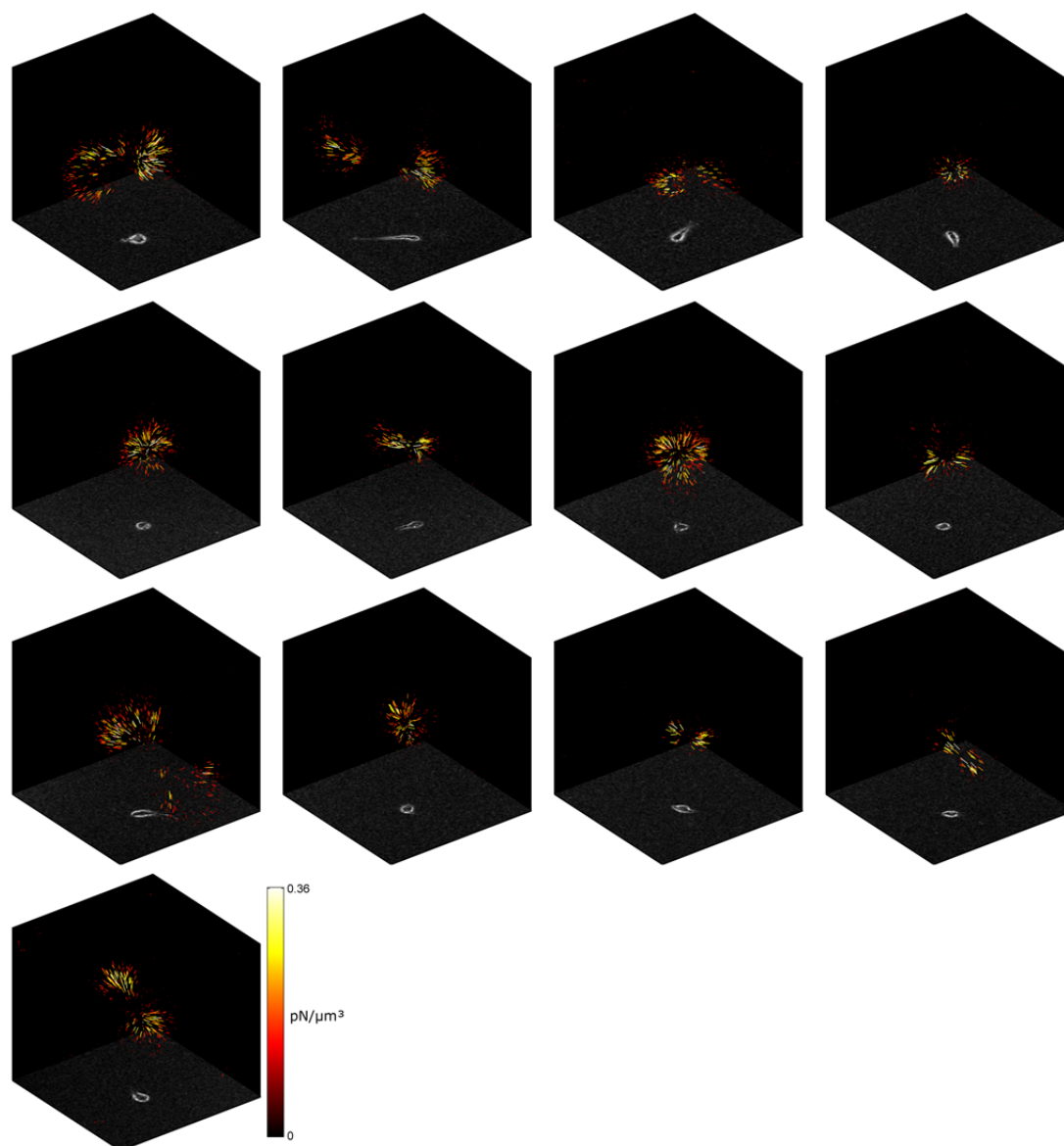


Figure 5.11: 3-D density plots around the MDA-MB 231 breast carcinoma cells with lam-A overexpressed included in this study.

The arrow density and color corresponds with the local force magnitude. The total volume displayed is a cubic box with edge length $130\mu\text{m}$. The bottom face of the displayed box shows a brightfield z-projection of each cell analyzed.

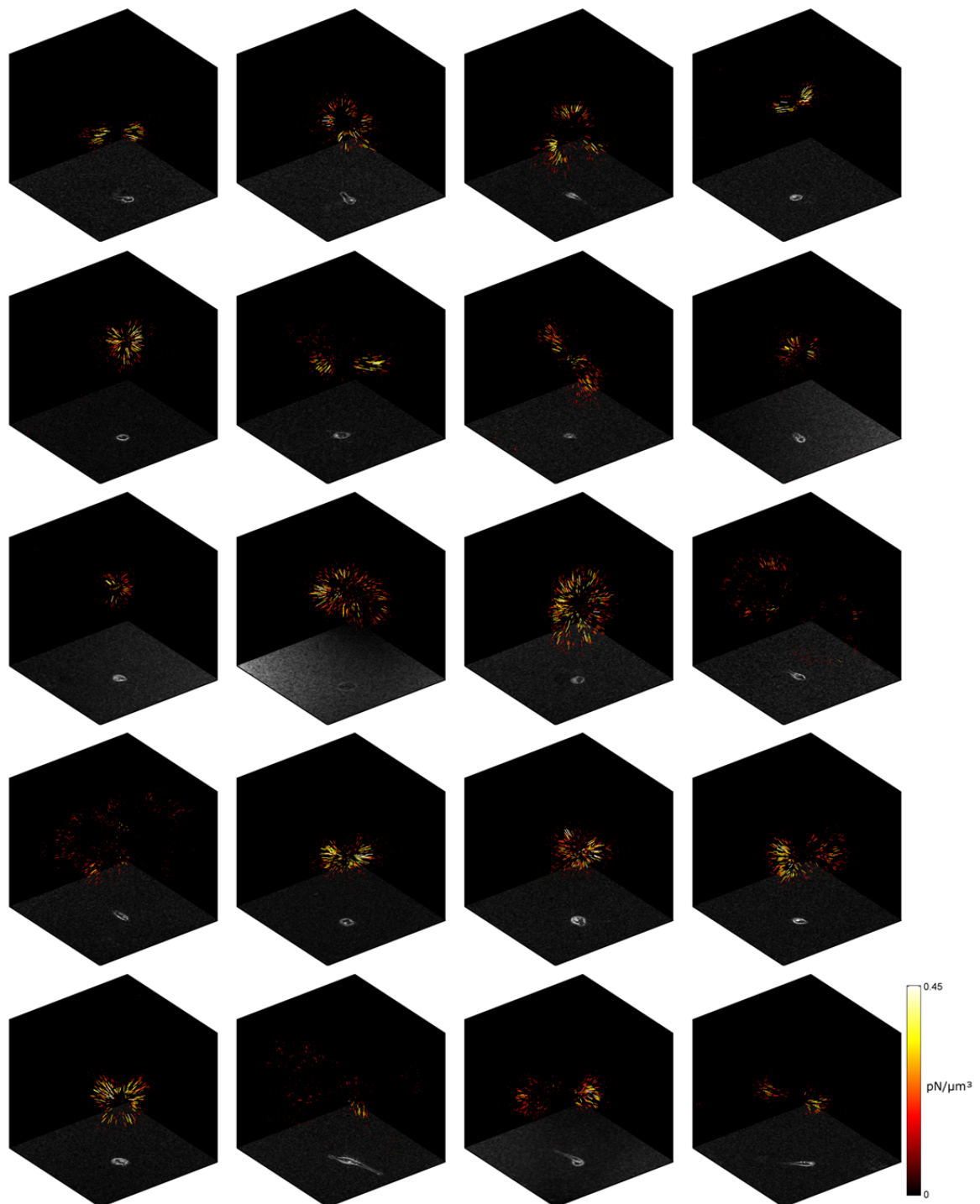


Figure 5.12: 3-D density plots around the MDA-MB 231 breast carcinoma cells with 5- μm polystyrene beads included in this study.

The arrow density and color corresponds with the local force magnitude. The total volume displayed is a cubic box with edge length $130\mu\text{m}$. The bottom face of the displayed box shows a brightfield z-projection of each cell analyzed.

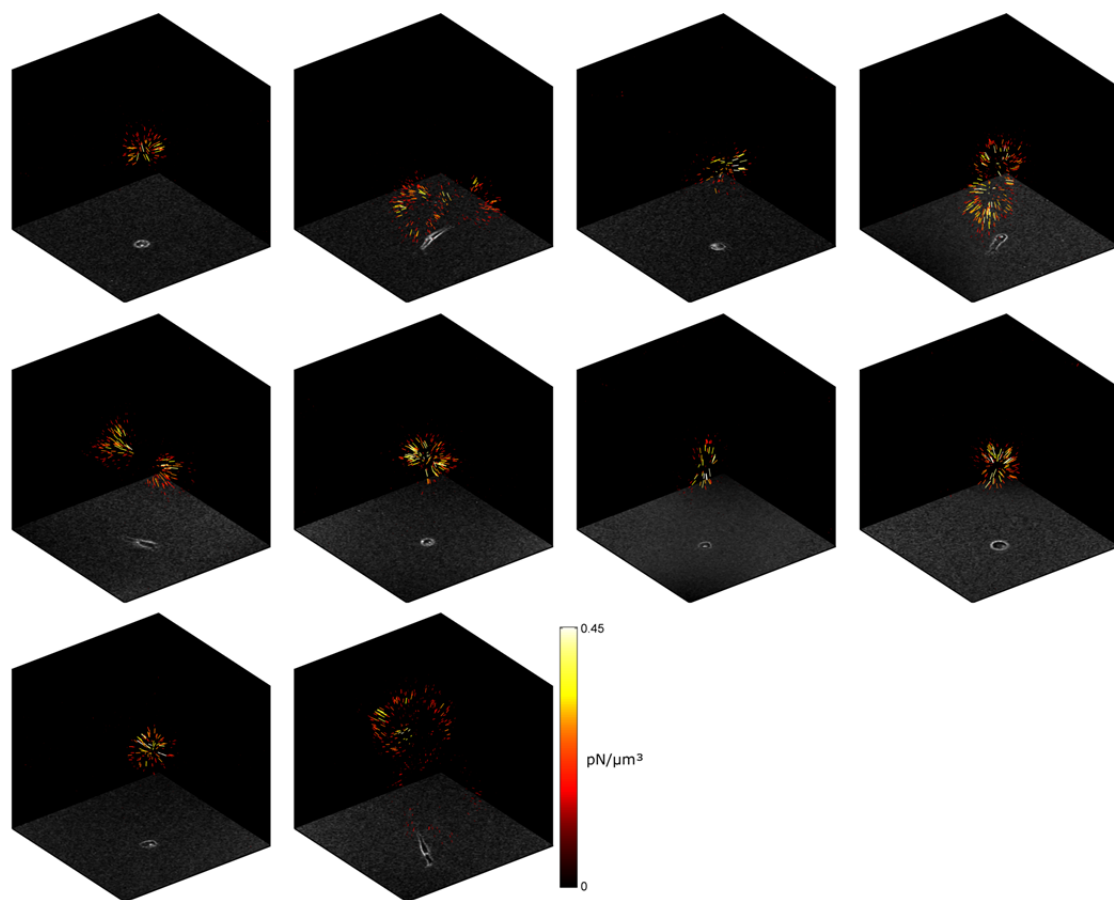


Figure 5.13: 3-D density plots around the MDA-MB 231 breast carcinoma cells with 5- μm polystyrene beads included in this study.

The arrow density and color corresponds with the local force magnitude. The total volume displayed is a cubic box with edge length $130\mu\text{m}$. The bottom face of the displayed box shows a brightfield z-projection of each cell analyzed.

We therefore compute two robust scalar characteristics of the force field - cell contractility and force polarity. Contractility measures the total magnitude of the projected force vectors in the direction of the force epicenter. Polarity is the maximum (principal) dipole contractility divided by the total contractility. Thus, the force polarity quantifies the fraction of the contractile force that is oriented in a single direction. For a force dipole, the force polarity approaches unity, whereas for an isotropic spherical force field, the force polarity approaches $1/3$.

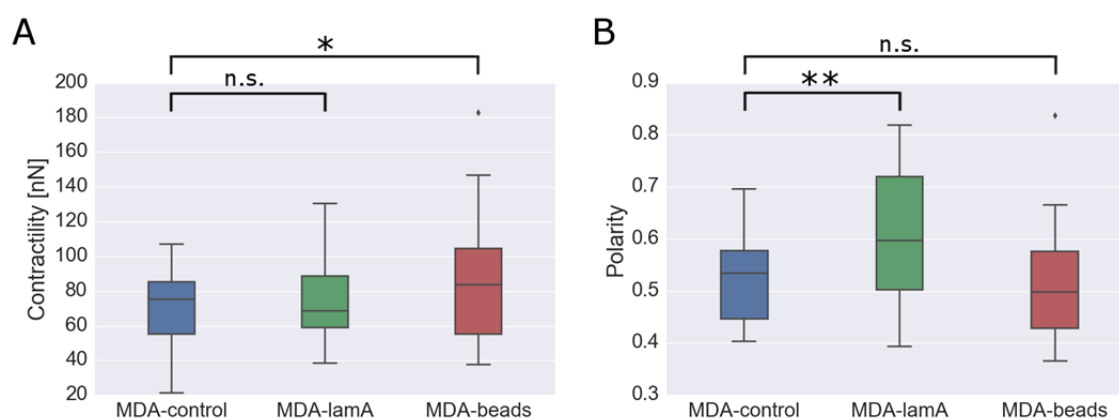


Figure 5.14: Influence of cell rigidity on cell traction forces.

A) Total contractility and B) force polarity of MDA-MB-231 cells (blue, for $n = 33$), MDA-MD-231 cells with lam-A overexpressed (green, for $n = 33$) and MDA-MD-231 cells with 5- μm polystyrene beads (red, for $n = 30$) embedded on 1.2 mg/ml collagen gels. For all box plots the central line indicates the median, the edges of the box denote the first and third quartiles and the whiskers the 5 and 95 percentiles. The outliers are plotted as individual points. * $P \leq 0.05$, ** $P \leq 0.01$, Student's t-test assuming unequal variances including the outliers; n.s., not significant ($P > 0.05$).

Total contractility was similar in MDA-control cells (70.2 ± 3.5 nN, mean \pm se) and MDA-lamA cells (72.1 ± 4.3 nN) but was significantly ($p < 0.05$) increased in MDA-beads cells (85.4 ± 6.2 nN) (Figure 5.14A). By contrast, force polarity was similar in MDA-control cells (0.53 ± 0.01 , mean \pm se) and MDA-bead cells (0.51 ± 0.01) but was significantly ($p < 0.05$) increased in MDA-lamA cells (0.61 ± 0.02) (Figure 5.14B).

Taken together, these findings suggest that there is a regulatory mechanism through which cells are capable to adapt their contractile forces to compensate for steric hindrance alterations of the matrix.

5.3.3. Strain energy and matrix stiffening

We next asked if these compensatory strategies prompt the cells to invest more or less energy for deforming the matrix. This deformation energy is calculated as the total elastic energy stored within in the imaged biopolymer network and released within 30 min after cells are treated with cytochalasin-D. Compared to MDA-control cells, MDA-lamA cells invest a significantly ($p < 0.05$) lower strain energy, while MDA-bead cells invest similar levels of strain energy, despite their higher contractile forces (Figure

5.15D). Although we cannot measure the total energy expenditure of the cells, our finding of an equal or lower strain energy suggests that the generated forces are utilized more efficiently under conditions of higher steric hindrance.

MDA-lamA cells achieve this higher efficiency via a more polarized force generation and hence by reducing “wasteful” forces perpendicular to the migration direction. In the case of MDA-bead cells, which have a similar force polarity but higher total forces compared to control cells, we hypothesized that the lower-than-expected strain energy may be a direct consequence of collagen fiber stiffening under higher forces. Fiber stiffening increases the alignment between collagen fiber orientation and cell-generated forces, and generally allows for a more efficient conversion of tractions to movements. However, fiber stiffening further increases the steric hindrance, thereby potentially canceling any gain in efficiency.

To quantify the effective stiffening of the collagen matrix, we compute the second derivative of the total strain energy in response to an infinitesimal extra deformation of the cell, which gives the apparent matrix stiffness that the cell “feels”. This matrix stiffness is computed under two conditions, first considering the full non-linear collagen behavior, and second considering only the linear and the buckling behavior of the collagen fibers but without any strain stiffening. The strain stiffening value is the ratio of both stiffness values. It quantifies the additional stiffness due to strain stiffening of the matrix.

Also it is computed the local map of strain stiffening of the collagen network around cells. From the strain vector of every node, we compute the matrix stiffness tensor and plot its magnitude averaged over a slice thickness of $\pm 10 \mu\text{m}$ above and below the cell (-Figure 5.15A-C). This value is then normalized by the median stiffness tensor magnitude within the imaged volume to quantify the local strain stiffening of the matrix. Note that the local matrix stiffening is much larger than the effective matrix stiffening that the cell “feels”. This is because stiffened matrix regions transmit cell deformations over large distances towards unstrained and thus softer matrix regions.

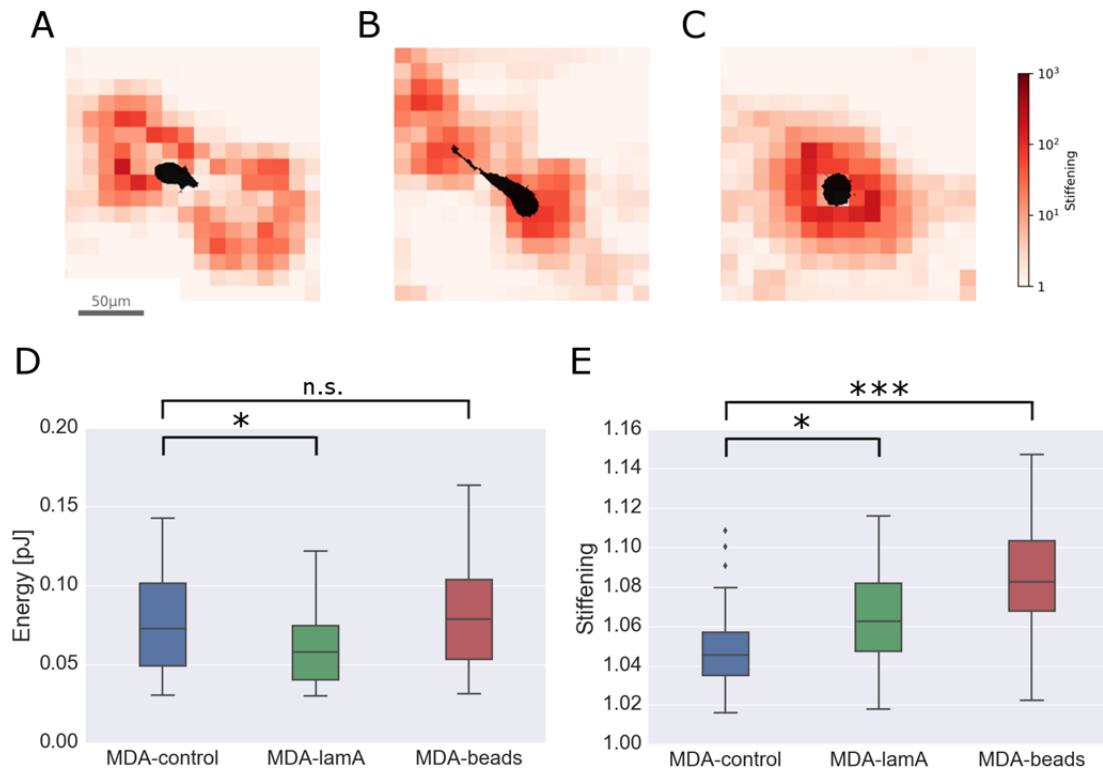


Figure 5.15: Influence of cell contractile forces on the collagen matrix properties. Strain-stiffening maps of the collagen network around an embedded: A) MDA-MB-231 cell, B) MDA-MD-231 cell with lam-A overexpressed and C) MDA-MD-231 cell with a 5-μm polystyrene bead. D) Strain energy and E) matrix strain stiffening of MDA-MB-231 cells (blue, for $n = 33$), MDA-MD-231 cells with lam-A overexpressed (green, for $n = 33$) and MDA-MD-231 cells with 5-μm polystyrene beads (red, for $n = 30$) embedded on 1.2 mg/ml collagen gels. For all box plots the central line indicates the median, the edges of the box denote the first and third quartiles and the whiskers extend to the maximum and minimum value not considered as an outlier. The outliers are plotted as individual points. * $P \leq 0.05$, *** $P \leq 0.001$, Student's t-test assuming unequal variances including the outliers; n.s., not significant ($P > 0.05$).

Moreover, no apparent structural changes can be observed in the collagen matrix for the 3 cases of study (see Figure 5.16). However, in support of our hypothesis, we find a significantly higher stiffening of the collagen matrix around MDA-bead cells compared to control cells (Figure 5.15E). Interestingly, also the matrix around MDA-lamA cells shows some additional stiffening, attributable to the larger principal component force aligned with the major cell axis (see Figure 5.15A-C).

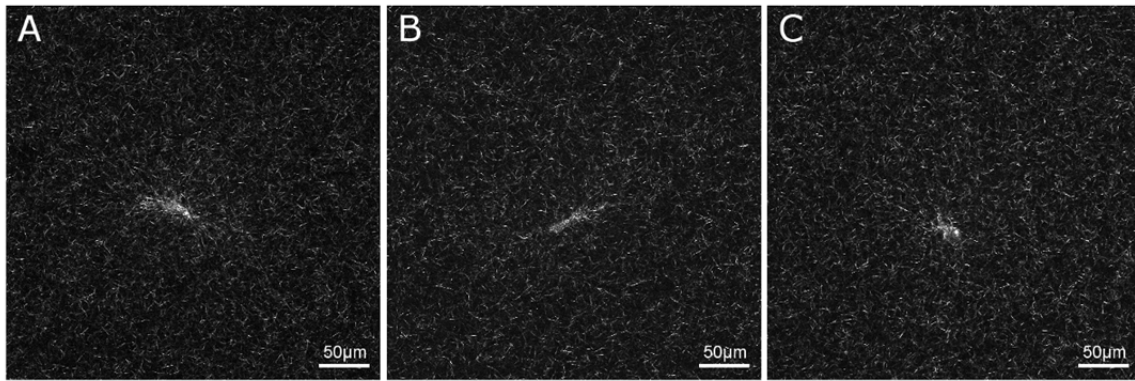


Figure 5.16: Collagen matrix structure imaging.

Collagen fiber network imaged using confocal reflection microscopy around an embedded: A) MDA-MB-231 cell, B) MDA-MD-231 cell with lam-A overexpressed and C) MDA-MD-231 cell with a 5- μ m polystyrene bead. The bright area in the center of the images is caused by the recruitment of the attached fibers to the cell.

5.3.4. Effect of steric hindrance on cell morphology

In this section, is explored the role of cell shape during cell invasion within 3-D collagen gels. From bright-field images stacks of cells embedded in 1.2 mg/ml collagen gels after 12 hours of culture, we quantify the maximum projected cell length (“major axis”), the largest cell dimension perpendicular to the major axis (“minor axis”), and the cell aspect ratio (the ratio of major to minor axis).

Cell aspect ratio in MDA-control cells (2.89 ± 0.27 , mean \pm se, for $n=33$) and MDA-lamA cells (2.42 ± 0.19 , for $n=33$) was not significantly altered ($p<0.05$) (see Figure 5.17D). This result indicates that the higher force polarity seen in MDA-lamA cells does not originate from a more elongated cell shape as we expected, but instead from an altered distribution of tractions across the cell surface. Similarly unexpected, we find a significantly shortened major axis and consequently lower aspect ratio in MDA-beads cells, but this does not translate into a lower force polarity, again pointing to an altered distribution of tractions across the cell surface (Figure 5.17D-F).

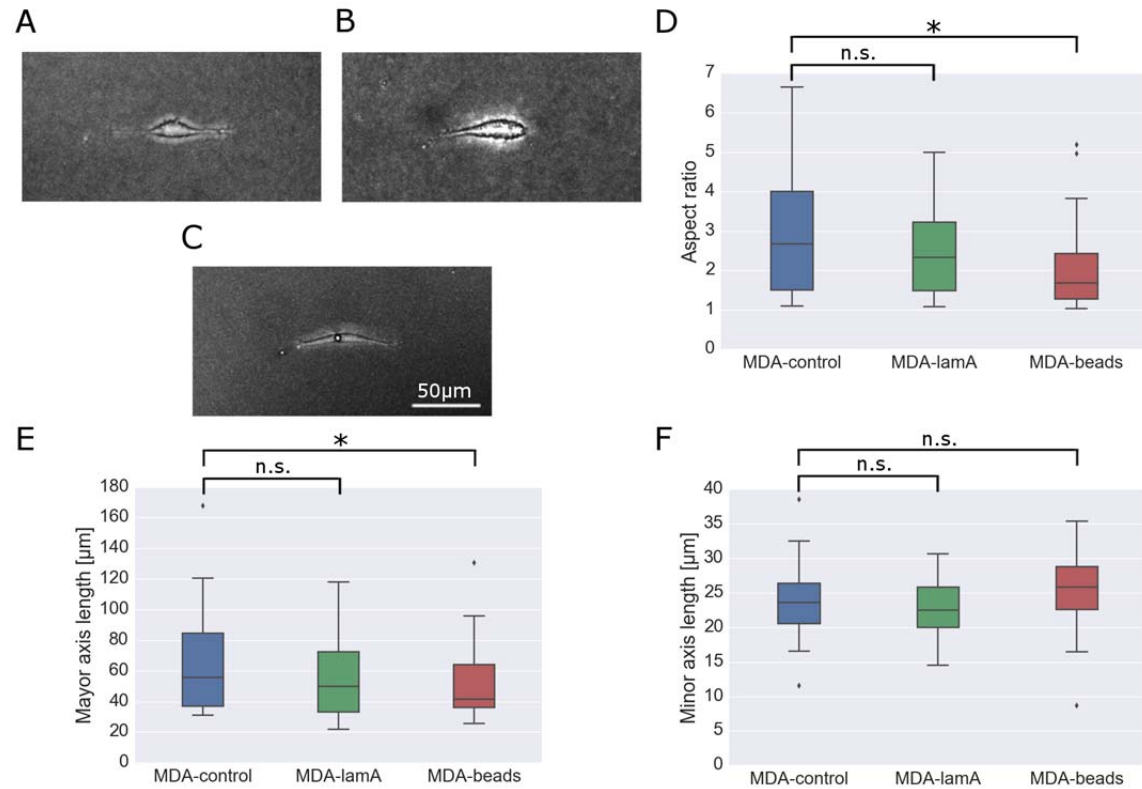


Figure 5.17: Influence of steric hindrance on the morphology of cells.

Maximum intensity projection image of a: A) MDA-MD-231 cell, B) MDA-MD-231 cell with lam-A overexpressed and C) MDA-MD-231 cell with a 5-μm polystyrene bead embedded on a 1.2 mg/ml collagen gel. D) Aspect ratio, E) major cell axis length and F) minor cell axis length of MDA-MB-231 cells (blue, for $n = 33$), MDA-MD-231 with lam-A overexpressed (green, for $n = 33$) and MDA-MD-231 with 5-μm polystyrene beads (red, for $n = 30$) in 1.2 mg/ml collagen gels. For all box plots the central line indicates the median, the edges of the box denote the first and third quartiles and the whiskers extend to the maximum and minimum value not considered as an outlier. The outliers are plotted as individual points. * $P \leq 0.05$, Student's t-test assuming unequal variances including the outliers; n.s., not significant ($P > 0.05$).

In line with this interpretation, we find that the contractility and cell aspect ratio of individual cells under all 3 hindrance conditions show a weak negative correlation (see Figure 5.18A-C), indicating that the more elongated cells tend to generate slightly smaller contractile forces, but this correlation did not reach statistical significance in our data.

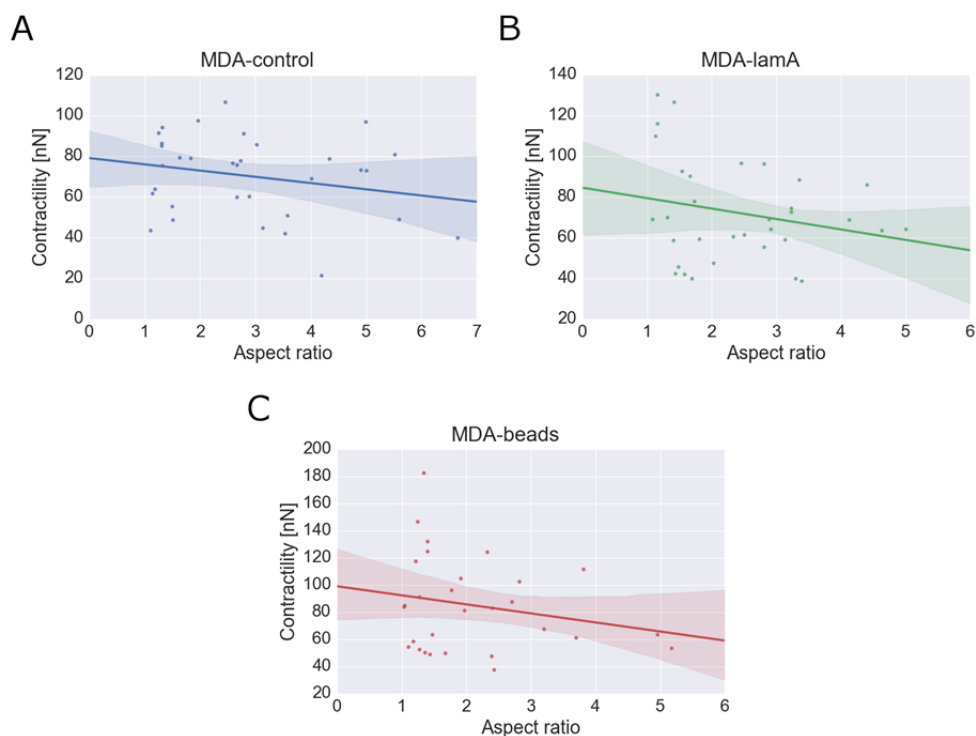


Figure 5.18: Correlation analysis between cell contractility and cell aspect ratio. Results of the correlation analysis for: A) MDA-MD-231 cells, B) MDA-MD-231 cells with lam-A overexpressed and C) MDA-MD-231 cells with a 5- μ m polystyrene bead embedded on a 1.2 mg/ml collagen gel.

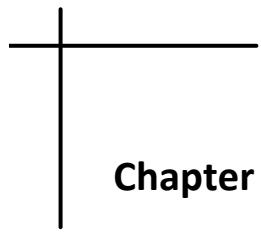
5.4. Discussion

In this study, it is investigated how cells migrate through a collagen network and respond to changes in steric hindrance that arise from altered cell mechanical properties. We increased steric hindrance either by stiffening the nucleus by overexpression the nuclear envelope protein lamin A, or by introducing 5 μ m polystyrene beads into the cells that are larger than the average network pore size of 3.8 μ m. Although both interventions may also cause secondary cellular responses that are difficult to predict, such as generation of reactive oxygen species, we argue that the ability to measure cell-generated traction forces and the migration behavior under identical matrix conditions compensates for the potential disadvantages.

Under both interventions, the percentage of cells that invaded into the collagen matrix decreased, as did the migration speed of the invasive cell fraction. These data are in line with previous results and support the notion that cell stiffness is inversely

correlated with cell invasiveness [232, 238]. Our data suggest, however, that cells attempt to compensate for the increased steric hindrance and the consequently reduced motility by two mechanisms. Under conditions of a moderately increased steric hindrance as in the case of MDA-lamA cells, the cells increase the force polarity and thus employ their contractile forces more efficiently. Under conditions of greatly increased steric hindrance as in the case of MDA-bead cells, the cells increase their contractile forces. Somewhat unexpectedly, this force increase was accompanied by a reduction of the cell aspect ratio and force polarity back to control levels. Also unexpectedly, the elastic strain energy stored in the collagen matrix was not increased, and was even reduced, under conditions of increased steric hindrance. Instead, we found an increased collagen matrix stiffening with increasing levels of steric hindrance. This matrix stiffening is the combined effect of contractile force magnitude, force polarity, and force vector distribution.

Importantly, matrix stiffening does not arise from outward-directed squeezing forces as the cells attempt to migrate through, and thereby widen, the confining pores of the matrix. Pore widening leads to a dramatic stiffening of the circumferential collagen fibers that constitute the pore, but this stiffening is highly localized and not detectable at the resolution of our measurements [115]. Rather, the observed matrix stiffening comes exclusively from the cell-generated inward-directed contractile forces. As the collagen fibers that carry the contractile stress are stretched, they cause an anisotropic and long-range stiffening of the collagen matrix that we are able to detect with this method [115]. We argue that this force-induced matrix stiffening, since it is not causing any further steric hindrance, promotes cell migration and hence is an important mechanism that cells employ to counteract steric hindrance. Cell shape, force magnitude and force distribution merely are the parameters that cells adapt to optimize cell and nuclear shape for easier migration through confining pores, and to distribute tractions for a more efficient movement. How exactly cell adapts each of these parameters, however, will depend on cell and nuclear mechanical properties and local matrix mechanical and structural properties.



Chapter 6

CONCLUSIONS

This chapter summarizes the work accomplished throughout the previous chapters, recapitulating the main conclusions and highlighting the original contributions of this Thesis. Finally, several open future lines of research are proposed.

6.1. Conclusions

The main objective of this Thesis was the development of numerical and computational models to achieve a better understanding of cell-matrix interactions, in particular cell traction forces, in 3-D physiological relevant matrices such as collagen type-I hydrogels. With this purpose, finite element-based approaches as well as experimental techniques were developed. Moreover, *in vitro* microfluidic-based devices were used and deeply investigated to better reproduce the physiological behavior of living cells and tissues.

The main conclusions of this Thesis are grouped by chapters and can be summarized as follows:

- Macroscopic simulation of cell-matrix adhesion:
 1. One-dimensional differential equations are adequate for modeling cell-matrix interactions and can be a useful tool to simulate complex behavior.
 2. Single-filopodium behavior was simulated on a continuous elastic substrate considering integrin reinforcement and tension-dependent strengthening of the adhesion through the evolution of the degree of adhesion state variable. The results reveal the existence of a mechanosensitive mechanism regulated by substrate deformation and therefore by its mechanical properties.
 3. The effect of direction and rate of traction force generation by cells through cell-matrix adhesions was investigated. Results demonstrate that cells adhere better on intermediate-rigidity substrates and generate stronger traction forces.
 4. Finally, the model illustrated that the behavior of cell-matrix adhesions is strongly dependent on the rate of force application and duration of loading. In particular, there is a biphasic behavior of the stability of FAs with respect to the magnitude of applied force. A relatively low force allows the growth and maturation of the FAs that stabilize the cell adhesion, while an excessively large force causes the disruption of cell adhesions.

- *In vitro* model for studying cell-matrix interactions:
 1. Microfluidic devices present new opportunities for studying cell-matrix interactions, allowing researchers to recreate and control the cell and tissues microenvironment and to create stable chemical gradients.
 2. Growth factor diffusion within 3-D matrices depends not only on the molecular diffusivity, but also on the geometrical parameters that characterizes these complex devices.
 3. The web-based application http://m2be.unizar.es/insilico_cell provides automatic estimation of growth factor diffusion within 3-D matrices inside a microfluidic device without prior knowledge of CAD or finite element modeling.
 4. The automatization of microfluidic device geometries generation greatly reduce the experimental validation processes, allowing to advance in the understanding of *in vitro* 3-D cell responses without the necessity of using commercial software or performing real testing experiments.

- Recursive method for reconstructing cell traction forces:
 1. The precise knowledge of the mechanical properties of both cell and matrix domains is crucial for obtaining a high accuracy of the predictions in traction force microscopy solutions, however errors in the cell mechanical estimates have only a relatively weak influence on the total error of the traction force magnitude.
 2. The numerical approach proposed here allows researchers to take into account the non-linear behavior of both domains, thus obtaining a good accuracy for cell traction forces reconstruction.
 3. This methodology can be used to study the effect of more complex cell substructures *in vitro*, such as the effect of cell nucleus mechanical properties or other cellular organelles, on the traction forces exerted by cells during cell migration or cell tissue invasion.

- Effect of cell mechanical properties on traction forces:
 1. The invasion assays show that by increasing apparent cell stiffness with polystyrene beads, steric effects of the matrix are enhanced, supporting the hypothesis that cell stiffness is inversely correlated with cell invasiveness. However, a less dramatic increase of nuclear stiffness had a surprisingly small effect on cell invasiveness, suggesting that cells may have responded with counteracting measures.
 2. Cells attempt to compensate for the increased steric hindrance and the consequently reduced motility by two mechanisms. Under conditions of a moderately increased steric hindrance as in the case of MDA-lamA cells, the cells increase the force polarity and thus employ their contractile forces more efficiently. Under conditions of greatly increased steric hindrance as in the case of MDA-beads cells, the cells increase their contractile forces.
 3. Unexpectedly, the elastic strain energy stored in the collagen matrix was not increased, and was even reduced, under conditions of increased steric hindrance. Instead, we found an increased collagen matrix stiffening with increasing levels of steric hindrance. This matrix stiffening is the combined effect of contractile force magnitude, force polarity, and force vector distribution.
 4. The higher force polarity seen in MDA-lamA cells does not originate from a more elongated cell shape as we expected, but instead from an altered distribution of tractions across the cell surface. Similarly unexpected, we find a significantly shortened major axis and consequently lower aspect ratio in MDA-beads cells, but this does not translate into a lower force polarity, again pointing to an altered distribution of tractions across the cell surface.
 5. In summary, we find that breast cancer cells are capable to mechanically adapt contractile forces, force polarity and the degree of stiffening of the collagen matrix around the cells, to compensate for steric hindrance alterations.

6.2. Original contributions

The foremost original contributions of this Thesis are the following:

- Development of a phenomenological cohesive model for simulating the dynamics of cell-matrix interactions as a function of an internal variable termed as adhesion degree, based on the principles of continuum damage mechanics.
- An *in vitro* model development by using microfluidic technology, designed to control the microenvironmental complexity of cells cultures and tissues.
- 3-D FE simulations of a microfluidic system to explore the chemical gradient formation process within these microfluidic devices.
- Analysis of the dependency of microfluidic devices geometry as well as the effect of different matrices onto the chemical gradient formation process.
- Development of a web-based application for automated quantification of chemical gradients in microfluidic devices.
- Formulation of a 3-D TFM inverse method by using a recursive algorithm based on finite elements.
- Analysis of the effect of the mechanical properties of both cell and matrix domains in the accuracy of the predictions in traction force microscopy.
- Experimental study of how cells respond to changes in steric hindrance that arise from altered cell mechanical properties.

6.2.1. Publications in peer-reviewed journals

The publications on international journals achieved during the Thesis period are listed below:

1. Moreno-Arotzena, G. Mendoza, **M. Córdor**, T. Rüberg and J.M. García-Aznar, *Inducing chemotactic and haptotactic cues in microfluidic devices for three-dimensional in vitro assays*. *Biomicrofluidics*, 8(6) 2014.
2. **M. Córdor** and J.M. García-Aznar, *A phenomenological cohesive model for the macroscopic simulation of cell–matrix adhesions*. *Biomechanics and Modeling in Mechanobiology*, 2017: p. 1-18.

3. **M. Córdor**, J. Steinwachs, C. Mark, J.M. García-Aznar and B. Fabry, *Traction Force Microscopy in 3-Dimensional Extracellular Matrix Networks*. Current protocols in cell biology, 2017: p. 10.22. 1-10.22. 20.
4. **M. Córdor**, T. Rüberg, C. Borau, J. Piles and J.M. García-Aznar, *A web-based application for automated quantification of chemical gradients induced in microfluidic devices*. Computers in Biology and Medicine, 2018.
5. C. Del Amo, V. Olivares, **M. Córdor**, A. Blanco, J. Santolaria, J. Asín, C. Borau and J.M. García-Aznar, *Matrix architecture plays a pivotal role on 3D osteoblast migration: effect of interstitial fluid flow*. Journal of the Mechanical Behavior of Biomedical Materials. 2018 (Under review).
6. **M. Córdor** and J.M. García-Aznar, *A recursive finite element-based approach for solving inverse problems in traction force microscopy*. 2018 (In preparation).
7. **M. Córdor**, C. Mark, R.C. Gerum, J.M. García-Aznar and B. Fabry, *Breast cancer cells adapt contractile forces to overcome steric hindrance*. 2018 (In preparation).

6.2.2. Congress and conference contributions

The following communications have been presented at national and international conferences and meetings:

1. **M. Córdor**, J.M. García-Aznar. *Finite element simulation of focal adhesion dynamics*. III Meeting of the National Chapter of the Spanish Society of Biomechanics (ESB). October 2013. Barcelona (Spain).
2. **M. Córdor**. *Finite element simulation of cell-substrate adhesion*. II Conference of Young Researchers of the Engineering Research Institute of Aragon (I3A). May 2013. Zaragoza (Spain).
3. J.M. García-Aznar, J. Escribano, **M. Córdor**, M.T. Sánchez. *Modeling cell-matrix adhesions at different scales*. VII World Biomechanics Congress (WCB). July 2014. Boston (USA).
4. J.M. García-Aznar, C. Borao, T. Rüberg, J. Escribano, **M. Córdor** and R.D. Kamm. *Modeling the mechanics of cell locomotion*. XI World Congress on Computational Mechanics (WCCM). July 2014. Barcelona (Spain).

5. **M. Córdor** and J.M. García Aznar. *Macroscopic simulation of cell-matrix adhesions*. VI European Cell Mechanics meeting (CELLMECH). May 2015. Barcelona (Spain).
6. C. Valero, **M. Córdor**, D. Navajas and J.M. García Aznar. *Apparent substrate stiffness sensed by cells depending on the substrate geometry and properties*. VI European Cell Mechanics meeting (CELLMECH). May 2015. Barcelona (Spain).
7. **M. Córdor** and J.M. García Aznar. *A phenomenological model for the macroscopic simulation of cell-matrix adhesion*. 9th European Solid Mechanics Conference (ESMC). July 2015. Carlos III University Madrid (Spain).
8. **M. Córdor**. *Cell traction forces in 3D microenvironments*. II Doctoral Conferences of the Iberus Campus. Oral presentation. July 2015. Jaca (Spain).
9. **M. Córdor** and J.M. García Aznar. *Numerical simulations for the determination of chemical gradients induced in collagen and fibrin hydrogels*. 14th international symposium in Computer Methods in Mechanics and Biomedical Engineering (CMMBE). September 2016. Tel Aviv (Israel).
10. **M. Córdor**, C. Borau and J.M. García Aznar. *Numerical predictions of chemical gradients generated in extracellular matrix networks*. Joint Meeting of the Spanish Network of Excellence in Mechanobiology and the European Innovative Training Network (BIOPOL). October 2016. Barcelona (Spain).
11. **M. Córdor**, R.C. Gerum, C. Mark, J.M. García-Aznar & B. Fabry. *Breast cancer cells adapt contractile forces as a function of cell stiffness*. 7th European Cell Mechanics Meeting (CELLMECH). June 2017. Windermere lake (England).
12. **M. Córdor**, O. Moreno-Arotzena, T. Rüberg, C. Borau and J.M. García-Aznar. *Numerical predictions of the chemical gradients induced in microfluidic-based chips*. Conference on Multiscale problems in Biomechanics and Mechanobiology (MultiBioMe). September 2017. Viena (Austria).

6.3. Future lines of work

Results and conclusions obtained throughout this work raise new questions and suggest possible future lines of research that need to be explored:

- Extension of the individual cell-matrix adhesion model proposed in chapter 2, taking into account the cell shape during cell adhesion processes. To that end, the introduction of cell geometry remodeling and cell remeshing of the FEM will be necessary.
- Studying the effect of chemical gradients on cell traction forces. To that end, the *in silico* model presented in chapter 3 can be used for inducing stationary chemical gradients. Cell traction forces can then be measured using the numerical method presented in chapter 4 of this Thesis.
- Study the effect of intracellular or sub-cellular structures, such as the mechanical properties of cell nucleus, on the cell traction forces using the FE method presented in chapter 4.



APPENDIX A: RESUMEN Y CONCLUSIONES

En este apéndice se presenta el resumen y los principales objetivos de esta Tesis, así como y las conclusiones más importantes obtenidas. Además se recogen las contribuciones originales obtenidas en este trabajo.

A.1 Antecedentes

Las células, para sobrevivir y crecer deben adherirse y esparcirse sobre el sustrato que las rodea [1-3]. Una vez adheridas, las células generan fuerzas internas de tracción a través de la interacción actino-miosina, que resultan en una tracción sobre el sustrato subyacente o la matriz extracelular (MEC) que las rodea. Estas fuerzas de tracción celular son por tanto esenciales para la migración celular, el mantenimiento de la forma celular, la generación de señales mecánicas y otras funciones celulares [4].

En los últimos años, los estudios de migración celular en sistemas tridimensionales de cultivo celular *in vivo*, han revelado numerosas diferencias cuando se comparan con estudios de migración celular en sistemas bidimensionales [5]. Cuando las células crecen sobre sustratos planos bidimensionales (2-D) las propiedades mecánicas, en particular la rigidez del sustrato subyacente, tienen una gran influencia en la migración celular [6, 7]. Además, diferentes estudios han demostrado que cuando las células migran sustratos más rígidos, estas forman adherencias focales mucho más estables, lo que conlleva a una menor velocidad de migración y contribuye a la durotaxis [1,8]. Sin embargo, cuando las células migran a través de una matriz tridimensional (3-D) estas deben vencer no sólo las fuerzas de adhesión, sino también las fuerzas de resistencia impuestas por la matriz que las rodea [9-11]. Las fuerzas de resistencia surgen principalmente de los efectos estéricos contra el movimiento de la célula, ya que ésta se mueve a través de la matriz y por consiguiente la deforma. Para superar este obstáculo, las células necesitan generar fuerzas de tracción que dependerán por tanto no sólo de las propiedades de la matriz (tamaño del poro y rigidez de las fibras [9, 12-14]) sino también de las propiedades de la célula (forma y rigidez de la célula [13, 15-19]).

Por consiguiente, el estudio de estas fuerzas así como la capacidad celular para deformar la MEC, es muy importante para una comprender mejor funciones fisiológicas y patológicas de las células tanto en condiciones de salud como de enfermedad que implican la adhesión celular, los cambios de forma y la migración, la formación de tejidos durante la embriogénesis, la invasión de células tumorales en el tejido, o la localización de células inmunitarias [8, 20-23]. Además, cuantificar estas fuerzas es importante para

comprender la función de las células musculares y otras células altamente contráctiles, como los fibroblastos, tanto a nivel de los tejidos como de los órganos.

A.1.1. Invasión celular

La mayor parte de las células que son capaces de adherirse, esparcirse y migrar en un sustrato 2-D también son capaces de adherirse, cambiar de forma y migrar en el interior de una red de biopolimérica con una adhesión, rigidez y porosidad de red adecuadas (ver Figura A.1).

La capacidad de las células para invadir un tejido conectivo depende de los siguientes factores, los cuales determinan la velocidad de migración de las células en matrices tridimensionales: la adhesión y el despegado celular, la capacidad de remodelación citoesquelética, las propiedades mecánicas tanto de las células como de la matriz, la remodelación de la matriz por secreción de enzimas proteolíticas y la generación de fuerzas protusivas [9,24]. Por tanto, el equilibrio de todos estos parámetros determina la capacidad de invasión celular en matrices tridimensionales y un cambio de este equilibrio puede conducir a un cambio hacia otro modo de invasión como el mesenquimal o ameboide, con o sin fuerzas de tracción, determinando por tanto la estrategia de invasión utilizada por las células [25].

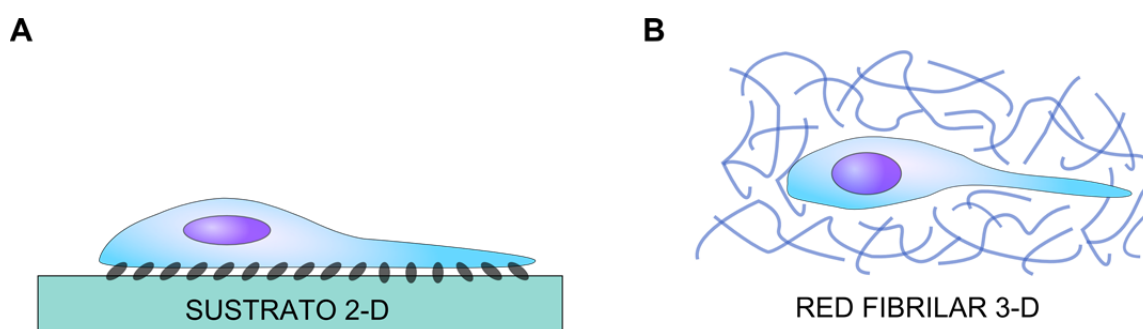


Figure A.1: Esquema de la migración celular en una matriz 2-D y 3-D.

La migración celular en sustratos 2-D depende en gran medida de la adhesión celular. Sin embargo, cuando las células migran en una red fibrilar tridimensional, se incrustan en el andamio y se someten pasivamente a contactos con la matriz circundante.

La forma en que las células regulan este equilibrio está todavía investigando, pero hay al menos dos mecanismos principales postulados: el primero es que las células invasoras degradan la MEC a través de la producción y secreción de enzimas proteolíticas que descomponen la MEC circundante; y el segundo se basa en que la invasión de la MEC no sólo depende de la actividad proteolítica de las metaloproteinasas de membrana, sino más bien en la generación de fuerzas de contracción por las células.

De hecho, varios estudios sugieren que la capacidad de invasión de las células depende de una combinación de ambos mecanismos y, por lo tanto, la generación de fuerzas de contracción es un elemento determinante de la velocidad de invasión celular así como de la profundidad de invasión de las células. Esto hace que la medición de fuerzas de contracción en entornos 2-D y 3-D sea un factor decisivo para determinar si una célula invade o no la MEC que las rodea [26,27].

A.1.2. Fuerzas de tracción celulares

Las células no musculares contienen haces de filamentos de actina, o fibras de esfuerzo, que forman estructuras semi-sarcómeras. Impulsado por la hidrólisis de adenosina trifosfato (ATP), los puentes cruzados de acto-miosina dentro de estas estructuras generan una tensión que hace que el cuerpo o el citoesqueleto de las células se contraiga [28,29]. Esta tensión es transmitida a la MEC y la fuerza ejercida sobre la MEC se denomina fuerza de tracción celular.

La polimerización de la actina es una segunda fuente de generación de fuerzas de tracción celular que impulsan hacia adelante las protuberancias situadas en el frente de avance de una célula migratoria [30, 31]. Para transmitir las fuerzas de tracción a la MEC, las células lo hacen a través de lo que se conocen como adhesiones focales (AFs). Las AFs están situadas en ambos extremos de las fibras de tensión y también en el sustrato [32] y por lo tanto conectan físicamente el citoesqueleto de las células con la MEC [33-35], siendo ésta la estructura principal a través de la cual se transmiten las fuerzas.

La adhesión focal es básicamente un conjunto de proteínas de la MEC, receptores transmembrana y proteínas estructurales y de señalización citoplasmáticas (ver Figura

A.2), incluyendo las integrinas $\alpha\text{v}\beta 3$ and $\alpha 5\beta 1$, vinculina, paxilina, talina, zyxina, tenina, proteína tirosina quinasa y fosfatasa [36, 37]. Además, entre estas proteínas contenidas en las adhesiones focales, las integrinas son las mediadoras primarias que proporcionan un vínculo físico entre la actina del citoesqueleto y la MEC, y por lo tanto juegan un papel fundamental en la mecanotransducción celular [38, 39].

A lo largo de los últimos años, muchos estudios se han centrado en investigar cómo las células se adhieren a la matriz extracelular a través de las AFs y cómo sus diferencias en tamaño y composición molecular hacen que se comporten distintivamente en la transmisión de fuerzas entre la célula y el sustrato [32, 40-43]. Por ejemplo, en las AFs más maduras en células relativamente estacionarias, la magnitud de las fuerzas de tracción se correlaciona linealmente con el tamaño de la AF [32, 35]. Sin embargo, si estos lugares de adhesión continúan madurando, hace que las fuerzas de tracción ejercidas por las células se incrementen notablemente. Curiosamente, otros estudios muestran cómo las células también ejercen fuerzas significativamente mayores en pequeños complejos focales, con un área promedio menor a un $1 \mu\text{m}^2$; donde el nivel de fuerza no se correlaciona nunca más con el tamaño de la adhesión [35]. En particular, cerca del borde de avance de una célula migratoria, por ejemplo de un fibroblasto, los pequeños complejos focales nacientes transmiten fuertes fuerzas de tracción, mientras que las adhesiones focales más grandes y maduras ejercen fuerzas mucho más débiles [40]. Por lo tanto, cambios en la estructura, la composición molecular y el nivel de fosforilación, junto con la maduración de las AFs, provocan un cambio en la transmisión de las fuerzas celulares sobre el sustrato subyacente [4, 44].

Sin embargo, trabajos recientes han destacado la importancia de examinar las adhesiones en ambientes tridimensionales puesto que son mucho más fisiológicos [46-48]. Aunque la caracterización de las adhesiones en matrices tridimensionales está todavía en fase muy primaria, los datos disponibles indican que las adhesiones en entornos bidimensionales y tridimensionales pueden diferir en algunos aspectos. Por ejemplo, se ha visto que cuando los fibroblastos están sobre sustratos 2-D o sembrados en el interior de matrices 3-D, la proteína tirosina quinasa (FAK) se fosforila de forma diferente en adhesiones en 2-D y 3-D [46]. Otros estudios también han mostrado diferencias en la señalización de las adhesiones, en la morfología y la composición entre

ambientes 2-D y 3-D [47, 49, 50]. Estas diferencias apuntan a la necesidad de caracterizar mejor estas adhesiones y otros tipos de interacciones entre células y matrices en entornos tridimensionales, como son las matrices de colágeno tipo I.

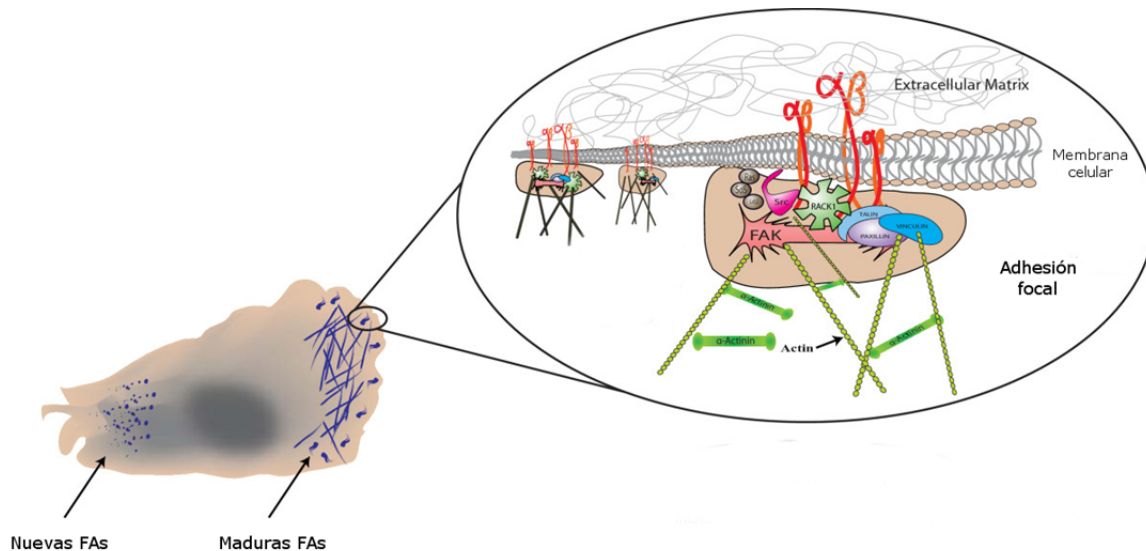


Figure A.2: Esquema de la adhesión celular a una matriz bidimensional.

Cuando una célula está en contacto con la MEC, las integrinas que se agrupan en la superficie celular conducen al reclutamiento de la proteína tirosina quinasa (FAK) y al establecimiento de las adhesiones focales. A través de las adhesiones focales, las células son capaces de transmitir fuerzas al sustrato y por lo tanto migrar. Figura adaptada de [45].

A.1.3. Hidrogeles biomiméticos tridimensionales

El tejido conectivo da un soporte mecánicamente estable a las células, permitiendo la difusión de oxígeno y nutrientes entre la microvasculatura y los tejidos adyacentes, y permitiendo a su vez el tráfico libre de las células en movimiento. El tejido conjuntivo está compuesto por una red de fibras biopoliméricas que contiene proteínas, proteoglicanos y glucosaminoglicanos que difieren en composición y estructura en las diferentes partes de nuestro cuerpo [51]. Cada tipo de tejido conectivo o conjuntivo tiene un tipo de MEC: por ejemplo la MEC del tejido óseo esta compuesta por fibras de colágeno y mineral óseo; la del tejido conjuntivo laxo esta compuesta por fibras reticulares y la sustancia fundamental; y la de la sangre es un tipo muy particular que esta formada por el plasma sanguíneo.

El componente más abundante de la MEC es el colágeno tipo I, una proteína fibrosa responsable de dar la rigidez a la MEC [52]. La rigidez y la alineación relativa de las fibras que componen la red son particularmente importantes para la función celular. De hecho, algunos estudios han revelado que los geles de colágeno denso y rígido pueden promover el crecimiento y la migración de células y tumores cancerosos [21, 53]. Otros ejemplos son la durotaxis, procesos en los que las células tienden a moverse hacia las matrices de mayor rigidez [54], y el contacto por orientación en el que las células tienden a alinearse y moverse en la dirección de la alineación de las fibras [55-57].

En las últimas décadas, los hidrogeles compuestos por biopolímeros se han convertido en una de las mejores alternativas para sustituir a los tejidos biológicos en el cultivo celular y la ingeniería tisular [58, 59]. Los hidrogeles formados por biopolímeros consisten en una red de polímeros compuesta por filamentos individuales interconectados la cual es embebida en un medio acuoso. Las propiedades de los filamentos individuales y la estructura global que forman, contribuyen a las propiedades mecánicas globales de los hidrogeles. Así pues, los parámetros geométricos como el diámetro de la fibra, el tamaño de los poros de la red, la distribución del tamaño de los poros o la longitud de la fibra pueden determinar las propiedades mecánicas o reológicas de estas redes y, al mismo tiempo, afectar al comportamiento de las células. Debido a sus efectos sobre el comportamiento y la comunicación celular, se ha realizado un trabajo significativo por caracterizar las propiedades físicas y estructurales de estas redes de biopolímeros [12, 60-64].

Para estudiar el comportamiento celular en microambientes tridimensionales, las MEC *in vitro* más utilizadas son: los geles de colágeno tipo I, los geles de fibrina y el extracto de membrana basal o Matrigel (ver Figura A.3) [65]. Todos ellos han sido utilizados para explorar diferencias en la morfología celular, señalización, adhesiones y motilidad, o incluso para cuantificar las fuerzas de tracción celular, que varían incluso para el mismo tipo de MEC dependiendo de las propiedades específicas o si las células están apoyadas o embebidas en su interior.

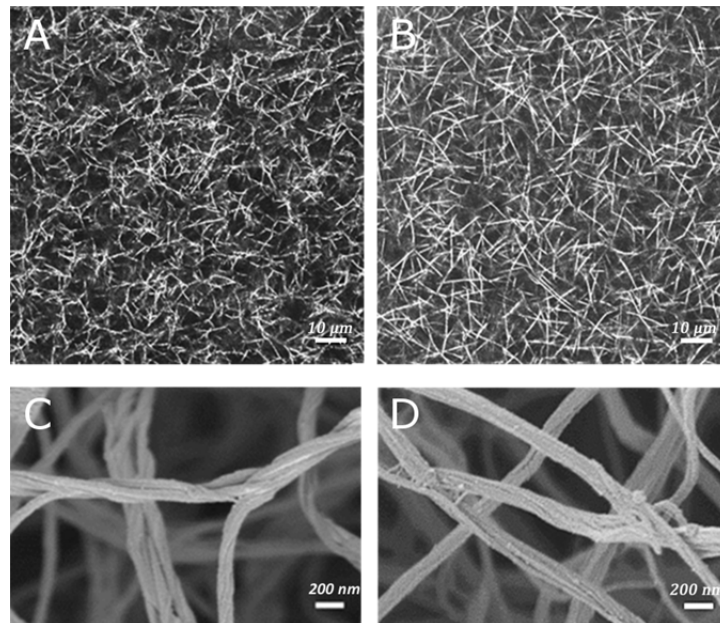


Figure A.3: Tipos de MEC para estudiar el comportamiento celular *in vitro*.

Imagen obtenida por microscopía confocal de reflexión a 120x de: A) un hidrogel de colágeno tipo I y B) un hidrogel de fibrina. Detalle de la estructura de la fibra, adquirida con microscopía SEM a 120kx de: C) un hidrogel de colágeno tipo I y D) un hidrogel de fibrina. Figura adaptada de [66].

Sin embargo, para estudiar las respuestas celulares de una manera más sencilla, como las fuerzas de tracción celular sobre sustratos planos (fuerzas de tracción en 2-D), los sustratos más utilizados son los hidrogeles de poliacrilamida-bisacrilamida. La principal ventaja que presenta el uso de este tipo de hidrogeles sintéticos radica en la sencillez de caracterización de las propiedades mecánicas, como por ejemplo el módulo elástico, permitiendo por tanto simplificar los métodos de medición de las deformaciones inducidas en el sustrato subyacente.

A.1.4. Microfluídica: Tecnología de vanguardia para el estudio de la interacción célula-matriz en ambientes 3-D

La investigación en ambientes *in vitro* 3-D ha crecido significativamente en los últimos años, ya que supone una mejor representación del microambiente de los tejidos vivos. El deseo de abordar ciertas cuestiones biológicas celulares que no pueden ser respondidas de otra manera más que de forma *in vitro*, ha conducido al desarrollo de tecnologías más avanzadas de imagen en tiempo real *in vivo* [67]. Sin embargo, los modelos *in vitro* siguen siendo indispensables para aislar y definir las contribuciones específicas de los factores individuales a la respuesta global en un tejido vivo.

Los recientes avances en las tecnologías de fabricación lo han hecho posible gracias a la creación de nuevos dispositivos de microfluídica que facilitan el control preciso del microambiente celular. La incorporación de la tecnología de microfluídica en la investigación de la respuesta biológica de células y tejidos frente diversos estímulos mecánicos, ha superado varias dificultades en los últimos años, permitiendo realizar experimentos *in vitro* a gran escala y al mismo tiempo controlar factores fisiológicos potencialmente importantes [68].

Los sistemas de microfluídica permiten un mayor control y versatilidad a la hora de diseñar y realizar experimentos y, por lo tanto, permiten crear modelos *in vitro* mucho más realistas de mecanotransducción en sistemas vivos. Además, esta tecnología también facilita la monitorización en tiempo real, por lo que se pueden realizar estudios cualitativos y cuantitativos en entornos 3-D (ver Figura A.4). Debido a todas estas ventajas, los sistemas de microfluídica presentan oportunidades únicas para el diseño de nuevos modelos *in vitro* fisiológicamente relevantes, lo que conduce a una transformación de los estudios actuales de mecanotransducción.

En resumen, los sistemas de cultivo celular microfluídico son una herramienta útil para aportar nuevos conocimientos a los mecanismos subyacentes mediante el control de la complejidad microambiental, los cuales pueden aplicarse a una amplia variedad de estudios *in vitro* como la angiogénesis, la función de órganos o al estudio de la migración de células tumorales [69, 70].

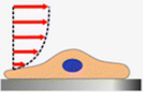
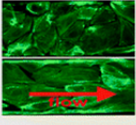
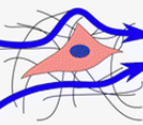
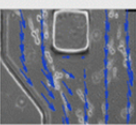
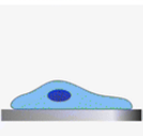
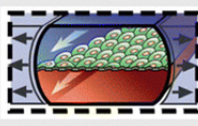
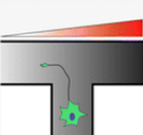
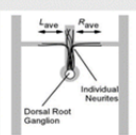

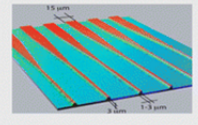
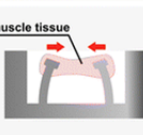
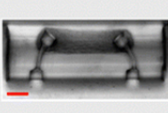
	Tipo de estímulo	Esquemas	Ejemplos de literatura
A	Esfuerzo cortante		
B	Flujo intersticial		
C	Estiramiento		
D	Gradiente de rigidez		
E	Confinado		
F	Medición de fuerzas		

Figure A.4: Diferentes tipos de dispositivos de microfluídica desarrollados para investigar la respuestas biológica de células y tejidos ante diversos estímulos mecánicos.

Tipo de estímulo inducido a las células (izquierda), esquema del sistema (centro) y ejemplos de literatura de dispositivos de microfluídica desarrollados (derecha). A) El paso de fluido a través de canales confinados induce un esfuerzo cortante a las células, mostrando alineación celular en la dirección del flujo [71, 72]. B) La aplicación de un gradiente de presión de fluido a través de un hidrogel, permite investigar el efecto del flujo intersticial sobre la migración y la alineación celular [73]. C) Mediante la incorporación de sustratos flexibles en plataformas de microfluídica, ha permitido estudiar el efecto del estiramiento mecánico sobre células cultivadas sobre un sustrato deformable [74]. D) Los gradientes de rigidez en sustratos dentro de dispositivos de microfluídica han sido utilizado para estudiar el efecto del gradiente de rigidez en la extensión axonal [75]. E) Sistemas de microfluídica utilizados para estudiar el efecto del confinamiento sobre el crecimiento de axones [76]. F) Nuevos dispositivos han sido desarrollados para medir las fuerzas generadas por células y tejidos activos, por ejemplo el microtejido cardíaco [77]. La figura es una adaptación de [68].

A.1.5. Estado del arte de la microscopía de fuerza de tracción

Las fuerzas de tracción celular son reguladores críticos de la adhesión, señalización y función celular y por lo tanto son cruciales en muchos procesos biológicos como la inflamación, la cicatrización de heridas, la angiogénesis o en la metástasis. A pesar de su gran importancia, la medición de las fuerzas celulares en un contexto fisiológico así como comprender su contribución en los procesos biológicos, sigue siendo todavía a día de hoy una tarea desafiante.

El concepto de microscopía de fuerza de tracción (MFT) fue desarrollado por primera vez en los años 80 por Harris et al. [78], quien demostró que los fibroblastos son capaces de deformar un sustrato elástico de silicona, mostrando así por tanto la actividad mecánica de las células. Sin embargo, este enfoque mostró algunas dificultades en la cuantificación de las fuerzas debido a la no linealidad que presenta la silicona y la baja resolución espacial de la técnica [79, 80]. Este enfoque se continuó desarrollando posteriormente mediante la combinación de técnicas de imagen de alta resolución y procedimientos computacionales extensivos, que indujeron una mejora significativa en la resolución, precisión y reproducibilidad de las mediciones de las fuerzas de tracción [34, 81-83].

Sin embargo, a pesar de que el MFT es una técnica ampliamente usada en la actualidad en muchos laboratorios biológicos, todavía pocos laboratorios son capaces de cuantificar las fuerzas celulares en ambientes tridimensionales. Es por ello que en los últimos años se han desarrollado diferentes métodos para cuantificar las fuerzas generadas por las células sobre sustratos tridimensionales con un impacto significativo en la comunidad biológica (ver Figura A.5). En la figura A.5 se presentan los fundamentos y consideraciones experimentales de los diferentes enfoques que los categorizan en función de: métodos que miden las fuerzas generadas por un tejido entero versus métodos que miden las fuerzas de tracción generadas por una célula individual [4, 84].

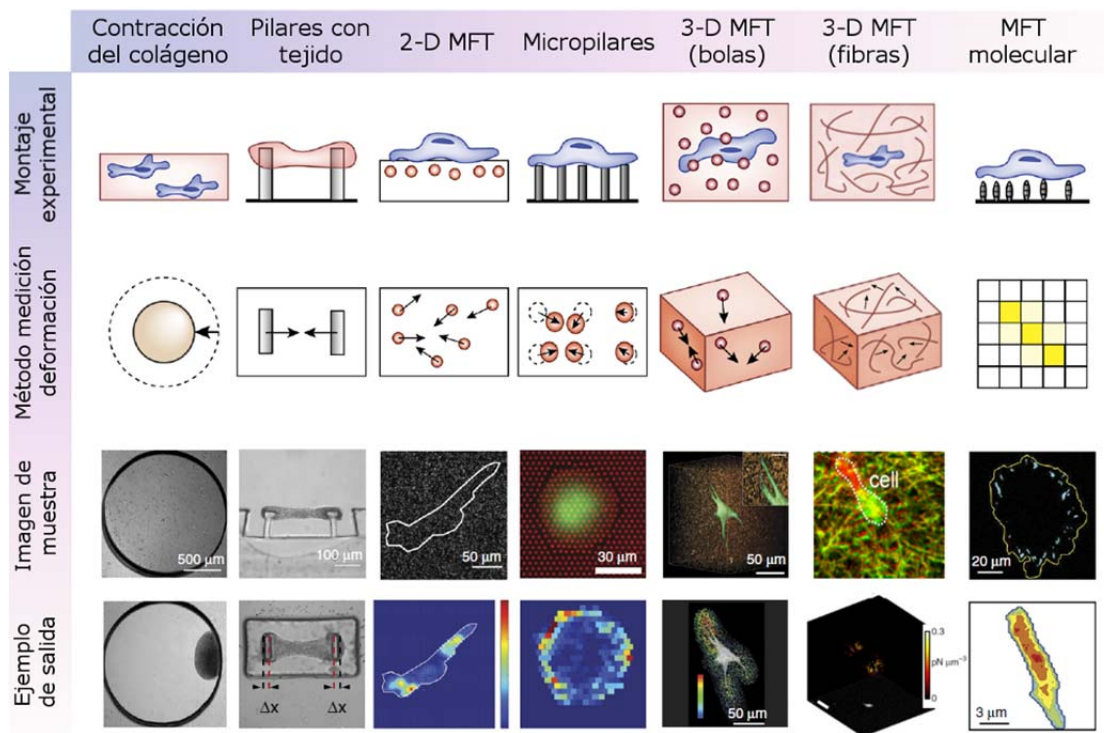


Figure A.5: Métodos para la medición de las fuerzas celulares.

Montaje experimental, método de medición de deformación, imagen de muestra y ejemplo de salida para los métodos de MFT más relevantes desarrollados en los últimos años para la medición de fuerzas celulares en tejidos y células individuales. Figura adaptada de [84].

A.2 Conclusiones

El objetivo principal de esta Tesis ha consistido en el desarrollo de modelos numéricos y computacionales, a fin de lograr una mejor comprensión de las interacciones célula-matriz, en particular de las fuerzas de tracción celular en matrices tridimensionales de gran relevancia fisiológica, como son los hidrogeles de colágeno tipo I. Con este propósito, se han desarrollado diferentes aproximaciones numéricas basadas en elementos finitos así como diferentes técnicas experimentales. Además, se han utilizado dispositivos de microfluídica para generar modelos *in vitro* con los que investigar y reproducir el comportamiento fisiológico de las células y tejidos vivos.

Las principales conclusiones de esta Tesis se han agrupado por capítulos y se resumen de la siguiente manera:

- Simulación macroscópica de la adhesión célula-matriz:
 1. Las ecuaciones diferenciales unidimensionales son adecuadas para modelar las interacciones célula-matriz y pueden ser una herramienta útil para simular este complejo comportamiento.
 2. El comportamiento de un filopodio sobre un sustrato elástico continuo ha sido simulado, considerando el fenómeno del refuerzo de integrinas y el fortalecimiento tensional de las adhesiones, a través de la evolución de una variable de estado interna, definida como el grado de adhesión. Los resultados revelan la existencia de un mecanismo mecanosensor el cual es regulado por la deformación del sustrato y por tanto por sus propiedades mecánicas.
 3. Se ha investigado el efecto de la dirección y velocidad de aplicación de las fuerzas de tracción generadas por las células a través de la adhesión a la matriz celular, concluyendo que las células se adhieren mejor a sustratos de rigidez intermedia, generando a su vez mayores fuerzas de tracción.
 4. Finalmente, el modelo desarrollado muestra como el comportamiento de las adhesiones célula-matriz depende en gran medida de la velocidad de aplicación de la fuerza y de la duración de la carga. Es particular, existe un comportamiento bifásico que regula la estabilidad de las adhesiones focales con respecto a la magnitud de la fuerza aplicada. Una fuerza relativamente baja permite el crecimiento y la maduración de las adhesiones focales que estabilizan la adhesión celular, mientras que una fuerza excesivamente grande causa la ruptura de las adhesiones celulares.
- Modelo *in vitro* para el estudio de las interacciones célula-matriz:
 1. Los dispositivos de microfluídica presentan nuevas oportunidades para estudiar las interacciones célula-matriz, permitiendo a los investigadores recrear y controlar los microambientes de células y tejidos además de permitir crear gradientes químicos estables en su interior.

2. La difusión de un factor de crecimiento en el interior de matrices tridimensionales depende no sólo de la física de difusión, sino también de los parámetros geométricos que caracterizan estos complejos dispositivos.
 3. La aplicación web desarrollada http://m2be.unizar.es/insilico_cell proporciona libremente a todo usuario, una estimación automática de la difusión de un factor de crecimiento a través de una matriz 3-D en el interior de un dispositivo microfluídico, sin necesidad de tener conocimientos previos de modelado CAD o de elementos finitos.
 4. La automatización de las geometrías de los dispositivos de microfluídica reduce en gran medida los procesos de validación experimental, permitiendo por tanto avanzar en la comprensión de las respuestas celulares *in vitro* sin la necesidad de utilizar un software comercial o de realizar experimentos reales.
- Método recursivo para la reconstrucción de las fuerzas de tracción celulares:
 1. El conocimiento preciso de las propiedades mecánicas de los dominios de la célula y de la matriz es crucial para obtener una alta precisión en las soluciones de microscopía de fuerza de tracción; sin embargo, los errores en las estimaciones mecánicas de la célula sólo tienen una influencia relativamente débil en el error total de la magnitud de la fuerza de tracción.
 2. El enfoque numérico aquí propuesto permite tener en cuenta el comportamiento no lineal de ambos dominios (la célula y la matriz), obteniendo así una buena precisión en la reconstrucción de las fuerzas de tracción celulares.
 3. Esta metodología permite por tanto estudiar *in vitro* el efecto de subestructuras celulares mucho más complejas, como por ejemplo las propiedades mecánicas del núcleo u otros orgánulos celulares, sobre las fuerzas de tracción ejercidas por las células durante la migración celular o la invasión de diferentes tejidos celulares.

- Efecto de las propiedades mecánicas de la célula en las fuerzas de tracción:
 1. Los ensayos de invasión realizados han mostrado como al aumentar la rigidez celular aparente con esferas de poliestireno, los efectos estéricos de la matriz han sido incrementados, apoyando por tanto la hipótesis de que la rigidez celular está inversamente correlacionada con la capacidad de invasión celular. Sin embargo, un aumento menos dramático de la rigidez nuclear ha mostrado un efecto sorprendentemente pequeño en la invasión celular, sugiriendo que en este caso las células han sido capaces de compensar este efecto.
 2. Las células intentan compensar el incremento estérico y por tanto la consiguiente reducción de la motilidad mediante dos mecanismos. Bajo condiciones de un aumento moderado del efecto estérico, como es el caso de las células MDA-lamA, las células aumentan la polaridad de las fuerzas y por tanto emplean sus fuerzas contráctiles más eficientemente. Sin embargo, en condiciones en las que un mayor aumento del efecto estérico se ha producido, como es el caso de las células MDA-beads, las células responden aumentando sus fuerzas contráctiles.
 3. Inesperadamente, la energía elástica almacenada en el interior de la matriz de colágeno no se ha visto incrementada bajo un aumento del efecto estérico, sino que incluso en algunos casos esta se ha visto reducida. Sin embargo, se ha observado un aumento en la rigidez de la matriz de colágeno bajo un aumento del efecto estérico. Este aumento en la rigidez de la matriz es por tanto el efecto combinado de la magnitud de fuerza contráctil, la polaridad de la fuerza y la distribución del vector de fuerza.
 4. El aumento observado en la polaridad de las fuerzas para el caso MDA-lamA no ha sido originado por un aumento de la longitud de las células tal y como esperábamos, sino por una alteración de la distribución de las tracciones en la superficie celular. Igualmente inesperado, encontramos una disminución del eje mayor para el caso de MDA-beads y por consiguiente de la relación de aspecto, lo cual no es traducido en una menor polaridad, lo que apunta nuevamente a una alteración en la distribución de las tracciones en la superficie celular.

5. En resumen, hemos visto que las células de cáncer de mama son capaces de adaptar mecánicamente las fuerzas contráctiles, modificar la polaridad e incluso rigidizar la matriz de colágeno alrededor de las células, para compensar las alteraciones estéricas de la matriz de colágeno en 3-D.

A.3 Contribuciones originales

A continuación se detallan las principales contribuciones originales de esta Tesis entre las que se recogen publicaciones, ponencias en congresos internacionales y otros méritos como la dirección de proyectos fin de grado y fin de máster, así como de docencia en diferentes asignaturas de grado y máster en la Universidad de Zaragoza.

A.3.1. Publicaciones relacionadas con la Tesis

Los siguientes trabajos hacen referencia a los trabajos publicados (o que serán próximamente publicados) en revistas científicas internacionales indexadas (JCR), cuyo contenido está total o parcialmente recogido en esta Tesis:

1. Moreno-Arotzena, G. Mendoza, **M. Córdor**, T. Rüberg and J.M. García-Aznar, *Inducing chemotactic and haptotactic cues in microfluidic devices for three-dimensional in vitro assays*. *Biomicrofluidics*, 8(6) 2014.
2. **M. Córdor** and J.M. García-Aznar, *A phenomenological cohesive model for the macroscopic simulation of cell-matrix adhesions*. *Biomechanics and Modeling in Mechanobiology*, 2017: p. 1-18.
3. **M. Córdor**, J. Steinwachs, C. Mark, J.M. García-Aznar and B. Fabry, *Traction Force Microscopy in 3-Dimensional Extracellular Matrix Networks*. *Current protocols in cell biology*, 2017: p. 10.22. 1-10.22. 20.
4. **M. Córdor**, T. Rüberg, C. Borau, J. Piles and J.M. García-Aznar, *A web-based application for automated quantification of chemical gradients induced in microfluidic devices*. *Computers in Biology and Medicine*, 2018.
5. C. Del Amo, V. Olivares, **M. Córdor**, A. Blanco, J. Santolaria, J. Asín, C. Borau and J.M. García-Aznar, *Matrix architecture plays a pivotal role on 3D osteoblast migration: effect of interstitial fluid flow*. *Journal of the Mechanical Behavior of Biomedical Materials*. 2018 (En revisión).

6. **M. C3ndor** and J.M. Garc3a-Aznar, *A recursive finite element-based approach for solving inverse problems in traction force microscopy*. 2018 (En preparaci3n).
7. **M. C3ndor**, C. Mark, R.C. Gerum, J.M. Garc3a-Aznar and B. Fabry, *Breast cancer cells adapt contractile forces to overcome steric hindrance*. 2018 (En preparaci3n).

A.3.2. Contribuciones a congresos

Las siguientes ponencias han sido presentadas en congresos nacionales y reuniones internacionales durante el desarrollo de esta Tesis:

1. **M. C3ndor**, J.M. Garc3a-Aznar. *Finite element simulation of focal adhesion dynamics*. III Meeting of the National Chapter of the Spanish Society of Biomechanics (ESB). October 2013. Barcelona (Spain).
2. **M. C3ndor**. *Finite element simulation of cell-substrate adhesi3n*. II Conference of Young Researchers of the Engineering Research Institute of Aragon (I3A). May 2013. Zaragoza (Spain).
3. J.M. Garc3a-Aznar, J. Escribano, **M. C3ndor**, M.T. S3nchez. *Modeling cell-matrix adhesions at different scales*. VII World Biomechanics Congress (WCB). July 2014. Boston (USA).
4. J.M. Garc3a-Aznar, C. Borao, T. R3berg, J. Escribano, **M. C3ndor** and R.D. Kamm. *Modeling the mechanics of cell locomotion*. XI World Congress on Computational Mechanics (WCCM). July 2014. Barcelona (Spain).
5. **M. C3ndor** and J.M. Garc3a Aznar. *Macroscopic simulation of cell-matrix adhesions*. VI European Cell Mechanics meeting (CELLMECH). May 2015. Barcelona (Spain).
6. C. Valero, **M. C3ndor**, D. Navajas and J.M. Garc3a Aznar. *Apparent substrate stiffness sensed by cells depending on the substrate geometry and properties*. VI European Cell Mechanics meeting (CELLMECH). May 2015. Barcelona (Spain).
7. **M. C3ndor** and J.M. Garc3a Aznar. *A phenomenological model for the macroscopic simulation of cell-matrix adhesion*. 9th European Solid Mechanics Conference (ESMC). July 2015. Carlos III University Madrid (Spain).

8. **M. Cóndor.** *Cell traction forces in 3D microenvironments.* II Doctoral Conferences of the Iberus Campus. Oral presentation. July 2015. Jaca (Spain).
9. **M. Cóndor** and J.M. García Aznar. *Numerical simulations for the determination of chemical gradients induced in collagen and fibrin hydrogels.* 14th international symposium in Computer Methods in Mechanics and Biomedical Engineering (CMMBE). September 2016. Tel Aviv (Israel).
10. **M. Cóndor,** C. Borau and J.M. García Aznar. *Numerical predictions of chemical gradients generated in extracellular matrix networks.* Joint Meeting of the Spanish Network of Excellence in Mechanobiology and the European Innovative Training Network (BIOPOL). October 2016. Barcelona (Spain).
11. **M. Cóndor,** R.C. Gerum, C. Mark, J.M. García-Aznar & B. Fabry. *Breast cancer cells adapt contractile forces as a function of cell stiffness.* 7th European Cell Mechanics Meeting (CELLMECH). June 2017. Windermere lake (England).
12. **M. Cóndor,** O. Moreno-Arotzena, T. Rüberg, C. Borau and J.M. García-Aznar. *Numerical predictions of the chemical gradients induced in microfluidic-based chips.* Conference on Multiscale problems in Biomechanics and Mechanobiology (MultiBioMe). September 2017. Viena (Austria).

A.3.3. Otras contribuciones

Durante la realización de esta Tesis y dentro del programa de formación de personal docente investigador se han realizado los siguientes encargos o tareas docentes en el departamento de Ingeniería Mecánica dentro del área de Mecánica de medios continuos y Teoría de estructuras:

1. **M. Cóndor.** Mecánica de sólidos deformables. Grado de Ingeniería Industrial. 52 horas en el curso 2016-2017.
2. **M. Cóndor.** Biomecánica y biomateriales. Máster de Ingeniería Biomédica. 8 horas en el curso 2016-2017.
3. **M. Cóndor.** Mecánica de sólidos deformables. Grado de Ingeniería Industrial. 52 horas en el curso 2017-2018.
4. **M. Cóndor.** Biomecánica y biomateriales. Máster de Ingeniería Biomédica. 8 horas en el curso 2017-2018.

Además durante la realización de esta Tesis se ha llevado a cabo la codirección de los siguientes proyectos fin de grado y trabajos fin de máster en la Universidad de Zaragoza:

1. *Modelado específico de una célula individual mediante elementos finitos para la obtención de las fuerzas de tracción.* Nicolás Laita Dieste. Trabajo Fin de Grado. Curso 2016-2017. **M. Cóndor** and J.M. García Aznar.
2. *Reconstrucción 3-D y caracterización de geles de colágeno a partir de imágenes de microscopía confocal.* Vanesa Olivares Velencoso. Trabajo Fin de Máster. Curso 2016-2017. **M. Cóndor** and J.M. García Aznar.

A.4 Líneas futuras

La variedad de enfoques presentados en esta Tesis no es más que una pequeña contribución en la comprensión del comportamiento de las interacciones entre las células y las diferentes matrices que las rodean. Los resultados y conclusiones obtenidos a lo largo de este trabajo plantean nuevas preguntas y sugieren posibles líneas de investigación que es preciso explorar. Algunas de las líneas futuras se enumeran a continuación:

- Ampliación del modelo de adhesión célula-matriz propuesto en el capítulo 2, teniendo en cuenta la forma de la célula durante el proceso de adhesión celular. Para ello, será necesaria la introducción de la remodelación de la geometría celular y habría que tener en cuenta en el modelo de elementos finitos.
- Estudio del efecto de los gradientes químicos sobre las fuerzas de tracción celular. Para ello, el modelo *in silico* presentado en el capítulo 3 puede ser utilizado para inducir gradientes químicos estables en diferentes líneas celulares. Las fuerzas de tracción celular pueden ser por tanto calculadas utilizando el método numérico presentado en el capítulo 4 de esta Tesis.
- Estudiar el efecto de las estructuras intracelulares o subcelulares, tales como las propiedades mecánicas del núcleo de las células, en las fuerzas de tracción celular, haciendo uso del modelo de elementos finitos presentado en el capítulo 4.

BIBLIOGRAPHY

1. Wang, H.B., et al., *Focal adhesion kinase is involved in mechanosensing during fibroblast migration*. Proceedings of the National Academy of Sciences of the United States of America, 2001. **98**(20): p. 11295-11300.
2. Yang, Z.C., et al., *Determining substrate displacement and cell traction fields - a new approach*. Journal of Theoretical Biology, 2006. **242**(3): p. 607-616.
3. Tolic-Norrelykke, I.M. and N. Wang, *Traction in smooth muscle cells varies with cell spreading*. Journal of Biomechanics, 2005. **38**(7): p. 1405-1412.
4. Wang, J.H.C. and J.S. Lin, *Cell traction force and measurement methods*. Biomechanics and Modeling in Mechanobiology, 2007. **6**(6): p. 361-371.
5. Friedl, P., et al., *New dimensions in cell migration*. Nat Rev Mol Cell Biol, 2012. **13**(11): p. 743-7.
6. Pelham, R.J. and Y.L. Wang, *Cell locomotion and focal adhesions are regulated by substrate flexibility*. Proceedings of the National Academy of Sciences of the United States of America, 1997. **94**(25): p. 13661-13665.
7. Lautscham, L.A., et al., *Biomembrane-mimicking lipid bilayer system as a mechanically tunable cell substrate*. Biomaterials, 2014. **35**(10): p. 3198-3207.
8. Lo, C.M., et al., *Cell movement is guided by the rigidity of the substrate*. Biophysical Journal, 2000. **79**(1): p. 144-152.
9. Zaman, M.H., et al., *Migration of tumor cells in 3D matrices is governed by matrix stiffness along with cell-matrix adhesion and proteolysis (vol 103, pg 10889, 2006)*. Proceedings of the National Academy of Sciences of the United States of America, 2006. **103**(37): p. 13897-13897.
10. Doyle, A.D., et al., *One-dimensional topography underlies three-dimensional fibrillar cell migration*. Journal of Cell Biology, 2009. **184**(4): p. 481-490.
11. Friedl, P. and E.B. Brocker, *The biology of cell locomotion within three-dimensional extracellular matrix*. Cellular and Molecular Life Sciences, 2000. **57**(1): p. 41-64.
12. Lang, N.R., et al., *Biphasic response of cell invasion to matrix stiffness in three-dimensional biopolymer networks*. Acta Biomaterialia, 2015. **13**: p. 61-67.
13. Wolf, K., et al., *Physical limits of cell migration: Control by ECM space and nuclear deformation and tuning by proteolysis and traction force*. Journal of Cell Biology, 2013. **201**(7): p. 1069-1084.
14. Miron-Mendoza, M., J. Seemann, and F. Grinnell, *The differential regulation of cell motile activity through matrix stiffness and porosity in three dimensional collagen matrices*. Biomaterials, 2010. **31**(25): p. 6425-6435.
15. Davidson, P.M., et al., *Nuclear Deformability Constitutes a Rate-Limiting Step During Cell Migration in 3-D Environments*. Cellular and Molecular Bioengineering, 2014. **7**(3): p. 293-306.
16. Friedl, P., K. Wolf, and J. Lammerding, *Nuclear mechanics during cell migration*. Current Opinion in Cell Biology, 2011. **23**(1): p. 55-64.
17. C ndor, M. and J.M. Garc a-Aznar, *A phenomenological cohesive model for the macroscopic simulation of cell-matrix adhesions*. Biomechanics and Modeling in Mechanobiology, 2017: p. 1-18.

18. Lange, J.R., et al., *Nuclear Deformability is Critically Dependent on Lamin A/B*. Biophysical Journal, 2014. **106**(2): p. 576a-576a.
19. Lammerding, J., et al., *Lamins A and C but not lamin B1 regulate nuclear mechanics*. Journal of Biological Chemistry, 2006. **281**(35): p. 25768-25780.
20. Galbraith, C.G., K.M. Yamada, and M.P. Sheetz, *The relationship between force and focal complex development*. Journal of Cell Biology, 2002. **159**(4): p. 695-705.
21. Levental, K.R., et al., *Matrix Crosslinking Forces Tumor Progression by Enhancing Integrin Signaling*. Cell, 2009. **139**(5): p. 891-906.
22. Friedl, P. and K. Wolf, *Tumour-cell invasion and migration: Diversity and escape mechanisms*. Nature Reviews Cancer, 2003. **3**(5): p. 362-374.
23. Eisenberg, J.L., et al., *Substrate stiffness regulates extracellular matrix deposition by alveolar epithelial cells*. Research and reports in biology, 2011. **2011**(2): p. 1.
24. Mierke, C.T., *The Role of Vinculin in the Regulation of the Mechanical Properties of Cells*. Cell Biochemistry and Biophysics, 2009. **53**(3): p. 115-126.
25. Wolf, K., et al., *Compensation mechanism in tumor cell migration: mesenchymal-amoeboid transition after blocking of pericellular proteolysis*. Journal of Cell Biology, 2003. **160**(2): p. 267-277.
26. Mierke, C.T., et al., *Breakdown of the endothelial barrier function in tumor cell transmigration*. Biophysical Journal, 2008. **94**(7): p. 2832-2846.
27. Rosel, D., et al., *Up-regulation of Rho/ROCK signaling in sarcoma cells drives invasion and increased generation of protrusive forces*. Molecular Cancer Research, 2008. **6**(9): p. 1410-1420.
28. Kolega, J., L.W. Janson, and D.L. Taylor, *The Role of Solation Contraction Coupling in Regulating Stress Fiber Dynamics in Nonmuscle Cells*. Journal of Cell Biology, 1991. **114**(5): p. 993-1003.
29. Sanger, J.W., J.M. Sanger, and B.M. Jockusch, *Differences in the Stress Fibers between Fibroblasts and Epithelial-Cells*. Journal of Cell Biology, 1983. **96**(4): p. 961-969.
30. Bereiter-Hahn, J., *Mechanics of crawling cells*. Medical Engineering & Physics, 2005. **27**(9): p. 743-753.
31. Elson, E.L., et al., *Forces in cell locomotion*. Cell Behaviour: Control and Mechanism of Motility, 1999. **65**: p. 299-314.
32. Balaban, N.Q., et al., *Force and focal adhesion assembly: a close relationship studied using elastic micropatterned substrates*. Nat Cell Biol, 2001. **3**(5): p. 466-72.
33. Burton, K., J.H. Park, and D.L. Taylor, *Keratocytes generate traction forces in two phases*. Molecular Biology of the Cell, 1999. **10**(11): p. 3745-3769.
34. Lee, J., et al., *Traction Forces Generated by Locomoting Keratocytes*. Journal of Cell Biology, 1994. **127**(6): p. 1957-1964.
35. Tan, J.L., et al., *Cells lying on a bed of microneedles: An approach to isolate mechanical force*. Proceedings of the National Academy of Sciences of the United States of America, 2003. **100**(4): p. 1484-1489.
36. Geiger, B. and A. Bershadsky, *Assembly and mechanosensory function of focal contacts*. Current Opinion in Cell Biology, 2001. **13**(5): p. 584-592.
37. Zamir, E. and B. Geiger, *Molecular complexity and dynamics of cell-matrix adhesions*. J Cell Sci, 2001. **114**(Pt 20): p. 3583-90.

38. Ingber, D.E., *Mechanosensation through integrins: Cells act locally but think globally*. Proceedings of the National Academy of Sciences of the United States of America, 2003. **100**(4): p. 1472-1474.
39. Wang, N., J.P. Butler, and D.E. Ingber, *Mechanotransduction across the Cell-Surface and through the Cytoskeleton*. Science, 1993. **260**(5111): p. 1124-1127.
40. Beningo, K.A., et al., *Nascent focal adhesions are responsible for the generation of strong propulsive forces in migrating fibroblasts*. J Cell Biol, 2001. **153**(4): p. 881-8.
41. Riveline, D., et al., *Focal contacts as mechanosensors: externally applied local mechanical force induces growth of focal contacts by an mDia1-dependent and ROCK-independent mechanism*. J Cell Biol, 2001. **153**(6): p. 1175-86.
42. Oria, R., et al., *Force loading explains spatial sensing of ligands by cells*. Nature, 2017. **552**(7684): p. 219-+.
43. Escribano, J., M. Sánchez, and J. García-Aznar, *A discrete approach for modeling cell-matrix adhesions*. Computational Particle Mechanics, 2014: p. 1-14.
44. Li, S., J.L. Guan, and S. Chien, *Biochemistry and biomechanics of cell motility*. Annual Review of Biomedical Engineering, 2005. **7**: p. 105-150.
45. Adams, D.R., D. Ron, and P.A. Kiely, *RACK1, A multifaceted scaffolding protein: Structure and function*. Cell Communication and Signaling, 2011. **9**.
46. Cukierman, E., R. Pankov, and K.M. Yamada, *Cell interactions with three-dimensional matrices*. Current Opinion in Cell Biology, 2002. **14**(5): p. 633-639.
47. Harunaga, J.S. and K.M. Yamada, *Cell-matrix adhesions in 3D*. Matrix Biology, 2011. **30**(7-8): p. 363-368.
48. Broussard, J.A., et al., *Automated Analysis of Cell-Matrix Adhesions in 2D and 3D Environments*. Scientific Reports, 2015. **5**.
49. Hakkinen, K.M., et al., *Direct Comparisons of the Morphology, Migration, Cell Adhesions, and Actin Cytoskeleton of Fibroblasts in Four Different Three-Dimensional Extracellular Matrices*. Tissue Engineering Part A, 2011. **17**(5-6): p. 713-724.
50. Li, S., et al., *Genomic analysis of smooth muscle cells in three-dimensional collagen matrix*. Faseb Journal, 2002. **16**(13): p. 97-+.
51. Brabek, J., et al., *The role of the tissue microenvironment in the regulation of cancer cell motility and invasion*. Cell Communication and Signaling, 2010. **8**.
52. Lodish, H., et al., *Collagen: the fibrous proteins of the matrix*. Molecular Cell Biology, 2000. **4**.
53. Tilghman, R.W., et al., *Matrix Rigidity Regulates Cancer Cell Growth and Cellular Phenotype*. Plos One, 2010. **5**(9).
54. Hadjipanayi, E., V. Mudera, and R.A. Brown, *Guiding Cell Migration in 3D: A Collagen Matrix with Graded Directional Stiffness*. Cell Motility and the Cytoskeleton, 2009. **66**(3): p. 121-128.
55. Guido, S. and R.T. Tranquillo, *A Methodology for the Systematic and Quantitative Study of Cell Contact Guidance in Oriented Collagen Gels - Correlation of Fibroblast Orientation and Gel Birefringence*. Journal of Cell Science, 1993. **105**: p. 317-331.
56. Provenzano, P.P., et al., *Contact Guidance Mediated Three-Dimensional Cell Migration is Regulated by Rho/ROCK-Dependent Matrix Reorganization*. Biophysical Journal, 2008. **95**(11): p. 5374-5384.

57. Liang, L., et al., *Heterogeneous force network in 3D cellularized collagen networks*. Physical Biology, 2016. **13**(6).
58. Van Vlierberghe, S., P. Dubruel, and E. Schacht, *Biopolymer-based hydrogels as scaffolds for tissue engineering applications: a review*. Biomacromolecules, 2011. **12**(5): p. 1387-1408.
59. Reddy, N., R. Reddy, and Q.R. Jiang, *Crosslinking biopolymers for biomedical applications*. Trends in Biotechnology, 2015. **33**(6): p. 362-369.
60. Yang, Y.L., S. Motte, and L.J. Kaufman, *Pore size variable type I collagen gels and their interaction with glioma cells*. Biomaterials, 2010. **31**(21): p. 5678-5688.
61. Petrie, R.J. and K.M. Yamada, *At the leading edge of three-dimensional cell migration*. Journal of Cell Science, 2012. **125**(24): p. 5917-5926.
62. Gardel, M.L., et al., *Elastic Behavior of cross-linked and bundled actin networks*. Science, 2004. **304**(5675): p. 1301-1305.
63. Piechocka, I.K., et al., *Rheology of Heterotypic Collagen Networks*. Biomacromolecules, 2011. **12**(7): p. 2797-2805.
64. O'Brien, F.J., et al., *The effect of pore size on cell adhesion in collagen-GAG scaffolds*. Biomaterials, 2005. **26**(4): p. 433-441.
65. Hakkinen, K.M., et al., *Direct Comparisons of the Morphology, Migration, Cell Adhesions, and Actin Cytoskeleton of Fibroblasts in Four Different Three-Dimensional Extracellular Matrices*. Tiss Eng Pt A, 2011. **17**(5-6): p. 713-724.
66. Moreno-Arotzena, O., et al., *Characterization of Fibrin and Collagen Gels for Engineering Wound Healing Models*. Materials (Basel), 2015. **8**(4): p. 1636-1651.
67. Weigert, R., N. Porat-Shliom, and P. Amornphimoltham, *Imaging cell biology in live animals: Ready for prime time*. Journal of Cell Biology, 2013. **201**(7): p. 969-979.
68. Polacheck, W.J., et al., *Microfluidic platforms for mechanobiology*. Lab on a Chip, 2013. **13**(12): p. 2252-2267.
69. Chung, S., et al., *Microfluidic Platforms for Studies of Angiogenesis, Cell Migration, and Cell-Cell Interactions*. Ann Biomed Eng, 2010. **38**(3): p. 1164-1177.
70. Chung, B.G., et al., *Microfluidic fabrication of microengineered hydrogels and their application in tissue engineering*. Lab Chip, 2012. **12**(1): p. 45-59.
71. Song, J.W., et al., *Computer-controlled microcirculatory support system for endothelial cell culture and shearing*. Analytical Chemistry, 2005. **77**(13): p. 3993-3999.
72. van der Meer, A.D., et al., *Analyzing shear stress-induced alignment of actin filaments in endothelial cells with a microfluidic assay*. Biomicrofluidics, 2010. **4**(1).
73. Polacheck, W.J., J.L. Charest, and R.D. Kamm, *Interstitial flow influences direction of tumor cell migration through competing mechanisms*. Proceedings of the National Academy of Sciences of the United States of America, 2011. **108**(27): p. 11115-11120.
74. Kim, H.J., et al., *Human gut-on-a-chip inhabited by microbial flora that experiences intestinal peristalsis-like motions and flow*. Lab on a Chip, 2012. **12**(12): p. 2165-2174.
75. Sundararaghavan, H.G., et al., *Neurite Growth in 3D Collagen Gels With Gradients of Mechanical Properties*. Biotechnology and Bioengineering, 2009. **102**(2): p. 632-643.

76. Peyrin, J.M., et al., *Axon diodes for the reconstruction of oriented neuronal networks in microfluidic chambers*. Lab on a Chip, 2011. **11**(21): p. 3663-3673.
77. Legant, W.R., et al., *Microfabricated tissue gauges to measure and manipulate forces from 3D microtissues*. Proceedings of the National Academy of Sciences of the United States of America, 2009. **106**(25): p. 10097-10102.
78. Harris, A.K., P. Wild, and D. Stopak, *Silicone-Rubber Substrata - New Wrinkle in the Study of Cell Locomotion*. Science, 1980. **208**(4440): p. 177-179.
79. Beningo, K.A. and Y.L. Wang, *Flexible substrata for the detection of cellular traction forces*. Trends in Cell Biology, 2002. **12**(2): p. 79-84.
80. Kraning-Rush, C.M., et al., *Quantifying Traction Stresses in Adherent Cells*. Computational Methods in Cell Biology, 2012. **110**: p. 139-178.
81. Aratyn-Schaus, Y. and M.L. Gardel, *Transient Frictional Slip between Integrin and the ECM in Focal Adhesions under Myosin II Tension*. Current Biology, 2010. **20**(13): p. 1145-1153.
82. Ng, M.R., et al., *Substrate stiffness regulates cadherin-dependent collective migration through myosin-II contractility*. Journal of Cell Biology, 2012. **199**(3): p. 545-563.
83. Gardel, M.L., et al., *Traction stress in focal adhesions correlates biphasically with actin retrograde flow speed*. Journal of Cell Biology, 2008. **183**(6): p. 999-1005.
84. Polacheck, W.J. and C.S. Chen, *Measuring cell-generated forces: a guide to the available tools*. Nature Methods, 2016. **13**(5): p. 415-423.
85. Bell, E., B. Ivarsson, and C. Merrill, *Production of a Tissue-Like Structure by Contraction of Collagen Lattices by Human-Fibroblasts of Different Proliferative Potential In vitro*. Proceedings of the National Academy of Sciences of the United States of America, 1979. **76**(3): p. 1274-1278.
86. Ehrlich, H.P. and J.B.M. Rajaratnam, *Cell Locomotion Forces Versus Cell Contraction Forces for Collagen Lattice Contraction - an In vitro Model of Wound Contraction*. Tissue & Cell, 1990. **22**(4): p. 407-417.
87. Dallon, J.C. and H.P. Ehrlich, *A review of fibroblast-populated collagen lattices*. Wound Repair and Regeneration, 2008. **16**(4): p. 472-479.
88. Delvoye, P., et al., *Measurement of Mechanical Forces Generated by Skin Fibroblasts Embedded in a 3-Dimensional Collagen Gel*. Journal of Investigative Dermatology, 1991. **97**(5): p. 898-902.
89. Zimmermann, W.H., et al., *Three-dimensional engineered heart tissue from neonatal rat cardiac myocytes*. Biotechnology and Bioengineering, 2000. **68**(1): p. 106-114.
90. Dennis, R.G. and P.E. Kosnik, *Excitability and isometric contractile properties of mammalian skeletal muscle constructs engineered in vitro*. In Vitro Cellular & Developmental Biology-Animal, 2000. **36**(5): p. 327-335.
91. Hansen, A., et al., *Development of a Drug Screening Platform Based on Engineered Heart Tissue*. Circulation Research, 2010. **107**(1): p. 35-U70.
92. Zimmermann, W.H., et al., *Tissue engineering of a differentiated cardiac muscle construct*. Circulation Research, 2002. **90**(2): p. 223-230.
93. Vandeburgh, H., et al., *Drug-screening platform based on the contractility of tissue-engineered muscle*. Muscle & Nerve, 2008. **37**(4): p. 438-447.

94. Serrao, G.W., et al., *Myocyte-Depleted Engineered Cardiac Tissues Support Therapeutic Potential of Mesenchymal Stem Cells*. Tissue Engineering Part A, 2012. **18**(13-14): p. 1322-1333.
95. Boudou, T., et al., *A Microfabricated Platform to Measure and Manipulate the Mechanics of Engineered Cardiac Microtissues*. Tissue Engineering Part A, 2012. **18**(9-10): p. 910-919.
96. Hinson, J.T., et al., *Titin mutations in iPS cells define sarcomere insufficiency as a cause of dilated cardiomyopathy*. Science, 2015. **349**(6251): p. 982-986.
97. Khetan, S., et al., *Degradation-mediated cellular traction directs stem cell fate in covalently crosslinked three-dimensional hydrogels*. Nature Materials, 2013. **12**(5): p. 458-465.
98. Kim, I.L., et al., *Fibrous hyaluronic acid hydrogels that direct MSC chondrogenesis through mechanical and adhesive cues*. Biomaterials, 2013. **34**(22): p. 5571-5580.
99. Dembo, M., et al., *Imaging the traction stresses exerted by locomoting cells with the elastic substratum method*. Biophysical Journal, 1996. **70**(4): p. 2008-2022.
100. Dembo, M. and Y.L. Wang, *Stresses at the cell-to-substrate interface during locomotion of fibroblasts*. Biophysical Journal, 1999. **76**(4): p. 2307-2316.
101. Sabass, B., et al., *High resolution traction force microscopy based on experimental and computational advances*. Biophysical Journal, 2008. **94**(1): p. 207-220.
102. Landau, L. and E. Lifshitz, *Course of theoretical physics, volume 7 (3rd English edition): Theory of elasticity*. 1986, Butterworth-Heinemann, ISBN.
103. Butler, J.P., et al., *Traction fields, moments, and strain energy that cells exert on their surroundings*. American Journal of Physiology-Cell Physiology, 2002. **282**(3): p. C595-C605.
104. Trichet, L., et al., *Evidence of a large-scale mechanosensing mechanism for cellular adaptation to substrate stiffness*. Proceedings of the National Academy of Sciences of the United States of America, 2012. **109**(18): p. 6933-6938.
105. Ghassemi, S., et al., *Cells test substrate rigidity by local contractions on submicrometer pillars*. Proceedings of the National Academy of Sciences of the United States of America, 2012. **109**(14): p. 5328-5333.
106. Galbraith, C.G. and M.P. Sheetz, *A micromachined device provides a new bend on fibroblast traction forces*. Proceedings of the National Academy of Sciences of the United States of America, 1997. **94**(17): p. 9114-9118.
107. Rajagopalan, J., A. Tofangchi, and M.T.A. Saif, *Linear High-Resolution BioMEMS Force Sensors With Large Measurement Range*. Journal of Microelectromechanical Systems, 2010. **19**(6): p. 1380-1389.
108. Stabley, D.R., et al., *Visualizing mechanical tension across membrane receptors with a fluorescent sensor*. Nature Methods, 2012. **9**(1): p. 64-U172.
109. Liu, Y., et al., *Tension Sensing Nanoparticles for Mechano-Imaging at the Living/Nonliving Interface*. Journal of the American Chemical Society, 2013. **135**(14): p. 5320-5323.
110. Morimatsu, M., et al., *Molecular Tension Sensors Report Forces Generated by Single Integrin Molecules in Living Cells*. Nano Letters, 2013. **13**(9): p. 3985-3989.
111. Liu, Y., et al., *Nanoparticle Tension Probes Patterned at the Nanoscale: Impact of Integrin Clustering on Force Transmission*. Nano Letters, 2014. **14**(10): p. 5539-5546.

112. Cost, A.L., et al., *How to Measure Molecular Forces in Cells: A Guide to Evaluating Genetically-Encoded FRET-Based Tension Sensors*. Cellular and Molecular Bioengineering, 2015. **8**(1): p. 96-105.
113. Legant, W.R., et al., *Measurement of mechanical tractions exerted by cells in three-dimensional matrices*. Nature Methods, 2010. **7**(12): p. 969-U113.
114. Vitale, G., L. Preziosi, and D. Ambrosi, *A numerical method for the inverse problem of cell traction in 3D*. Inverse Problems, 2012. **28**(9).
115. Steinwachs, J., et al., *Three-dimensional force microscopy of cells in biopolymer networks*. Nature Methods, 2016. **13**(2): p. 171-+.
116. Dong, L. and A.A. Oberai, *Recovery of cellular traction in three-dimensional nonlinear hyperelastic matrices*. Computer Methods in Applied Mechanics and Engineering, 2017. **314**: p. 296-313.
117. Palacio, J., et al., *Numerical estimation of 3D mechanical forces exerted by cells on non-linear materials*. Journal of Biomechanics, 2013. **46**(1): p. 50-55.
118. Schwarz, U.S., et al., *Calculation of forces at focal adhesions from elastic substrate data: The effect of localized force and the need for regularization*. Biophysical Journal, 2002. **83**(3): p. 1380-1394.
119. Hall, M.S., et al., *Toward single cell traction microscopy within 3D collagen matrices*. Experimental Cell Research, 2013. **319**(16): p. 2396-2408.
120. Koch, T.M., et al., *3D Traction Forces in Cancer Cell Invasion*. Plos One, 2012. **7**(3).
121. Gjorevski, N. and C.M. Nelson, *Mapping of Mechanical Strains and Stresses around Quiescent Engineered Three-Dimensional Epithelial Tissues*. Biophysical Journal, 2012. **103**(1): p. 152-162.
122. Berrier, A.L. and K.M. Yamada, *Cell-matrix adhesion*. J Cell Physiol, 2007. **213**(3): p. 565-73.
123. Oakes, P.W. and M.L. Gardel, *Stressing the limits of focal adhesion mechanosensitivity*. Current Opinion in Cell Biology, 2014. **30**: p. 68-73.
124. Katoh, K., Y. Kano, and S. Ookawara, *Role of stress fibers and focal adhesions as a mediator for mechano-signal transduction in endothelial cells in situ*. Vasc Health Risk Manag, 2008. **4**(6): p. 1273-82.
125. Case, L.B. and C.M. Waterman, *Integration of actin dynamics and cell adhesion by a three-dimensional, mechanosensitive molecular clutch*. Nature Cell Biology, 2015. **17**(8): p. 955-963.
126. Fouchard, J., et al., *Three-dimensional cell body shape dictates the onset of traction force generation and growth of focal adhesions*. Proc Natl Acad Sci U S A, 2014. **111**(36): p. 13075-80.
127. Vicente-Manzanares, M. and A.R. Horwitz, *Adhesion dynamics at a glance*. Journal of Cell Science, 2011. **124**(23): p. 3923-3927.
128. Fraley, S.I., et al., *A distinctive role for focal adhesion proteins in three-dimensional cell motility*. Nat Cell Biol, 2010. **12**(6): p. 598-604.
129. Gilmore, A.P. and L.H. Romer, *Inhibition of focal adhesion kinase (FAK) signaling in focal adhesions decreases cell motility and proliferation*. Molecular Biology of the Cell, 1996. **7**(8): p. 1209-24.
130. Kanchanawong, P., et al., *Nanoscale architecture of integrin-based cell adhesions*. Nature, 2010. **468**(7323): p. 580-U262.

131. Vogel, V. and M.P. Sheetz, *Cell fate regulation by coupling mechanical cycles to biochemical signaling pathways*. Current Opinion in Cell Biology, 2009. **21**(1): p. 38-46.
132. Moore, S.W., P. Roca-Cusachs, and M.P. Sheetz, *Stretchy proteins on stretchy substrates: the important elements of integrin-mediated rigidity sensing*. Dev Cell, 2010. **19**(2): p. 194-206.
133. Harjanto, D. and M.H. Zaman, *Matrix mechanics and receptor-ligand interactions in cell adhesion*. Org Biomol Chem, 2010. **8**(2): p. 299-304.
134. Cavalcanti-Adam, E.A., et al., *Cell spreading and focal adhesion dynamics are regulated by spacing of integrin ligands*. Biophys J, 2007. **92**(8): p. 2964-74.
135. Geiger, B., et al., *Transmembrane extracellular matrix-cytoskeleton crosstalk*. Nature Reviews Molecular Cell Biology, 2001. **2**(11): p. 793-805.
136. Lele, T.P., et al., *Mechanical forces alter zyxin unbinding kinetics within focal adhesions of living cells*. J Cell Physiol, 2006. **207**(1): p. 187-94.
137. Nicolas, A., B. Geiger, and S.A. Safran, *Cell mechanosensitivity controls the anisotropy of focal adhesions*. Proc Natl Acad Sci U S A, 2004. **101**(34): p. 12520-5.
138. Dokukina, I.V. and M.E. Gracheva, *A model of fibroblast motility on substrates with different rigidities*. Biophys J, 2010. **98**(12): p. 2794-803.
139. Lemmon, C.A. and L.H. Romer, *A predictive model of cell traction forces based on cell geometry*. Biophys J, 2010. **99**(9): p. L78-80.
140. Zhong, Y. and B. Ji, *Impact of cell shape on cell migration behavior on elastic substrate*. Biofabrication, 2013. **5**(1): p. 015011.
141. Tee, S.Y., et al., *Cell shape and substrate rigidity both regulate cell stiffness*. Biophys J, 2011. **100**(5): p. L25-7.
142. Smilenov, L.B., et al., *Focal adhesion motility revealed in stationary fibroblasts*. Science, 1999. **286**(5442): p. 1172-4.
143. Ponti, A., et al., *Two distinct actin networks drive the protrusion of migrating cells*. Science, 2004. **305**(5691): p. 1782-6.
144. Pollard, T.D. and G.G. Borisy, *Cellular motility driven by assembly and disassembly of actin filaments*. Cell, 2003. **112**(4): p. 453-465.
145. Alexandrova, A.Y., et al., *Comparative dynamics of retrograde actin flow and focal adhesions: formation of nascent adhesions triggers transition from fast to slow flow*. PLoS One, 2008. **3**(9): p. e3234.
146. Choi, C.K., et al., *Actin and alpha-actinin orchestrate the assembly and maturation of nascent adhesions in a myosin II motor-independent manner*. Nat Cell Biol, 2008. **10**(9): p. 1039-50.
147. Geiger, B. and K.M. Yamada, *Molecular architecture and function of matrix adhesions*. Cold Spring Harb Perspect Biol, 2011. **3**(5).
148. Schwarz, U.S. and S.A. Safran, *Physics of adherent cells*. Reviews of Modern Physics, 2013. **85**(3): p. 1327-1381.
149. Ladoux, B. and A. Nicolas, *Physically based principles of cell adhesion mechanosensitivity in tissues*. Reports on Progress in Physics, 2012. **75**(11).
150. Bell, G.I., *Theoretical-Models for the Specific Adhesion of Cells to Cells or to Surfaces*. Advances in Applied Probability, 1980. **12**(3): p. 566-567.

151. Evans, E., *Energy landscapes of biomolecular adhesion and receptor anchoring at interfaces explored with dynamic force spectroscopy*. Faraday Discuss, 1998(111): p. 1-16.
152. Deshpande, V.S., R.M. McMeeking, and A.G. Evans, *A bio-chemo-mechanical model for cell contractility*. Proc Natl Acad Sci U S A, 2006. **103**(38): p. 14015-20.
153. Olberding, J.E., et al., *The non-equilibrium thermodynamics and kinetics of focal adhesion dynamics*. PLoS One, 2010. **5**(8): p. e12043.
154. Wang, J.Z. and H.J. Gao, *Clustering instability in adhesive contact between elastic solids via diffusive molecular bonds*. Journal of the Mechanics and Physics of Solids, 2008. **56**(1): p. 251-266.
155. Freund, L.B. and Y. Lin, *The role of binder mobility in spontaneous adhesive contact and implications for cell adhesion*. Journal of the Mechanics and Physics of Solids, 2004. **52**(11): p. 2455-2472.
156. Bruinsma, R., *Theory of force regulation by nascent adhesion sites*. Biophys J, 2005. **89**(1): p. 87-94.
157. Shemesh, T., et al., *Focal adhesions as mechanosensors: A physical mechanism*. Proceedings of the National Academy of Sciences of the United States of America, 2005. **102**(35): p. 12383-12388.
158. Chan, C.E. and D.J. Odde, *Traction Dynamics of Filopodia on Compliant Substrates*. Science, 2008. **322**(5908): p. 1687-1691.
159. Elosegui-Artola, A., et al., *Rigidity sensing and adaptation through regulation of integrin types*. Nat Mater, 2014. **13**(6): p. 631-7.
160. Paszek, M.J., et al., *Integrin clustering is driven by mechanical resistance from the glycocalyx and the substrate*. PLoS Comput Biol, 2009. **5**(12): p. e1000604.
161. Ronan, W., et al., *Cellular contractility and substrate elasticity: a numerical investigation of the actin cytoskeleton and cell adhesion*. Biomech Model Mechanobiol, 2014. **13**(2): p. 417-35.
162. Musto, M. and G. Alfano, *A novel rate-dependent cohesive-zone model combining damage and visco-elasticity*. Computers & Structures, 2013. **118**: p. 126-133.
163. Camacho, G.T. and M. Ortiz, *Computational modelling of impact damage in brittle materials*. International Journal of Solids and Structures, 1996. **33**(20-22): p. 2899-2938.
164. Moreo, P., et al., *Modelling the mechanical behaviour of living bony interfaces*. Computer Methods in Applied Mechanics and Engineering, 2007. **196**(35-36): p. 3300-3314.
165. Garcia-Aznar, J.M., M.A. Perez, and P. Moreo, *Modelling of Interfaces in Biomechanics and Mechanobiology*. Cmes-Computer Modeling in Engineering & Sciences, 2009. **48**(3): p. 271-302.
166. Simo, J.C. and T.J.R. Hughes, *Computational inelasticity*. Interdisciplinary applied mathematics. 1998, New York: Springer. xiv, 392 p.
167. Legant, W.R., et al., *Multidimensional traction force microscopy reveals out-of-plane rotational moments about focal adhesions*. Proc Natl Acad Sci U S A, 2013. **110**(3): p. 881-6.
168. Tziampazis, E., J. Kohn, and P.V. Moghe, *PEG-variant biomaterials as selectively adhesive protein templates: model surfaces for controlled cell adhesion and migration*. Biomaterials, 2000. **21**(5): p. 511-20.

169. Mofrad, M.R.K. and R.D. Kamm, *Cytoskeletal mechanics : models and measurements*. 2006, Cambridge ; New York: Cambridge University Press. x, 244 p.
170. Franck, C., et al., *Three-dimensional traction force microscopy: a new tool for quantifying cell-matrix interactions*. PLoS One, 2011. **6**(3): p. e17833.
171. Crow, A., et al., *Contractile equilibration of single cells to step changes in extracellular stiffness*. Biophys J, 2012. **102**(3): p. 443-51.
172. Evans, E.A. and D.A. Calderwood, *Forces and bond dynamics in cell adhesion*. Science, 2007. **316**(5828): p. 1148-53.
173. Mitrossilis, D., et al., *Real-time single-cell response to stiffness*. Proceedings of the National Academy of Sciences of the United States of America, 2010. **107**(38): p. 16518-16523.
174. Borau, C., R.D. Kamm, and J.M. Garcia-Aznar, *A time-dependent phenomenological model for cell mechano-sensing*. Biomech Model Mechanobiol, 2013.
175. Aroush, D.R.B., et al., *Temporal evolution of cell focal adhesions: experimental observations and shear stress profiles*. Soft Matter, 2008. **4**(12): p. 2410-2417.
176. Solon, J., et al., *Fibroblast adaptation and stiffness matching to soft elastic substrates*. Biophysical Journal, 2007. **93**(12): p. 4453-4461.
177. Slomka, N. and A. Gefen, *Confocal microscopy-based three-dimensional cell-specific modeling for large deformation analyses in cellular mechanics*. J Biomech, 2010. **43**(9): p. 1806-16.
178. C ndor, M., et al., *A web-based application for automated quantification of chemical gradients induced in microfluidic devices*. Computers in Biology and Medicine, 2018.
179. Moreno-Arotzena, O., et al., *Inducing chemotactic and haptotactic cues in microfluidic devices for three-dimensional in vitro assays*. Biomicrofluidics, 2014. **8**(6).
180. Li, L., et al., *Collective cell migration: Implications for wound healing and cancer invasion*. Burns & trauma, 2013. **1**(1): p. 21.
181. Martin, P., *Wound healing - Aiming for perfect skin regeneration*. Science, 1997. **276**(5309): p. 75-81.
182. Friedl, P. and D. Gilmour, *Collective cell migration in morphogenesis, regeneration and cancer*. Nature Reviews Molecular Cell Biology, 2009. **10**(7): p. 445-457.
183. Wang, W.G., et al., *Tumor cells caught in the act of invading: their strategy for enhanced cell motility*. Trends in Cell Biology, 2005. **15**(3): p. 138-145.
184. Garrett, Q., et al., *Involvement of CTGF in TGF- 1–Stimulation of Myofibroblast Differentiation and Collagen Matrix Contraction in the Presence of Mechanical Stress*. Investigative Ophthalmology & Visual Science, 2004. **45**(4): p. 1109-1116.
185. Long, C.J., et al., *Fibroblast growth factor-2 promotes keratan sulfate proteoglycan expression by keratocytes in vitro*. Journal of Biological Chemistry, 2000. **275**(18): p. 13918-13923.
186. Jester, J.V. and J. Ho-Chang, *Modulation of cultured corneal keratocyte phenotype by growth factors/cytokines control in vitro contractility and extracellular matrix contraction*. Exp Eye Res, 2003. **77**(5): p. 581-92.

187. Roussos, E.T., J.S. Condeelis, and A. Patsialou, *Chemotaxis in cancer*. Nat Rev Cancer, 2011. **11**(8): p. 573-87.
188. Petrie, R.J., A.D. Doyle, and K.M. Yamada, *Random versus directionally persistent cell migration*. Nat Rev Mol Cell Biol, 2009. **10**(8): p. 538-49.
189. Aznavoorian, S., et al., *Signal transduction for chemotaxis and haptotaxis by matrix molecules in tumor cells*. J Cell Biol, 1990. **110**(4): p. 1427-38.
190. Kramer, N., et al., *In vitro cell migration and invasion assays*. Mutation Research-Reviews in Mutation Research, 2013. **752**(1): p. 10-24.
191. Zervantonakis, I.K., et al., *Three-dimensional microfluidic model for tumor cell intravasation and endothelial barrier function*. Proceedings of the National Academy of Sciences, 2012. **109**(34): p. 13515-13520.
192. Lee, J.H., et al., *Microfluidic 3D bone tissue model for high-throughput evaluation of wound-healing and infection-preventing biomaterials*. Biomaterials, 2012. **33**(4): p. 999-1006.
193. Wu, J.D., X. Wu, and F. Lin, *Recent developments in microfluidics-based chemotaxis studies*. Lab on a Chip, 2013. **13**(13): p. 2484-2499.
194. Kothapalli, C.R., et al., *A high-throughput microfluidic assay to study neurite response to growth factor gradients*. Lab Chip, 2011. **11**(3): p. 497-507.
195. Taipale, J. and J. Keski-Oja, *Growth factors in the extracellular matrix*. Faseb Journal, 1997. **11**(1): p. 51-9.
196. Brizzi, M.F., G. Tarone, and P. Defilippi, *Extracellular matrix, integrins, and growth factors as tailors of the stem cell niche*. Current Opinion in Cell Biology, 2012. **24**(5): p. 645-51.
197. Martino, M.M., et al., *Growth Factors Engineered for Super-Affinity to the Extracellular Matrix Enhance Tissue Healing*. Science, 2014. **343**(6173): p. 885-888.
198. Peppas, N.A., et al., *Hydrogels in biology and medicine: from molecular principles to bionanotechnology*. Advanced Materials, 2006. **18**(11): p. 1345-1360.
199. Geckil, H., et al., *Engineering hydrogels as extracellular matrix mimics*. Nanomedicine, 2010. **5**(3): p. 469-484.
200. Frantz, C., K.M. Stewart, and V.M. Weaver, *The extracellular matrix at a glance*. J Cell Sci, 2010. **123**(Pt 24): p. 4195-200.
201. Diegelmann, R.F. and M.C. Evans, *Wound healing: An overview of acute, fibrotic and delayed healing*. Frontiers in Bioscience, 2004. **9**: p. 283-289.
202. Weisel, J.W., *The mechanical properties of fibrin for basic scientists and clinicians*. Biophysical Chemistry, 2004. **112**(2-3): p. 267-276.
203. Ern, A. and J.-L. Guermond, *Theory and practice of finite elements*. 2010, New York: Springer.
204. Shin, Y., et al., *Microfluidic assay for simultaneous culture of multiple cell types on surfaces or within hydrogels*. Nature protocols, 2012. **7**(7): p. 1247-1259.
205. Moreno-Arotzena, O., et al., *Fibroblast Migration in 3D is Controlled by Haptotaxis in a Non-muscle Myosin II-Dependent Manner*. Ann Biomed Eng, 2015. **43**(12): p. 3025-39.
206. Martino, M.M., et al., *Heparin-binding domain of fibrin (ogen) binds growth factors and promotes tissue repair when incorporated within a synthetic matrix*. Proceedings of the National Academy of Sciences, 2013. **110**(12): p. 4563-4568.

207. Kihara, T., J. Ito, and J. Miyake, *Measurement of biomolecular diffusion in extracellular matrix condensed by fibroblasts using fluorescence correlation spectroscopy*. PLoS One, 2013. **8**(11): p. e82382.
208. Einstein, A., *Über die von der molekularkinetischen Theorie der Wärme geforderte Bewegung von in ruhenden Flüssigkeiten suspendierten Teilchen*. Annalen der physik, 1905. **322**(8): p. 549-560.
209. Ogston, A., B. Preston, and J. Wells, *On the transport of compact particles through solutions of chain-polymers*. Proceedings of the Royal Society of London. A. Mathematical and Physical Sciences, 1973. **333**(1594): p. 297-316.
210. Kim, W.-S. and J.M. Tarbell, *Macromolecular transport through the deformable porous media of an artery wall*. Journal of biomechanical engineering, 1994. **116**(2): p. 156-163.
211. Del Amo, C., et al., *Quantification of angiogenic sprouting under different growth factors in a microfluidic platform*. Journal of Biomechanics, 2016. **49**(8): p. 1340-1346.
212. Del Amo, C., et al., *Quantifying 3D chemotaxis in microfluidic-based chips with step gradients of collagen hydrogel concentrations*. Integrative Biology, 2017. **9**(4): p. 339-349.
213. Li, J., et al., *Microfluidic device for studying cell migration in single or co-existing chemical gradients and electric fields*. Biomicrofluidics, 2012. **6**(2): p. 24121-2412113.
214. Geuzaine, C. and J.F. Remacle, *Gmsh: A 3-D finite element mesh generator with built-in pre- and post-processing facilities*. International Journal for Numerical Methods in Engineering, 2009. **79**(11): p. 1309-1331.
215. Rüberg, T., F. Cirak, and J.M.G. Aznar, *An unstructured immersed finite element method for nonlinear solid mechanics*. Advanced Modeling and Simulation in Engineering Sciences, 2016. **3**(1): p. 22.
216. Ern, A. and J.-L. Guermond, *Theory and practice of finite elements*. Vol. 159. 2013: Springer Science & Business Media.
217. Thain, D., T. Tannenbaum, and M. Livny, *Distributed computing in practice: the Condor experience*. Concurrency and Computation-Practice & Experience, 2005. **17**(2-4): p. 323-356.
218. Wang, S.J., et al., *Differential effects of EGF gradient profiles on MDA-MB-231 breast cancer cell chemotaxis*. Experimental Cell Research, 2004. **300**(1): p. 180-189.
219. Hughes-Alford, S.K. and D.A. Lauffenburger, *Quantitative analysis of gradient sensing: towards building predictive models of chemotaxis in cancer*. Current Opinion in Cell Biology, 2012. **24**(2): p. 284-291.
220. Sudo, R., et al., *Transport-mediated angiogenesis in 3D epithelial coculture*. Faseb Journal, 2009. **23**(7): p. 2155-2164.
221. Jeong, G.S., et al., *Sprouting Angiogenesis under a Chemical Gradient Regulated by Interactions with an Endothelial Monolayer in a Microfluidic Platform*. Analytical Chemistry, 2011. **83**(22): p. 8454-8459.
222. Borau, C., R.D. Kamm, and J.M. Garcia-Aznar, *Mechano-sensing and cell migration: a 3D model approach*. Physical Biology, 2011. **8**(6).
223. Córdor, M., et al., *Traction Force Microscopy in 3-Dimensional Extracellular Matrix Networks*. Current protocols in cell biology, 2017: p. 10.22. 1-10.22. 20.

224. Sniadecki, N.J., et al., *Magnetic microposts as an approach to apply forces to living cells*. Proceedings of the National Academy of Sciences of the United States of America, 2007. **104**(37): p. 14553-14558.
225. Toyjanova, J., et al., *High Resolution, Large Deformation 3D Traction Force Microscopy*. Plos One, 2014. **9**(4).
226. Toyjanova, J., et al., *3D Viscoelastic traction force microscopy*. Soft Matter, 2014. **10**(40): p. 8095-8106.
227. Munoz, J.J., *Non-Regularised Inverse Finite Element Analysis for 3d Traction Force Microscopy*. International Journal of Numerical Analysis and Modeling, 2016. **13**(5): p. 763-781.
228. Barreto, S., et al., *A multi-structural single cell model of force-induced interactions of cytoskeletal components*. Biomaterials, 2013. **34**(26): p. 6119-6126.
229. Fraley, S.I., et al., *Three-dimensional matrix fiber alignment modulates cell migration and MT1-MMP utility by spatially and temporally directing protrusions*. Scientific Reports, 2015. **5**.
230. Ehrbar, M., et al., *Elucidating the Role of Matrix Stiffness in 3D Cell Migration and Remodeling*. Biophysical Journal, 2011. **100**(2): p. 284-293.
231. Buxboim, A., I.L. Ivanovska, and D.E. Discher, *Matrix elasticity, cytoskeletal forces and physics of the nucleus: how deeply do cells 'feel' outside and in?* Journal of Cell Science, 2010. **123**(3): p. 297-308.
232. Lautscham, L.A., et al., *Migration in Confined 3D Environments Is Determined by a Combination of Adhesiveness, Nuclear Volume, Contractility, and Cell Stiffness*. Biophysical Journal, 2015. **109**(5): p. 900-913.
233. Fabry, B., et al., *Scaling the microrheology of living cells*. Physical Review Letters, 2001. **87**(14).
234. Metzner, C., et al., *Fluctuations of cytoskeleton-bound microbeads-the effect of bead-receptor binding dynamics*. Journal of Physics-Condensed Matter, 2010. **22**(19).
235. Mierke, C.T., et al., *Integrin alpha 5 beta 1 facilitates cancer cell invasion through enhanced contractile forces*. Journal of Cell Science, 2011. **124**(3): p. 369-383.
236. Thievensen, I., et al., *Vinculin is required for cell polarization, migration, and extracellular matrix remodeling in 3D collagen*. Faseb Journal, 2015. **29**(11): p. 4555-4567.
237. Lang, N.R., et al., *Estimating the 3D Pore Size Distribution of Biopolymer Networks from Directionally Biased Data*. Biophysical Journal, 2013. **105**(9): p. 1967-1975.
238. Cross, S.E., et al., *Nanomechanical analysis of cells from cancer patients*. Nature Nanotechnology, 2007. **2**(12): p. 780-783.